

Correlated Percolation in the Fracture Dynamics on a Network of Ionomer Bundles

by

Yule Wang

M.Sc., Simon Fraser University, 2015
B.Sc., Harbin University of Science and Technology, 2012

Thesis Submitted in Partial Fulfillment of the
Requirements for the Degree of
Doctor of Philosophy

in the
Department of Physics
Faculty of Science

**© Yule Wang 2020
SIMON FRASER UNIVERSITY
Fall 2020**

Copyright in this work rests with the author. Please ensure that any reproduction
or re-use is done in accordance with the relevant national copyright legislation.

Declaration of Committee

Name: **Yule Wang**

Degree: **Doctor of Philosophy**

Title: **Correlated Percolation in the Fracture Dynamics
on a Network of Ionomer Bundles**

Committee:

Chair: Keren Kavanagh
Professor, Physics

Malcolm Kennett
Supervisor
Associate Professor, Physics

Michael Eikerling
Committee Member
Adjunct Faculty, Chemistry

Barbara Frisken
Committee Member
Professor, Physics

Steven Holdcroft
Examiner
Professor, Chemistry

Ferenc Kun
External Examiner
Professor
Department of Theoretical Physics
University of Debrecen

Abstract

Motivated by predicting the lifetime of polymer electrolyte membranes (PEMs), we map the fracture dynamics of a network of ionomer bundles onto a correlated percolation model. A kinetic Monte Carlo method is employed to study these dynamics. The swelling pressure upon water uptake causes the breakage events of ionomer bundles, and the strength of the bundle-to-bundle correlations is characterized by the stress field and the stress redistribution scheme. Local load sharing (LLS) and equal load sharing (ELS) are the two most frequently studied stress transfer schemes. We adopt a stress transfer scheme that follows a power-law-type spatial decay in this thesis as an intermediate scheme between LLS and ELS. By tuning the magnitude of the stress field and the effective range of stress transfer, two fracture regimes, i.e., the random breakage (percolation-type) regime and the localization (correlated crack growth) regime, can be observed. A central property considered in this thesis is the frequency distribution of percolation thresholds. Based on this distribution, we introduce an order parameter to assess the crossover between these two fracture regimes. Moreover, the average percolation threshold is found to exhibit a peculiar variation, which has not been reported in previous correlated percolation studies.

Keywords: fracture dynamics; nucleation; percolation; correlated percolation; PEM

Dedication

To my mom

To physics

Acknowledgements

I would like to express my sincere gratitude to my supervisors, Dr. Michael Eikerling and Dr. Malcolm Kennett, for their patient guidance and support during my PhD study. I feel blessed to be working with a group of colleagues from Dr. Eikerling's group and from the Department of Physics at Simon Fraser University. I would also like to thank my colleagues Fafu Niu and Nicholas Lee-Hone for fruitful research discussions. I am also very grateful to Mpumelelo Maste, Justine Munich Michael Desrochers, Narinder Singh Khattri, Qingxin Zhang and Pingyi Zhang for their invaluable suggestions during thesis writing. I also thank my dear friends Jun Huang and Lishen Zhang for their support when I was going through a difficult time. Finally, I acknowledge Simon Fraser University, NSERC and Dr. Kjeang for financial support.

Table of Contents

Declaration of Committee	ii
Abstract	iii
Dedication	iv
Acknowledgements	v
Table of Contents	vi
List of Tables	ix
List of Figures	x
Nomenclature	xiii
1 Introduction	1
1.1 Statistical Mechanics of Fracture Networks	1
1.2 Fracture formation on Polymer Electrolyte Membranes	2
1.3 Challenges	4
1.4 Dissertation Organization	6
2 Theoretical Background and Literature Reviews	8
2.1 Fracture Disordered Systems	8
2.1.1 Crack Nucleation and Growth	9
2.1.2 Load-transfer Laws	11
2.1.3 Weibull and Gumbel Strength Distributions (Power-law and Exponential Decay Rates)	12
2.2 Percolation Theory	14
2.2.1 Uncorrelated Percolation	14
2.2.2 Correlated Percolation	18
3 Model	21
3.1 Overview	21

3.2	Model	24
3.2.1	Bundle of Ionomer Fibers	24
3.2.2	Bundle Network Model	25
3.2.3	Remarks	27
4	Computational Approach and Methods	29
4.1	Kinetic Monte Carlo Algorithms	29
4.1.1	Markov Chain Monte Carlo	29
4.1.2	Rejection-free Kinetic Monte Carlo	30
4.1.3	Adopting the Rejection-free MC Method for the PEM Fracture Model	31
4.2	Percolation Algorithm	32
4.3	Algorithm	34
4.4	Remarks on the Algorithm	37
5	Results: Fracture Regimes and Percolation Behaviour at a Fixed Lattice Size	39
5.1	Overview	39
5.2	Percolation Regimes and Order Parameter	40
5.2.1	Distribution of Percolation Thresholds for Different Regimes	40
5.2.2	Order Parameter	42
5.2.3	Phase Diagram	43
5.3	Percolation Behaviour	45
5.3.1	Expectation Values of the Two Peaks	45
5.3.2	Average Percolation Threshold	46
5.4	Cluster Structure Analysis	49
5.4.1	Dynamics of the Largest Crack	49
5.4.2	Cluster Structures (Static)	53
5.5	Time-to-Fracture	55
5.6	Summary	58
6	Results: Finite Size Effects	59
6.1	Overview	59
6.2	Phase Diagram	60
6.3	Transition of Fracture Regimes in the Crossover Region	61
6.3.1	Order Parameter ξ	62
6.3.2	Largest Crack Dynamics	63
6.4	Variation of Percolation Thresholds	64
6.5	Time-to-Fracture	65
6.6	Preliminary Studies	66
6.6.1	Fracture Regimes for Small σ^0 or γ	66

6.7	Summary	68
7	Conclusions and Outlook	69
7.1	Conclusions	69
7.2	Outlook	71
	Bibliography	72

List of Tables

Table 2.1 Site or bond percolation thresholds for the square lattice (2D), triangular lattice (2D), honeycomb lattice (2D) and simple cubic lattice (3D).	15
Table 3.1 Effective coefficients α_k/α_1 and η_k/η_1 for $k \leq 10$	25
Table 5.1 Lifetime for $k = 1, 3, 10$ at $T = 298$ and 353K in the range of $\sigma^0 = 3 - 30$ MPa. The two limits for the range of t_{PEM} values given in parentheses correspond to γ varying from 0 to 100 respectively.	58

List of Figures

Figure 1.1	Schematic illustration of a PEM fuel cell.	3
Figure 1.2	X-ray computed tomography images of the fatigue propagation tracking of an identical area of a Nafion-type membrane plane from beginning of life (BOL) condition to thousands of wet/dry cycles.	5
Figure 2.1	Illustrations of (a) nucleation and (b) growth	10
Figure 2.2	Free energy representation of spinodal nucleation.	10
Figure 2.3	A phase diagram of random breakage (percolation-like) regime to nucleation (localization) regime	14
Figure 2.4	Wrapping probability R as a function of the concentration	17
Figure 2.5	Wrapping probability R (solid lines) for finite-sized lattices and infinite-sized lattices.	18
Figure 3.1	Ionomer fibers with hydrophobic backbone (red) and grafted sidechains (red) terminated with sulfonic acid head groups (yellow) that dissociate in water.	22
Figure 3.2	In the model by Ioselevich <i>et al.</i> , the fiber-bundle-network for PEM is constructed of an ordered structured network of cages, made of cylindrical bundles.	23
Figure 3.3	Illustrations of the comparison of the two models of bundle of fibers: (a) FBM and (b) ionomer fibers in a bundle in a PEM	24
Figure 3.4	An illustration of how the stress of failing bundles is transferred in the bundle-network	27
Figure 4.1	An illustration of two tree-structures which represents the clusters A and B and the merging process of the two clusters.	33
Figure 4.2	Frequency distributions of p_c^L in the uncorrelated case	34
Figure 4.3	A flowchart of Monte Carlo simulations of a particular configuration of L , $\eta_k \sigma^0$ and γ	35
Figure 4.4	An illustration of a square lattice of an $L \times L$ square lattice.	37

Figure 5.1	Normalized frequency distributions of percolation thresholds for a square lattice with $L = 100$, for random breakage regime and localization regime	41
Figure 5.2	Normalized frequency distribution of percolation thresholds for the crossover region	42
Figure 5.3	Plots of the order parameter $\xi = A_2/(A_1 + A_2)$ over (a) σ^0 and (b) γ	43
Figure 5.4	Phase diagram, illustrated as a color map, in the plane spanned by γ and $\eta_k\sigma^0$	44
Figure 5.5	Normalized frequency distribution of percolation thresholds that exhibits three discernible peaks for the case with $\gamma = 1.2$, $\eta_k\sigma^0 = 5.0$	45
Figure 5.6	Plots of (a) μ_1 and (b) μ_2 as a function of γ with $\eta_k\sigma^0$ as parameter.	47
Figure 5.7	Plots of average percolation thresholds p_{av}^L over (a) γ with $\eta_k\sigma^0$ as parameter, and (b) $\eta\sigma^0$ with γ as parameter.	48
Figure 5.8	Normalized growth of the largest crack size S_L/N with the fraction of failed bonds N_b/N in the lattice. Three regimes are shown: uncorrelated percolation, crossover, and localization	50
Figure 5.9	Normalized growth of the largest crack size S_L/N with the fraction of failed bonds N_b/N in the lattice for different stresses with γ as parameter.	51
Figure 5.10	Normalized growth of the largest crack size S_L/N with the fraction of failed bonds in the lattice for different γ with $\eta_k\sigma^0$ as parameter.	52
Figure 5.11	Cluster structures (a) $m_{0,c}$, (b) $m_{1,c}$, (c) $S_{av,c}$ and (d) $S_{L,c}$ at a percolation threshold as a function of γ for different stresses	54
Figure 5.12	Frequency distributions of the time to fracture t_{PEM} (normalized to α_k) for systems in the regime of random breakage, crossover region and localization regime.	56
Figure 5.13	Time-to-fracture t_{PEM} (normalized to α_k) (a) on a log-scale as a function of $\eta_k\sigma^0$ with γ as parameter and (b) as a function of γ with $\eta_k\sigma^0$ as parameter.	56
Figure 5.14	A color map of t_{PEM} in the γ and $\eta_k\sigma^0$ plane.	57
Figure 6.1	The minimum values of m_0 are shown by triangular dots linked by a dashed line. The color map represents the phase diagram (Fig. 5.4) in the plane spanned by γ and $\eta_k\sigma^0$ and was generated with the order parameter ξ . Regimes of random breakage and localization are separated by a narrow crossover region. The minimum values of m_0 clearly fall into the crossover region. Thus, minimum values of m_0 can be adopted to separate the two regimes for larger sizes L	61

Figure 6.2	Phase diagrams in the plane spanned by γ and $\eta_k\sigma^0$ for different sizes $L = 100, 250$ and 400	62
Figure 6.3	Frequency distributions of the percolation thresholds for (a) $L = 250$, $\eta_k\sigma^0 = 0.51$, $\gamma = 5.5$ performed by 325 MC runs and (b) $L = 400$, $\eta_k\sigma^0 = 0.61$, $\gamma = 4$ performed by 80 MC runs.	62
Figure 6.4	ξ obtained with $\eta_k\sigma^0 = 0.41$ and $\eta_k\sigma^0 = 0.36$ for $\gamma = 100$ (LLS) as a function of sizes L in the crossover region.	63
Figure 6.5	Largest crack growth S_L/N as a function of damage fraction N_b/N for $\eta_k\sigma_0 = 0.41$ and $\gamma = 100$ (solid lines) for several sizes L	64
Figure 6.6	Plots of the average percolation thresholds p_{av}^L over γ for (a) $\eta_k\sigma^0 = 0.51$, (b) $\eta_k\sigma^0 = 1.0$ and (c) $\eta_k\sigma^0 = 5.0$, and p_{av}^L over $\eta_k\sigma^0$ for (d) $\gamma = 100$ for different L	65
Figure 6.7	Time-to-fracture t_{PEM} (normalized to α_k) for (b) the uncorrelated system, (e) the crossover region, and (h) the localization regime as a function of L	67
Figure 6.8	Largest crack growth S_L/N for $\eta_k\sigma^0 = 0.2$ and $\gamma = 100$ (solid lines) compared with the growth dynamics of uncorrelated percolation (dashed lines).	68

Nomenclature

Parameter/Variable	Description	Units
k_B	Boltzmann constant	J/K
T	temperature	K
β	$1/(k_B T)$	1/J
E_a	activation energy	J
p	concentration	-
p_c	percolation threshold (infinite lattice)	-
R	wrapping probability	-
L	linear size of the finite lattice	-
N	number of edges (finite lattice of L)	-
p_c^L	percolation threshold (finite lattice of L)	-
p_{av}^L	average percolation threshold (finite lattice of L)	-
p_c^{uncor}	average uncorrelated percolation threshold	-
s	cluster size	-
n_s	size cluster distribution	-
m_k	k^{th} moment of cluster size distribution	-
ξ	connectivity length	-
$\alpha, \beta, \gamma, \delta, \nu$	percolation scaling critical exponents	-
k	number of ionomer fibers in a bundle	-
ν	ionomer fiber activation volume	m^3
σ_f	ionomer fiber stress	Pa
σ	bundle stress	Pa
σ^0	uniform initial stress	Pa
λ	correlation length (correlated percolation systems)	-
ξ	order parameter (fracture systems)	-
κ_f	ionomer fiber breakage rate	1/s
κ_b	bundle breakage rate	1/s
τ_0	ionomer fiber vibration period	s
η_k	scaling parameter of k size bundle	1/Pa
α_k	scaling parameter of k size bundle	1/s
r_{ij}	distance between bundles i and j	-
γ	effective range of stress transfer parameter	-
μ_1, μ_2	expected values of Gaussian distributions	-
n	number of Monte Carlo runs	-
t_{PEM}	time to fracture	s

Chapter 1

Introduction

This thesis presents Monte Carlo simulations of the fracture dynamics in polymer electrolyte membranes (PEMs). The fracture processes of a network of ionomer bundles is mapped onto a bond percolation model. The introduction provides the context and motivation of the fracture dynamics of PEMs from both a theoretical and a practical point of view, together with an outline of the structure of the thesis.

1.1 Statistical Mechanics of Fracture Networks

The fracture mechanics of solids is a long-lived topic that has garnered interest in both engineering and theoretical physics communities. Historical evidence of this field can be traced back to the age of Leonardo da Vinci (1452–1519) and Galileo Galilei (1564–1642), when the rupture and strength of metal wires and beams were systematically studied [1, 2, 3]. A century ago, scientists started to master this field with modern physics concepts and approaches. In 1920, a milestone was marked by Griffith [4], when he related the surface energy (per unit area) that must be overcome to the onset of crack propagation. Later, Weibull [5] formulated the fracture strength of a solid from a statistical point of view.

Since the mid-1980s, fractured media have attracted attention from the statistical physics community [6, 7, 8, 9]. Mishnaevsky in Ref. [10] proposed that fracture is a random and complex process, based on experimental observations [11, 12, 13, 14]. Moreover, structural materials can be treated as a network of interconnected discrete material elements [15, 16].¹ These reasons motivated physicists to map the problem of the fracture mechanics of a solid onto a complex network problem. The random fuse network [6, 19], a model of the electrical breakage of a circuit network that consists of randomly failing fuses, is a prototypical model used to study the stochastic fracture dynamics of complex networks.

¹Whether a material is treated as continuous or discrete depends on the scale at which the material is being modeled, *viz.*, at a microscopic level or at a macroscopic level. A material at a microscopic scale, materials usually cannot be treated as continuous media. But on a macroscopic scale, treating materials as continuous media is acceptable and continuum models have been widely adopted [17, 18].

Other network models of practically relevant fatigue problems have also been studied, such as earthquake models [20, 21, 22] and brain neural network models [23, 24]. Furthermore, other complex networks, such as the Internet, social networks, artificial neural networks, etc. [25], and of course, the spin lattice, the most widely studied model of classical statistical physics, also reveal similarities with fracture network models, even though the difference between the fatigue systems and other complex systems is that the fracture models are mostly characterized by irreversible transformations of the network elements.

In general studies of complex networks, the order-disorder phenomena and phase transitions are of critical interest to statistical physicists. Moreover, from the perspective of complexity theory, robustness is also a vital problem that concerns how much disturbance a system can tolerate before the loss of its required function. Percolation, as a critical phenomenon, is an especially important subject. Percolation occurs when there are sufficient connections between network elements and a dominant cluster spans the whole network. An application of this is to predict the spread of infectious diseases [26]. Nowadays, with the rapid growth of computing power, Monte Carlo methods are widely adopted to simulate the stochastic processes of networks to explore these interesting phenomena [27].

In the specific context of stochastic fracture networks, the robustness of complex networks can be translated to the assessment of what physical quantities can lead the material to reach catastrophic failure, such as the analysis of the stress strength threshold of the system or the prediction of a lifetime. The percolation transition is highly relevant for assessing whether a catastrophic failure has taken place [20], since the microcracks are randomly generated over time and grow into a sample-spanning fracture.

Fracture systems also display order-disorder phenomena. The crack events exhibit both spatial and temporal correlations that are caused by a time-dependent stress field. In a weakly correlated system, these failure events are nearly completely random and the system has a high degree of disorder. On the other hand, a strongly correlated system shows more ordered breakage behaviours in which localized damage occurs at an early stage. This leads to the follow-up questions: How do we understand the transition or crossover between the two damage regimes, viz., the random breakage regime and the localization regime? What physical quantities can characterize this transition?

1.2 Fracture formation on Polymer Electrolyte Membranes

A self-assembled polymer network is a typical complex fracture network. One ubiquitous example is the scaffold of charged and elastic ionomer bundles that constitute the stable skeleton of a polymer electrolyte membrane (PEM) network.

A PEM is a vital component in PEM fuel cells (PEMFCs) and is needed in PEMFCs to transport protons and separate the reactant gases supplied at anode (hydrogen) and cathode (oxygen) sides. PEMFCs are a promising type of fuel cells and are touted for

use in automotive and backup power systems [28, 29]. As green energy conversion devices, PEMFCs could help combat global warming [30].

In PEMFCs, the fuel is hydrogen gas (H_2). As illustrated in Fig. 1.1, at the anode, hydrogen is split into protons (hydrogen ions) and electrons. In a proton-conducting PEM, the protons permeate through a network of water-filled nanopores of the network, and the electrons flow through an external circuit. At the cathode, oxygen gas (O_2) is delivered to combine with the protons and the electrons to form water molecules. In this way, the electric potential difference is maintained between the cathode and the anode, and electric power is generated. The chemical reaction equations are as follows:

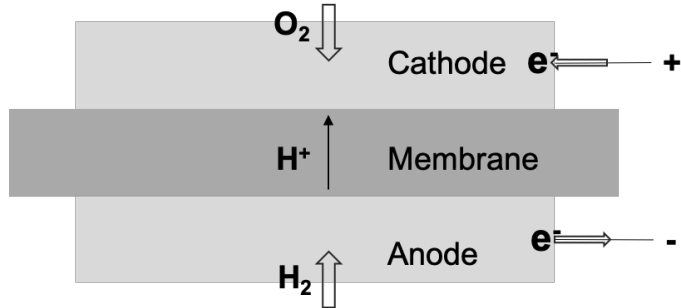
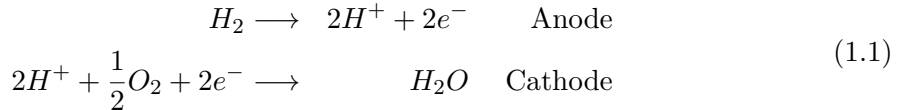


Figure 1.1: Schematic illustration of a PEM fuel cell. Hydrogen and oxygen gases are supplied from the gas compartments on the anode and cathode sides. Hydronium ions permeate through the membrane and electrons are conducted through the external circuit.

Membrane failure in PEMFCs occurs when a direct crossover of the reactive gases (hydrogen or oxygen) between the cathode and the anode. Micro-cracks initiate and grow over time [31], caused by chemical or mechanical stressors. Eventually, a sample-spanning fracture develops and reactants permeate through this fracture, resulting in voltage losses and the degradation of PEMFCs [32, 33, 34, 35]. These issues motivate us to study the fracture dynamics on PEMs and determine after what time a sample-spanning fracture occurs and what factors determine its formation.

The most commonly used membrane material is Nafion. In aqueous solution, individual Nafion ionomer backbone strands in solution assemble into cylindrical bundles. As the length of a single ionomer strand exceeds the length of a bundle, an effective cross-linked three-dimensional network of ionomer bundles and nanoporous superstructures is formed [36]. The water molecules are trapped in the nanopores. The polymer network structure and the water content in the supercells can be verified by mean-field theory [37, 38, 39, 40, 41, 42] and molecular dynamics (MD) simulations [40, 43, 44, 45]. Experimentally, X-ray and neutron

scattering techniques can be used to verify the network morphology [46]. However, even though the self-organized polymer network has a randomly disordered structure, periodic lattices are often considered in theoretical models for reasons of simplicity [47].

Micro-fractures on membranes are caused by chemical and mechanical degradation mechanisms. Chemical degradation has been widely studied [48]. For the mechanical degradation that we study in this work, fractures on bundles are induced by the pressure of the water phase in the nanopores. Moreover, under typical operating conditions in PEM fuel cells, PEMs are subject to fluctuations in temperature as well as cyclic relative humidity. In other words, PEMs undergo the cycles of water sorption and desorption, inducing cyclic stresses in the membrane [49]. As indicated in Refs. [50, 51, 52], a Nafion membrane in a cell has a lifetime up to 20 000 hours. To study the lifetime of PEMs experimentally, accelerated stress testing (AST) is adopted to simulate the PEMs under cyclic stresses in real-world conditions [53, 54]. The fracture concentration in the membrane can be detected by X-ray beams [55, 56]. Fig. 1.2 taken from Ref. [57] shows an X-ray computed tomography image of fracture on a Nafion-type polymer membrane from pristine beginning-of-life (BOL) condition to thousands of wet/dry cycles. As indicated in Ref. [57], micro-cracks start between 2000 and 4000 cycles, but the sample-spanning cracks occur between 4000 and 4500 cycles.

1.3 Challenges

The motivation that drives this work is to develop the ability to make predictions of the lifetime of polymer electrolyte membranes. In view of this overarching goal, we strive to understand the fracture mechanics from the general statistical physics aspects and apply it to the fracture dynamics of PEMs. We map the damage dynamics of PEMs onto a bond percolation model of fracture. The stochastic fracture process on the network is simulated by a kinetic Monte Carlo method.

In Ref. [58], stochastic fracture dynamics of completely random behaviour on the bundle network were studied by Melchy and Eikerling. However, in a real PEM, the bundle breakage events are correlated both spatially and temporally. In the correlated case of a fracture dynamics problem, the probability of a bundle failure in a stochastic sequence of breakage events can be described as a function of the updated stress field after a bundle fails. From this, we ask, what is the functional form of this stress-dependent bundle failure probability? More importantly, how does the stress redistribute within the remaining intact parts of the network after a bundle failure?

In general studies of stochastic fracture models, the stress field redistribution rule is often treated as a way in which the remaining intact parts of the material receive the additional stress from the crack tips. The two widely studied stress transfer models are equal load sharing (ELS) and local load sharing (LLS). ELS assumes a mean-field limit that every surviving bundle receives the exact same fraction of the load, whereas LLS assumes

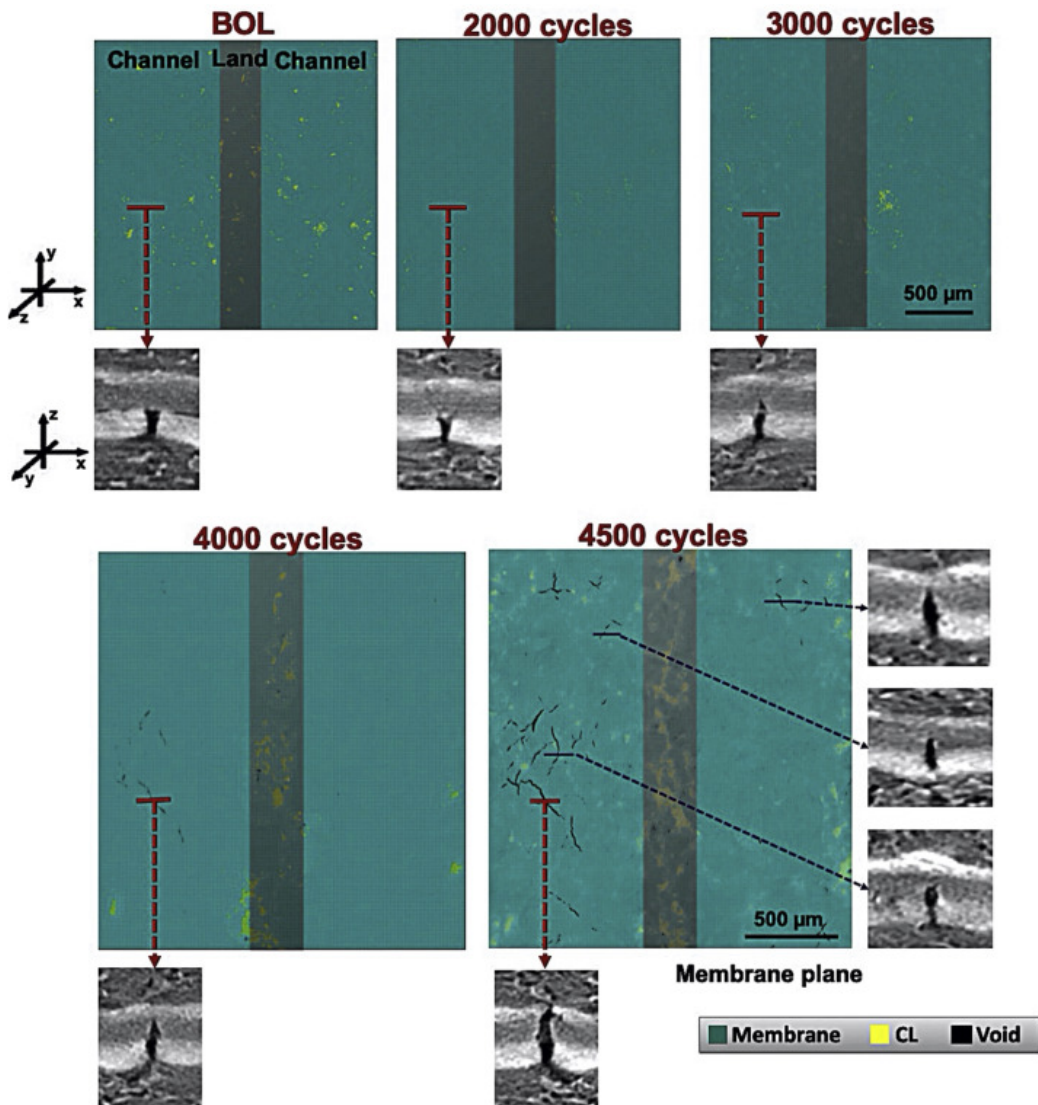


Figure 1.2: X-ray computed tomography images of the fatigue propagation tracking of an identical area of a Nafion-type membrane plane from beginning of life (BOL) condition to thousands of wet/dry cycles. The insets represent the corresponding cross-sectional views at the indicated membrane locations. Reprinted from International Journal of Hydrogen Energy, 45, D. Ramani *et al.*, 4D in situ visualization of mechanical degradation evolution in reinforced fuel cell membranes, 10089 - 10103, Copyright (2020), with permission from Elsevier.

that only the nearest neighbours take the load. These two limiting regimes correspond to an uncorrelated system and a correlated system, respectively. However, the stress transfer scheme of a real material is most likely to fall in between the two limits. The stress transfer scheme for a polymer network of the PEM is especially more complicated because the stress field is caused by the internal swelling pressure [59].

Once a suitable stress redistribution scheme is adopted, we can explore the percolation phenomenon, the lifetime, and the crossover between the two damage regimes, viz., the random breakage regime, and the localization regime. These are not only of practical interest, but they also provide insights from the perspective of statistical physics. Moreover, understanding the percolation behaviour in a fracture system is of particular importance. In Chapter 2, a more detailed review of fracture dynamics as well as percolation theory will be revisited.

1.4 Dissertation Organization

This thesis is divided into seven chapters, the contents of which are as follows:

Chapter 1: Introduction. This chapter provides context and practical motivation for the presented research.

Chapter 2: Theoretical Background and Related Studies. This chapter shows theoretical background of statistical fracture dynamics and percolation theory. Related studies or progress will be discussed.

Chapter 3: Model. This chapter presents the framework of the model in this present work. Fracture processes on PEM networks are mapped to a dynamic percolation model on a lattice. The correlation of fractures in the breakage sequence is described by both the breakage rate and the stress redistribution law.

Chapter 4: Computational Approach and Methods. This chapter presents the context of a (rejection-free) kinetic Monte method and an algorithm of the identification of the onset of percolation, both of which are adopted in the kinetic simulation of the dynamic fracture process of the membrane polymer network. The detailed simulation procedures are also presented.

Chapter 5: Results: Fracture Regimes and Percolation Behaviour at a Fixed Lattice Size. This chapter presents the Monte Carlo results for a lattice of fixed size. Fracture regimes, viz., the random breakage regime and the localization regime, and the peculiar percolation behaviours are of particular importance in our present work. Also, a lifetime analysis of PEMs is presented.

Chapter 6: Results: Analysis of Finite Size Effects. This chapter extends the results of Chapter 5 to lattices of varying sizes.

Chapter 7: Conclusions and Outlook. This chapter presents a summary of the findings in this work, as well as possible extensions for future study.

Chapter 2

Theoretical Background and Literature Reviews

A self-assembled polymer network exhibits a complex fracture behaviour. The fracture events on the network are characterized by randomness and thus can be interpreted from the perspective of statistical physics. Several physical phenomena emerge during nucleation and growth of a fracture. Among these, the percolation behaviour is of particular importance as it is concerned with the growth and merging process of cracks.

In Section 2.1, the concept of the crack nucleation and growth regimes in fracture disordered systems will be reviewed. Spinodal nucleation will be briefly introduced to understand the nature of the nucleation process in the statistical physics picture. The correlations in fracture systems are characterized by the redistribution laws of the stress field. To describe the dynamic process, two widely used rules of breakage rates will be reviewed.

In Section 2.2, I will first present classical uncorrelated percolation theory and then proceed with the investigation of several prototypical spatially correlated percolation models.

2.1 Fracture Disordered Systems

Fractured phenomena have drawn the attention of statistical physicists for the past 40 years [6, 7, 8, 9, 15]. The fracture propagation process is characterized by randomness, thus the system exhibits a certain extent of disorder. Therefore, fracture systems can be interpreted as disordered media. In a disordered system, the degree of randomness is reduced due to ordering behaviour that occurs through interactions or correlations. As a result, several critical phenomena emerge. A typical example of a disordered system is a spin system – one of the most classical systems in statistical physics. As for disordered systems considered in fracture mechanics, the Random Fuse Model (RFM) [6, 60, 61, 62] and the Fiber Bundle Model (FBM) [63] are two prototypical approaches. An RFM represents a network of fuses with random thresholds of strength subjected to an external current. In an FBM, a collection

of parallel fibers is clamped into a bundle with the conserved tensile stress applied vertically to the plane.

The above classical models are associated with microscopic random discrete states, that can be represented by -1 or 1. One key difference between a fracture system and an Ising model is that a fracture system starts with a fully intact network, in which all the network elements take the state of 1 (in the spin analogy), and once it begins to fracture, these elements normally flip *irreversibly* to the -1 state. We also address here that our model of the self-assembled polymer network is effectively modeled within the same framework as an FBM, whose very spirit is that the stress dissipation is zero.¹

An order parameter can quantify the extent to which a phase is ordered or disordered. In an RFM or fibrous fracture systems [47, 64], a commonly used order parameter is the conductivity. In this regard, the system's global failure is identified when the conductivity decays to zero. In our case, however, global breakdown is defined when the system is percolated by a crack. Later in Chapter 5, a new order parameter based on the distribution of percolation thresholds in our results will be presented.

2.1.1 Crack Nucleation and Growth

Fracture dynamics proceeds essentially as a crack nucleation and growth process. What is a nucleation regime? Nucleation commonly exists in nature. One classical example of nucleation is the initial formation of bubbles in heated water as it evolves into a new stable phase, viz. the vapour, once the barrier in free energy is overcome. As an analogy, the "bubble" nucleation and growth can be described as the cluster generation (a) and growth (b) respectively, as illustrated in Fig. 2.1.

In a thermally activated fracture system under stress, microscopic fractures first nucleate randomly and later cracks grow along the edges of the initial nuclei in a correlated manner. Eventually, the damage regime of localization is strong enough to transform the system to complete failure in short time. From a statistical physics point of view, the nucleation process involves a shift from a metastable state to a new stable state of global failure [9]. One interpretation of the process can be through spinodal nucleation, following the logics of Landau-Ginzburg mean-field theory [7, 9, 65]. In this context, a local minimum of the free energy disappears, at the spinodal point, resulting in the system transitioning to a lower minimum in the free energy, corresponding to another stable state as illustrated in Fig. 2.2.

To note, the application of spinodal nucleation theory to crack propagation is still controversial. Kun *et al.* [63], in their numerical work, reported that the spinodal point can

¹Admittedly, a polymer network is complex in the sense that a self-assembled network consists of two parts, namely, the fiber-bundle and the bundle-network. Furthermore, the stress field redistribution caused by swelling is also intriguing. See more discussions in Chapter 4.

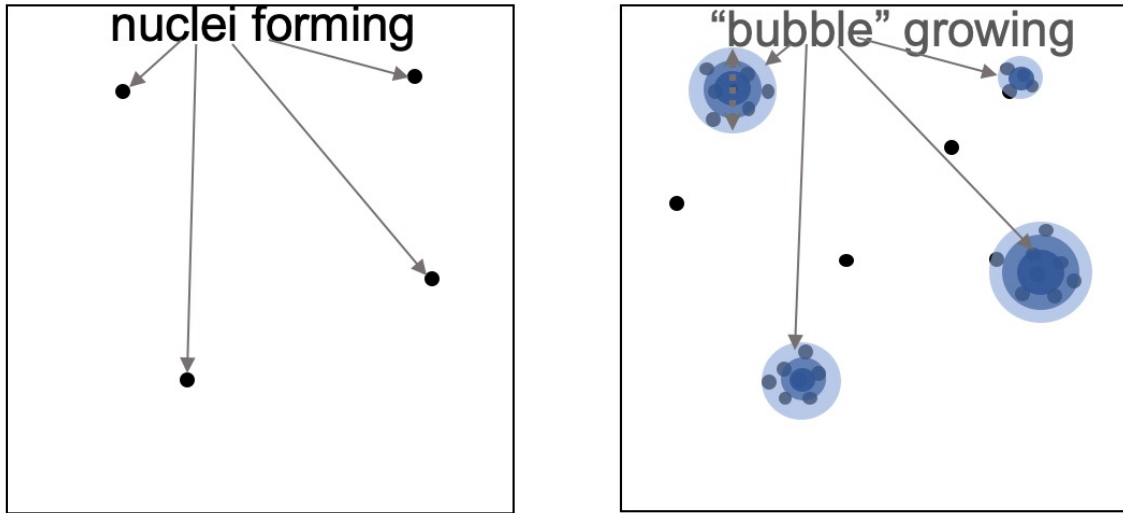


Figure 2.1: Illustrations of (a) nucleation and (b) growth. A disordered system which shows a nucleation regime should undergo the stage of random formation of nuclei and the later stage of correlated "bubble" growth around existing nuclei, while further nuclei continue to be formed.

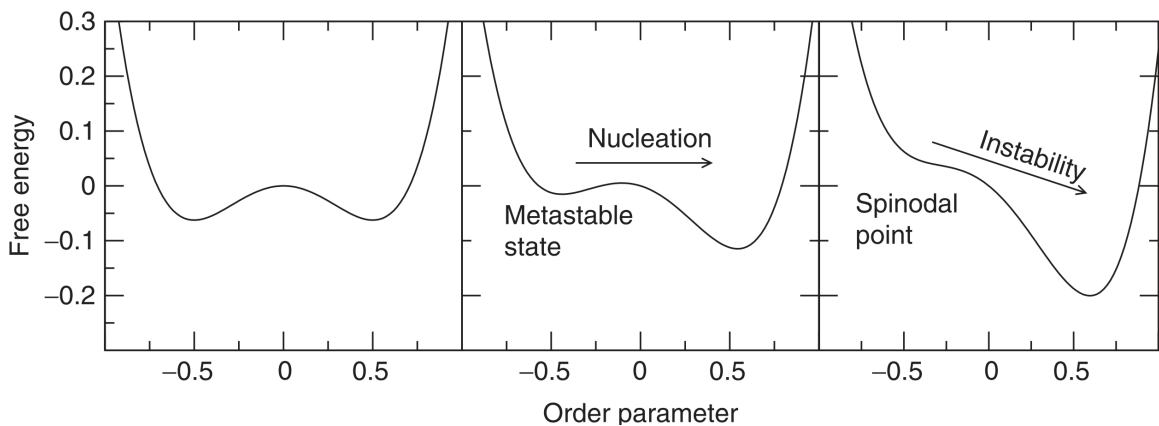


Figure 2.2: Free energy representation of spinodal nucleation. In the absence of an external field, the system has two stable states (left panel). In the presence of a field, one of the two minima shifts up and this state becomes metastable, inducing nucleation (middle panel). When reaching the spinodal point, this minimum disappears and the state becomes unstable (right panel). Reprinted figure with permission from Ref. [66] Copyright (2006) by Taylor & Francis.

never be reached until final collapse, but can be approached by increasing the range of interactions to a limit of global range or a mean-field limit [67, 68]. An avalanche, whose size distribution of bursts is characterized by a power-law functional form, is believed to be a precursor to indicate whether a spinodal point is reached [63, 69, 70].

Another question is whether there is a phase transition between two fracture regimes: the percolation-type (random breakage) regime and the localization (correlated crack growth) regime. The percolation-type regime corresponds to the limit of infinite disorder [19, 71] as the material elements break completely at random. The localization regime is an unstable state decaying rapidly to the final catastrophic failure. It shows a finite (or even infinitesimal) disorder because the process displays phenomena of correlated localized damage growth. Theories of Rundle and Klein [7] predicted a first-order phase transition between the two regimes as their order parameter shows a discontinuity; but Refs. [72, 73] assumed that it is a second-order phase transition. More strikingly, the theoretical analysis of Ref. [74] concluded that it is just a crossover between regimes, but not a real transition between two phases as neither a discontinuity nor a divergence of the derivative of the order parameter were found.

2.1.2 Load-transfer Laws

As described above, fracture disordered systems under interaction laws of varying range exhibit distinct physical phenomena. Interactions are represented through load-transfer mechanisms. In an RFM, the current load is recalculated through Kirchhoff's equations after one or a few fuses fail. As for an elastic fracture system, the stochastic sequence of fracture events is subjected to a stress field, which is reconstructed following each failure event. We could simplify the stress field redistribution by assuming the load added on other surviving material elements (fibers in an FBM or bundles in a bundle-network model) are solely transferred from the failure element. Two extensively studied rules of load sharing are equal load sharing (ELS)[75, 76, 77], and local load sharing (LLS) [75, 78, 79], corresponding to the two limits of load transfer. In ELS, all intact elements receive exactly the same load from the breakage of an element. This case corresponds to the mean-field limit and it can be solved analytically [58, 80, 81]. For LLS, only the nearest neighbours (or next nearest neighbours) receive the load. In real materials, the stress redistribution should fall in between the two extremes [82]. Motivated by this, Hidalgo *et al.* [82] proposed a stress transfer rule in an FBM which exhibits a power-law-type spatial decay,

$$\sigma_{\text{add}} \sim r^{-\gamma}, \quad (2.1)$$

where σ_{add} is the load added on a survived element at a distance r from the failed element, and γ describes the effective range of load transfer. Equation (2.1) gives the limits of the ELS for $\gamma \rightarrow 0$ and the LLS for $\gamma \rightarrow \infty$.

2.1.3 Weibull and Gumbel Strength Distributions (Power-law and Exponential Decay Rates)

The fracture process can be described as a sequence of stochastic bundle breakage events. There are two different models that treat the fracture process in different perspectives: the static model and the probabilistic model [83]. In our present work, we adopt the probabilistic way to model the fracture dynamics process.

In a static model, the elements only fail when the load borne by them exceeds their strength thresholds. Once these thresholds are randomly assigned to each material element, the elements will fail in a deterministic order [82] according to certain cumulative distribution of failure strengths. The two commonly used strength distributions are the Weibull distribution,

$$P_W(\sigma) = 1 - e^{(-\sigma/\sigma_0)^\rho}, \quad (2.2)$$

where ρ is the Weibull index, which characterizes the degree of disorder in the system; and the Gumbel distribution (double exponential distribution),

$$P_G(\sigma) = e^{-e^{-\beta(a\sigma-E_a)}}, \quad (2.3)$$

where $\beta = 1/(k_B T)$ with Boltzmann constant k_B , E_a is the activation energy, a is a positive coefficient .

On the other hand, in the probabilistic model, the fracture process can be interpreted as a Markov chain [83]. In a Markov chain model, the occurrence of the next random fracture state is dependent on its current state, which includes the present network of remaining intact elements, the current load field and the ongoing failing element. If only one failure event of a certain material element occurs at a time, its probability is proportional to its decay rate subject to the load σ on it,

$$p\{\text{failure at } \mathbf{x} \mid \text{current network structure, load field, ongoing failing element}\} \propto \kappa(\sigma(\mathbf{x})). \quad (2.4)$$

Now it comes to the question of an appropriate form of the failure rate $\kappa(\sigma(\mathbf{x}))$ as a function of the load. Two functional forms are widely employed: the power-law breakdown rule,

$$\kappa_p(\sigma) \propto \left(\frac{\sigma}{\sigma_0}\right)^\rho, \quad (2.5)$$

with the positive constant σ_0 ; and the exponential breakdown rule ²,

$$\kappa_e(\sigma) \propto e^{\beta(a\sigma-E_a)}. \quad (2.6)$$

²Equation (2.6) assumes $n = 1$ in $\kappa_e(\sigma) = e^{\eta\sigma^n}$ which is supported by a number of experiments; whereas in some studies n is assigned the value of 2 [8].

The two breakdown rules above, Eqs. (2.5) and (2.6), are related to the Weibull distribution (Eq. (2.2)) and the Gumbel distribution (Eq. (2.3)), respectively. The relations between strength distributions $P(t; \sigma(t))$ and the corresponding decay rate $\kappa[\sigma(\tau)]$ can be established as follows [80, 84]³,

$$P(t; \sigma(t)) = 1 - \exp \left\{ - \int_0^t \kappa[\sigma(\tau)] d\tau \right\}. \quad (2.7)$$

Both, the power-law and the exponential forms of decay, have been adopted in the past to describe the molecular breakage events of fibers [86]. For a fiber, which undergoes a thermally activated process, clearly the exponential form of the rate better describes the statistical breakdown behaviour since it contains the Boltzmann factor. On the other hand, the power-law form of decay, which has been widely adopted in the fracture studies [19, 82, 87], is credited for its consistency with a well-known empirical distribution – the Weibull distribution. The Weibull distribution has traditionally been used to fit experimental strength data on elastic fibers, but theoretical and numerical studies suggested that a Gumbel distribution overall better fits the numerical data [88, 89], at least for some regions in parameter space [90, 91]. Experimental results as claimed in Ref. [92] showed the Gumbel distribution is a better description of the nature of fiber strength.

Nevertheless, the power-law form can still locally approximate the exponential case [86, 93]. Also, the power-law breakdown rule has a simple size scaling form whereas the exponential-law breakdown rule is unlikely to have such a form. [86]. A scaling theory which describes a transition between fracture regimes proposed by Shekhawat *et al.*[19] is based on the assumption of the Weibull distribution (Fig. 2.3). In our study, we employ the exponential breakdown rule for the material elements (bundles) in the disordered network to observe whether a qualitatively different fracture behaviour can be observed.

Another remark relates to the difference between static and probabilistic methods of failure process simulations. In the static approach, a material element only fails when the load exceeds its strength threshold. For a specific initial load, all the elements of the system may eventually completely break down, or reach an equilibrium when the remaining elements can survive with the loads below their strength thresholds [82]. The probabilistic method on the other hand relies on the decay rates of elements that describe the finite failure probabilities of these elements for a given time period. Thus all elements will finally fail given long enough time. In our present work, the fracture process is modeled by the probabilistic method and is simulated by a kinetic Monte Carlo method that will be introduced and further discussed in Chapter 4.

³It can be derived from $-dn = n(\tau)\kappa[\sigma(\tau)]dt + \mathbf{o}(d\tau)$, where n represents the surviving elements. The accumulative failure distribution $P(t)$ is equated with $1 - n(t)/N$, where N is the total number of elements [85, 80].

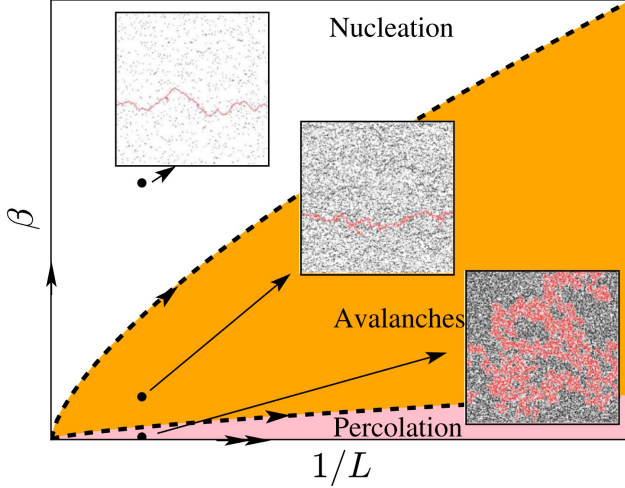


Figure 2.3: A phase diagram of random breakage (percolation-like) regime to nucleation (localization) regime for a random fuse network. The phase transition was studied based on a scaling theory and an assumption of the Weibull strength distribution. Reprinted figure with permission from Ref. [19] Copyright (2013) by the American Physical Society.

2.2 Percolation Theory

Percolation theory has been applied in many disordered systems to study the connectedness of clusters for practical purposes. Applications vary from forest fire models [94, 95, 96], earthquake predictions [21, 22], epidemic spreading analysis [26], and liquid penetration analysis for porous media [22]. In statistical physics, percolation phenomena have also been shown to relate to the critical behaviours in Ising models [97, 98]. Fracture dynamics are undoubtedly relevant to percolation studies, as during the fracture process, the randomly generated cracks merge over time and eventually develop a sample-spanning fracture.

This section starts with a simple introduction to uncorrelated percolation theory. In real systems, however, the random variables are interacting or correlated in the dynamic process. Correlated percolation, as a more practical case, will be discussed in Section 2.2.2.

2.2.1 Uncorrelated Percolation

Uncorrelated percolation is a classical, simplified version of the percolation model, which disregards interactions between the elements in a disordered network. Stauffer [99] has explained the basic spirit of uncorrelated percolation theory: sites (site percolation) or bonds (bond percolation) on a lattice are randomly and independently occupied with probability p (or empty with probability $1 - p$). Groups of sites/bonds are occupied and connected through bonds/sites⁴, forming clusters. Upon reaching a critical probability p_c from below,

⁴In principle, a bond percolation problem can be transformed into a site percolation problem through bond-to-site transformation [100]. For example, the square lattice bond percolation problem can be treated

a cluster forms that spans the lattice, leading to a macroscopic critical phenomenon, i.e., percolation. For infinite lattices, when increasing p to p_c , the probability of forming at least one percolating cluster changes abruptly from 0 to 1 as depicted in Fig. 2.4 (a). The critical value p_c is known as the percolation threshold.

Exact analytical solutions for p_c have been found for several lattices: the site percolation threshold for the triangular lattice and bond percolation threshold for the square lattice, triangular lattice and honeycomb lattice [94, 101]. The reader can refer to Table 2.1 for site or bond percolation thresholds for selected two-dimensional or three-dimensional lattices.

Table 2.1: Site or bond percolation thresholds for the square lattice (2D), triangular lattice (2D), honeycomb lattice (2D) and simple cubic lattice (3D).

Lattice	p_c , site	p_c , bond
square lattice	0.593 [102, 103, 104] [†]	0.5 *
triangular lattice	0.5 *	$2 \sin(\pi/18)$ *
honeycomb	0.697 [105, 106] [†]	$1-2 \sin(\pi/18)$ *
simple cubic	0.312 [107, 108] [†]	0.248 [109, 110] [†]

* analytical result

† numerical result

Several critical phenomena occur in the vicinity of the percolation threshold for the cluster structures of the lattice, similar to the Ising model at the critical temperature. Some of the cluster structures can be analyzed by the k^{th} moment of the distribution n_s of cluster size s ,

$$m_k = \sum_s s^k n_s. \quad (2.8)$$

Stauffer has explained the critical phenomena of the cluster structures by showing the scaling relations in Ref.[94]. Those are:

m_0 , the total number of clusters,

$$M_0(p) \propto |p - p_c|^{2-\alpha}, \quad (2.9)$$

m_1 , the total number of occupied sites,

$$m_1(p) \propto (p - p_c)^\beta, \quad (2.10)$$

m_2 , the mean cluster size,

$$m_2(p) \propto |p - p_c|^{-\gamma}, \quad (2.11)$$

as a self-matching site percolation problem. To avoid being overly verbose, I will use the language of site percolation to explain the concept of percolation theory in this section.

ξ , the connectivity length,

$$\xi(p) \propto |p - p_c|^{-\nu}, \quad (2.12)$$

and,

$$\sum_s s \cdot n_s e^{-hs} \propto h^{1/\delta}, \quad (2.13)$$

where h is real number.

Any two of the five critical exponents $\alpha, \beta, \gamma, \delta, \nu$ in scaling equations are related to each other in d dimension lattices via the three scaling laws

$$2 - \alpha = \gamma + 2\beta = \beta\delta + \beta = d\nu, \quad (2.14)$$

Thus, once two of them are determined analytically or numerically, the other three can be obtained. For most two-dimensional lattices⁵, including square, triangular and honeycomb lattices, the scaling exponents have been exactly solved with $\alpha = -2/3$, $\beta = 5/36$, $\gamma = 43/18$, $\delta = 91/5$ and $\nu = 4/3$ [99]. Three-dimensional lattices, such as a cubic lattice, have $\alpha = -0.6$, $\beta = 0.4$, $\gamma = 1.8$, $\delta = 5.3$ and $\nu = 0.9$, which were determined numerically [99].

To note, the connectivity length ξ represents the average radius of a typical percolation cluster. As it characterizes the correlation between occupied sites, some studies used to refer to it as the correlation length. To differentiate it with the correlated length in correlation functions defined in the correlated percolation models introduced in Section 2.2.2, we will continue referring to ξ as the connectivity length.

Kinetic Percolation

Classically, the uncorrelated percolation is as defined above, in which p is the occupation probability of every site in the lattice and we can call this "ordinary" version of percolation model as the static percolation model. However, the kinetic version of the percolation model [114, 115] is more applicable for describing dynamic processes. Sites are added one by one randomly in the kinetic percolation model, in which p_c is defined as the critical concentration, i.e., the proportion of the occupied sites, which must be filled to create a percolating cluster. Numerical simulations show the values of p_c defined in the two respective models are statistically equivalent⁶. In this thesis, we adopt the kinetic percolation model to describe

⁵A Cayley tree has $\alpha = -1$, $\beta = 1$, $\gamma = 1$, $\delta = 2$ and $\nu = 0.5$ [111, 112, 113].

⁶Numerical simulations approaching the infinite size limit so far support such an equivalence, but a strict mathematical proof of the equivalence of the two definitions of p_c could not be found. Even though the concentration can in theory take values less or more than the occupation probability p in the static model, the main factor that affects the percolation behaviour is still the permutation of the spatial structure of the occupied sites at the same concentration. Moreover, as the lattice size approaches the limit of infinity, the concentration matches the probability p of the lattice.

the fracture process and the percolation threshold p_c is defined as the concentration in the dynamic process.

Finite-sized Lattices

Now we wonder what is the wrapping probability R , i.e., the probability of forming a percolating cluster, as a function of the concentration p in finite-sized lattices. Unlike infinite lattices (Fig. 2.4 (a)), Fig. 2.4 (b) shows a continuous transition of R from 0 for $p = 0$ to 1 for $p = 1$. One can imagine the following rare cases: for low p close to 0, there is a chance of generating a percolating cluster of a single row (or similar phenomena); and for p close to 1, the sites are occupied almost everywhere but they might still not be connected together to become a percolating cluster. However, as the size of lattices grows, the chance of the above rare cases becomes vanishingly small, and eventually when reaching an infinite size limit, R transforms to a step function as shown in Fig. 2.4 (a).

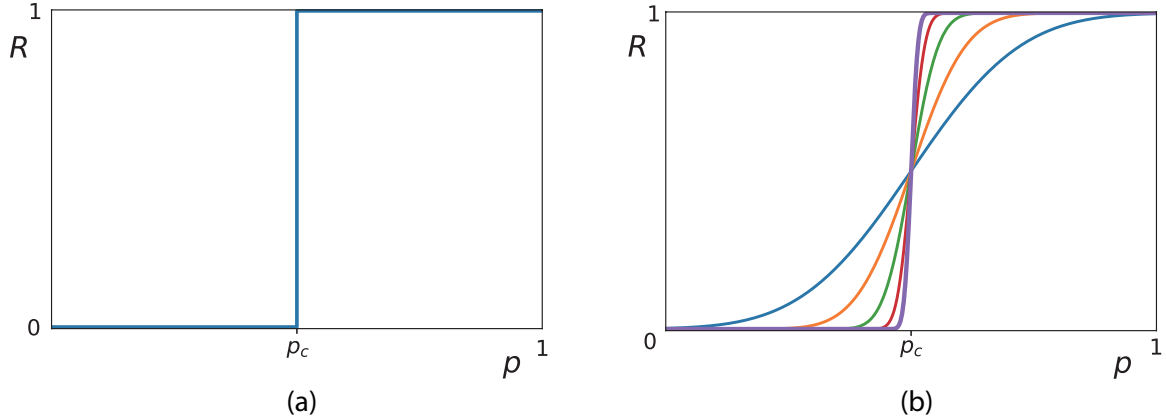


Figure 2.4: Wrapping probability R as a function of the concentration (or occupation probability) p . (a) For an infinite lattice, R exhibits a step-like change from 0 to 1 at the percolation threshold p_c . (b) For finite lattices, R changes continuously. While L increases (blue, orange, green, red and purple), the transition region of R becomes steeper in the vicinity of p_c .

In a kinetic percolation model, the percolation threshold p_c^L for a finite lattice of linear size L , can be defined as the concentration p at which a percolating cluster first appears [99, 116, 117]. In a probability distribution of p_c^L , the probability that p_c^L takes a value at p is proportional to $\frac{dR}{dp}$. Fig. 20 in page 76 of Stauffer's book (1985) [99] (Fig. 2.5) discusses the relation between the wrapping probability R and the probability distribution of p_c^L . Accordingly, the average percolation threshold can be defined via

$$p_{\text{av}}^L = \int p_c^L \left(\frac{dR}{dp} \right) dp_c^L. \quad (2.15)$$

For some lattices, for example a cubic lattice, the site or bond percolation threshold cannot be solved analytically; p_c can be obtained, however, numerically and by fitting the simulation data to the finite-size scaling equation [99, 117]⁷,

$$p_{\text{av}}^L - p_c \sim L^{-1/\nu}. \quad (2.16)$$

For an uncorrelated percolation model, the probability distribution of p_c^L follows a Gaussian-like behaviour. Furthermore, the width of the distribution decreases with increasing L , approaching a δ -function-like distribution when $L \rightarrow \infty$. In contrast, for the fracture-type correlated percolation system considered in this work, the distribution of percolation thresholds exhibits unusual behaviours at the onset of the localized damage regime, which will be shown in Chapter 5.

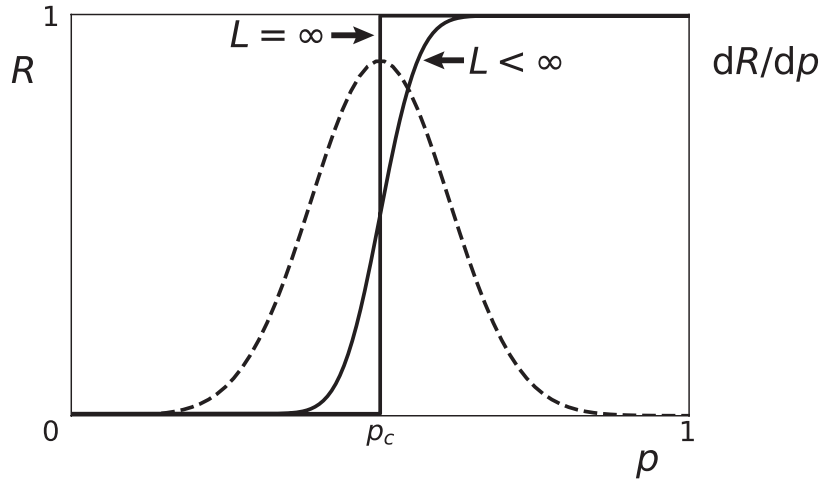


Figure 2.5: Wrapping probability R (solid lines) for finite-sized lattices and infinite-sized lattices. The dashed line represents dR/dp , proportional to the probability that at concentration p a percolating cluster appears for the first time. When $L \rightarrow \infty$, dR/dp approaches the Dirac δ function. Reproduced (qualitatively) according to Fig. 20, page 76 in the book of Stauffer (1985) [99].

2.2.2 Correlated Percolation

An uncorrelated percolation model is over-simplified for real systems in which the random variables are interacting and correlated. Fracture systems clearly fall into the category of correlated percolation problems.

Here we introduce a prototypical long-range correlated percolation model, which has been extensively studied for theoretical purposes [118, 119, 120, 121]. In this model, $u(\mathbf{r})$

⁷Likewise, other physical observables like the wrapping probability R , the connectedness length ξ and average size S also exhibit finite-size scaling properties. Please refer to Refs. [99, 117]

represents a site that has one of the binary states of (-1, 1), corresponding to the empty or occupied states. The correlation functions $\langle u(\mathbf{r})u(\mathbf{r} + \mathbf{R})\rangle$ are defined to follow spatial decays which can take power-law, exponential, or Gaussian forms, with a correlation length λ :

$$\langle u(\mathbf{r})u(\mathbf{r} + \mathbf{R})\rangle \sim |\mathbf{R}|^{-\lambda}, \quad (2.17)$$

$$\langle u(\mathbf{r})u(\mathbf{r} + \mathbf{R})\rangle \sim e^{-|\mathbf{R}|/\lambda}, \quad (2.18)$$

$$\langle u(\mathbf{r})u(\mathbf{r} + \mathbf{R})\rangle \sim e^{-|\mathbf{R}|^2/\lambda^2}. \quad (2.19)$$

The process behind this model is modelled with a Markov chain Monte Carlo (MCMC) model [117]. Given a copy of a statistical ensemble, for example one with a particular MC configuration of the correlation length λ and an occupation probability p , the simulation starts with an initialization of a random occupation of a spatial lattice. Next, a new spatial lattice structure will be calculated according to the transition probability matrix or the Fourier transform and this procedure is repeated until the system reaches equilibrium, at which point one can observe whether the lattice is percolated for the given copy. Once this process is done for many MC realizations, we can obtain a wrapping probability R , in terms of parameters of λ and p .⁸

A general intuitive expectation is that the percolation threshold decreases with stronger correlation [91] as the connectedness is stronger between clusters. Such a phenomenon was first reported in an early model of a continuum correlated percolation system [125]. For long-range discrete models, a similar conclusion was also reached in Refs. [123, 126], but this can be limited to the observations of a small range of correlation lengths. Later, Harter in his work [117] showed that the percolation thresholds reduce but will increase again for sufficient correlation length.

To note, the prototypical correlated percolation model introduced in this section is of the most standard form, and is usually studied for theoretical interest. However, for solving some more particular problems, different correlated percolation models are specifically considered, such as the directed percolation model for the flow penetration in a porous medium [98] and bootstrap percolation for the neuronal activity [127]. For the correlated percolation model of the "fracture-type", one typical characteristic is that all material elements start with an intact (micro-)state of 1, and once the elements fail, they flip to 0 *irreversibly*. As a comparison, the random state of $u(\mathbf{r})$ in the "standard" correlated percolation model can flip back at each step in the Markov process. Furthermore, the correlation function in the "standard" correlated percolation model is clearly defined as in Eq. (2.17) to (2.19),

⁸For detailed simulation procedures, please refer to Ref. [122] and Refs. [123, 124].

etc. However, in a fracture-type percolation system, the correlation is characterized by the stress field redistribution, but a correlation function cannot be formulated so far. Moreover, correlation between the fracture events appears to grow over time. The reader will see an unusual percolation variation in the results in Chapters 5 and 6 that can be compared to the percolation behaviours observed in Refs. [91, 117, 123, 125, 126]. However, it is unknown whether the different percolation behaviour is caused by intrinsic differences between the standard correlated percolation models and the fracture-type correlated percolation model considered in this work.

Chapter 3

Model

This chapter discusses the framework of the model studied in this thesis. The fracture problem of a self-assembled polymer electrolyte membrane (PEM) can be broken down into two parts: the decay rate or lifetime for a bundle of ionomer fibers and the stress field redistribution law for the bundle-network model. Once the above two essentials are obtained, we can numerically simulate the dynamics of failure events in the network as a Markov process using Monte Carlo methods (this will be further introduced in Chapter 4).

3.1 Overview

Compared to the simple prototype fiber bundle models (FBMs) (see Section 2.1), the fracture problem of a PEM is more convoluted owing to the complex polymer network structure and the internal stress field that is caused by the swelling pressure upon water uptake. Individual ionomer backbone strands in solution assemble into cylindrical bundles, as seen in calculations based on mean-field theory [37, 38, 39, 40, 41, 42] and molecular dynamics (MD) simulations [40, 43, 44]. The length of a single ionomer strand exceeds the length of a bundle, giving rise to effective cross-linking of ionomer bundles, that results in the formation of a mechanically stable network [36]. The above description is illustrated in the first two subfigures (from the left) on the upper rail in Fig. 3.1. The network is randomly self-organized subject to water uptake; the structure thus exhibits a certain degree of disorder, but the symmetry in some local areas of the network has been observed [128]. The local symmetry can be extended to "global symmetry" for theoretical interest [47, 129]. Motivated by this, Ioselevich *et al.* proposed a model of the three-dimensional (3D) crystalline lattice of "cages", made of cylindrical bundles (see Fig. 3.2). Water molecules are trapped inside the cages of cylinders [130, 131]. Thus Ioselevich *et al.* treated the water clusters as spherical droplets in their models [47, 132]. The stress field of the lattice, which triggers bundle breakage events, is created as a result of the swelling pressure corresponding to equilibrium water sorption. Furthermore, the stress field is reconstructed due to breakage of bundles in the cages, thus the initially assumed-to-be uniform stress field evolves to become more

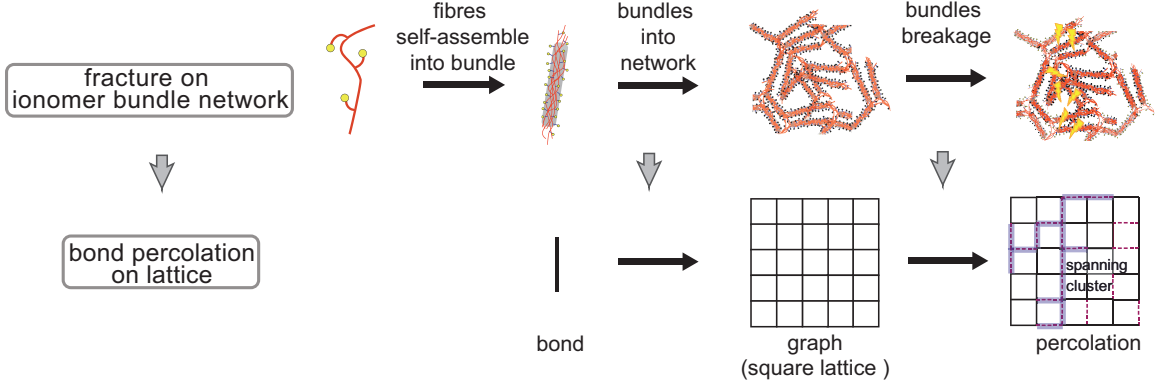


Figure 3.1: Ionomer fibers with hydrophobic backbone (red) and grafted sidechains (red) terminated with sulfonic acid head groups (yellow) that dissociate in water. The upper rail illustrates self-aggregation into bundles of size k (number of fibres in the bundle) and cross-linking into a network. In the swollen membrane state, bundles experience an internal swelling stress that triggers random breakage events. The lower rail illustrates how fracture formation in the bundle network is mapped onto a dynamic bond percolation problem.

and more nonuniform over time. This makes the probability of bundle breakages in the failure sequence unequal and effectively creates a correlation or dependence between the breakage events of the neighbours and other surviving bundles. Fracture formation in the bundle-network model is the consequence of individual bundle breakage events that occur randomly in space and time. Over time, clusters of broken bundles, representing microscopic cracks, grow and increase in density. At a certain time, a percolating cluster of broken bundles will emerge, corresponding to a fracture that spans through the membrane. Hence, the bundle-network model can be mapped to a bond percolation, where the occupied bond represents a bundle failure as shown in Fig. 3.1. A previous percolation model of PEM was studied by Melchy and Eikerling [58], in which the bundle breakage events were simplified as being independent, thereby representing the limit of uncorrelated percolation. The PEM lifetimes were given as a function of the percolation threshold. This model is relevant in a regime where there is low water uptake by the PEM and thus weak swelling stress exerted on pore walls and bundles. However, bundle breakage events could also happen in a highly correlated manner, which is expected in the strong stress regime encountered at large swelling. In this regard, the PEM lifetimes predicted in Ref. [58] were overestimates. In our present work, we attempt to extend the model in Ref. [58] to a correlated case. We consider the bond percolation model in which the correlations exist in the dynamic breakage processes and the correlations between the breakage events are caused by the stress field redistribution. Effectively, the redistribution of the stress field is treated as the load transfer from the failing bundle to other intact bundles in the network.

The stable bundle size, given by the number k of strands in a bundle [133, 36], results from competing effects of backbone hydrophobicity and electrostatic repulsion due to

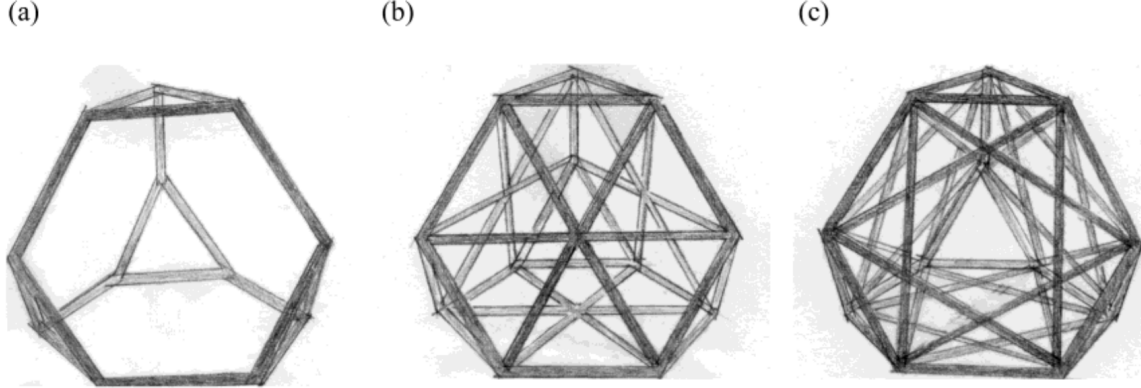


Figure 3.2: In the model by Ioselevich *et al.*, the fiber-bundle-network for PEM is constructed of an ordered structured network of cages, made of cylindrical bundles. The water clusters are treated as spherical droplets inside the cages, creating pressure on the bundles that form the cages. As the stress on bundles is generated internally by water uptake and swelling, it will usually not be conserved within the network over time. Reprinted (adapted) with permission from Ref. [47] Copyright (2004) American Chemical Society.

charged ionic end groups at grafted ionomer side chains, favouring dispersion of ionomer chains in solution. In the model in Ref. [58], a bundle is assumed to be failed once all of the ionomer fibers fail. The swelling pressure is applied to the wall of a cylindrical bundle in PEM (Fig. 3.3 (b)). The scalar quantity of the swelling stress tensor on the bundle can be computed from the Cauchy stress tensor and this scalar value of stress is the so-called von Mises stress [134, 135]. As the swelling stress on bundles evolves, the stress load as the scalar value of stress, on the backbone ionomer fibers within a bundle is unlikely to be conserved over time. This is unlike the conserved external stress applied vertically to the ends of fibers in the prototypical FBM (Fig. 3.3 (a))¹. Likewise, the stress load is not conserved over bundles in the bundle-network of the PEM (as described in the caption of Fig. 3.2).

Regardless, for simplicity, based on an assumption of equal load sharing over backbone fibers and of no load dissipation within a bundle, the lifetime of a bundle was deduced in Ref. [58]. The rate of thermally activated breakage of a single ionomer fibre is given by [13]

$$\kappa_f(\sigma_f) = \tau_0^{-1} \exp(-\beta(E_a - \nu\sigma_f)), \quad (3.1)$$

¹In FBM, as the conserved external load is applied to the ends of fibers *in the same direction*, clearly the value of the von Mises stress of a fiber is exactly equal to the external stress load on that fiber. Of course, the total amount of the von Mises stress is equal to the external stress! But for fibers in the PEM, the swelling stress is applied to the wall of the bundle. In the bundle of PEM, the Cauchy stress tensor on each fiber is caused by equilibrium of forces between other fibers. The calculation of the Cauchy stress is much more complicated and the von Mises stress, as a scalar quantity, is calculated from this. Therefore, the sum of the von Mises stress loads of each fiber cannot be assumed as equal to the initial value of the total amount of the von Mises stresses. Similarly, for bundles in the PEM network, the stress load cannot be simply assumed to be conserved.

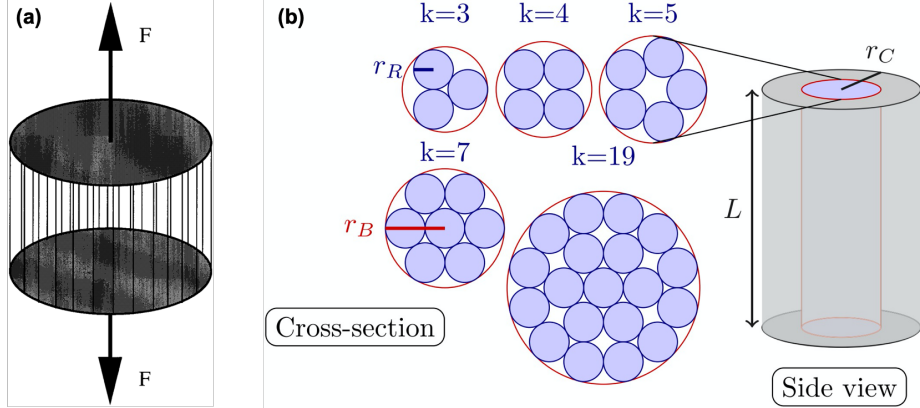


Figure 3.3: Illustrations of the comparison of the two models of bundle of fibers: (a) The *classical* fiber bundle model (FBM). The external stress is simply applied vertically at both ends of parallel fibers, the load is conserved over time. (b) A bundle of aggregated rod-like k ionomer fibers in an electrolyte: the bundle in the core with radius r_B , surrounded by a concentric electrolyte shell with radius r_C that contains dissociated protons bundles. Swelling pressure applies to the wall of the bundle, hence the scalar stress (load) field of the fibers inside the bundle during the fracture process is more complicated. (a) Reprinted figure with permission from Ref. [75] Copyright (1997) by the American Physical Society. (b) Reprinted figure with permission from Ref. [133]. Copyright (2014) by the American Physical Society.

where τ_0 is the period of an atomic bond vibration; $\beta = 1/(k_B T)$, with Boltzmann constant k_B ; E_a the activation energy of fiber breaking; ν the activation volume of an ionomer fiber and σ_f the stress on a single fiber. The breakage rate of a bundle was deduced as

$$\kappa_b(\sigma_f) = \tau_0^{-1} \exp(-\beta E_a) \left(\sum_{j=1}^k \frac{\exp\left(\frac{-k\beta\nu\sigma_f}{j}\right)}{j} \right)^{-1}. \quad (3.2)$$

3.2 Model

3.2.1 Bundle of Ionomer Fibers

Equation (3.1) adopted the exponential form as the decay rate to describe the thermally-dynamic failure process of a fiber. In the present work, we adopt this exponential breakage law for an entire bundle, resulting in

$$\kappa_b(\sigma) \propto \exp(\eta\sigma), \quad (3.3)$$

where σ is the stress on the bundle.

For theoretical purposes, we employ the exponential form for the breakage rate of a bundle in the bundle-network to explore the fracture propagation process, as distinct from

Table 3.1: Effective coefficients α_k/α_1 and η_k/η_1 for $k \leq 10$.

k	2	3	4	5	6	10
η_k/η_1	0.50	0.33	0.25	0.20	0.17	0.11
α_k/α_1	1	1	0.99	0.97	0.94	0.77

the power-law form of decay. There are detailed discussions in Section 2.1.3 to compare the decay rate of the power-law form (corresponding to the Weibull strength distribution) and of the exponential form (corresponding to the Gumbel strength distribution) for a material element in a fracture network. Substantial studies of fracture systems are based on the assumption of a power-law decay rate or the Weibull strength distribution of a material element to study the disordered regimes [82, 87, 124, 136, 137]. At the end of the present chapter, a comment in regards to the framework of the model will be presented.

We adopt the simplified exponential form Eq. 3.3 to describe the lifetime of a bundle. But for practical purposes, to get a qualitative understanding of the relation between the network lifetime and the bundle of size k , we hereby associate Eq. (3.3) to Eq. (3.2) in Ref. [58]. Fitting Eq. 3.3 to Eq. (3.2), Eq. (3.3) changes to

$$\kappa_b(\sigma) = \alpha_k \exp(\eta_k \sigma), \quad (3.4)$$

with $\sigma = k\sigma_f$. This form of the breakage rate is exactly equal to Eq. (3.2) for $k = 1$, where $\alpha_1 = \tau_0^{-1} \exp(-\beta E_a)$ and $\eta_1 = \beta \nu$. For $1 < k \leq 10$, Eq. (3.4) approximates Eq. (3.2) with effective coefficients that are listed in Table 3.1. The k values considered in Table 3.1 span the typical range encountered in Nafion-type PEMs [133, 58, 138]. For $k \gg 1$, Eq. (3.4) fails to reproduce Eq. 3.2 in the tail region of large σ . Coefficients in Eq. (3.4) have been optimized to reproduce Eq. (3.2) most closely in the range of $\eta_k \sigma$ from 0 to 30².

3.2.2 Bundle Network Model

Once the breakage rate of a bundle of size k is adopted, we can proceed to investigate the stochastic fracture failure process in the bundle-network. As illustrated in Fig. 3.1, we use an ordered lattice-like structure, to replace the randomly self-organized network. The results of Ref. [58] were obtained on a three-dimensional cubic model. In the present work, in order to keep computational costs reasonable, we have considered a bundle network with a two-dimensional square lattice structure, as we were primarily interested in obtaining a qualitative understanding of the impact of correlation effects on fracture formation in this

²The upper limit of the evaluated range of $\eta_k \sigma$ is approximately determined by the highest stress on a single bundle when 50% bundles have failed for the system of $\eta \sigma^0 = 0.46$ and $\gamma = 100$.

bundle network. The regular lattice of bundles is prepared in an initial state, in which all bundles have equal k and thus equal mechanical strength. Moreover, a uniform initial stress field σ^0 is assumed, meaning that each bundle in the pristine lattice is intact and under identical stress.

Now it comes to the question of the stress field redistribution regime. Upon breakage of a bundle, the load that it carried prior to breaking will be redistributed to surviving bundles in the network. As discussed previously in Section 3.1, bundles in the membrane that are subject to a swelling pressure take complicated stress loads. For simplicity, we will assume that the total stress in the network is conserved at each breakage event. As reviewed in Section 2.1.2, the power-law-type stress redistribution rule (Eq. (2.1)), introduced by Hidalgo *et al.* [82], was originally used to apply to an FBM. That can be regarded as an intermediate stress transfer rule between equal load sharing (ELS) and local load sharing (LLS). We now adopt it in the present work for the bundle-network model. To express it more explicitly, the stress transfer function is,

$$F(r_{ij}, \gamma) = r_{ij}^{-\gamma} \left(\sum_{j \in I} r_{ij}^{-\gamma} \right)^{-1}, \quad (3.5)$$

where r_{ij} is the distance between the midpoints³ of the failed bundle i and an intact bundle j in the lattice (see Fig. 3.4), γ is a correlation exponent related to the load distribution range, and I denotes the set of intact bundles. If only one bundle breakage event takes place at a time, the amount of load received by a surviving bundle j after time step τ , is,

$$\sigma_j(t + \tau) = \sigma_j(t + \tau - 1) + \sigma_i(t + \tau - 1)F(r_{ij}, \gamma), \quad (3.6)$$

As remarked in Section 2.1.2., the limit $\gamma \rightarrow \infty$ corresponds to the case when the load of the failed bundle is transferred to nearest neighbours, referred to as the LLS scheme. This regime is attained to very good approximation when $\gamma > 10$ ⁴. The opposite limit, $\gamma \rightarrow 0$, corresponds to the ELS, wherein all intact bundles receive exactly the same fraction of the load released by the breakage of a bundle. The ELS scheme or the limit $\sigma^0 \rightarrow 0$, represents the case of the uncorrelated percolation. In the work of 2015 [58], the lifetime is overestimated due to the neglect of the load redistribution in that approach, as accounted for in the second term on the right-hand side of Eq. (3.6).

³The LLS or the localization regime is sensitive to the way it defines the distance between bonds in the lattice.

⁴For $\gamma > 10$, nearest neighbours share 96.8% of the load released by a broken bundle. In our study, the highest γ is set to be 100, for which 99.99997 % are shared among nearest neighbours.

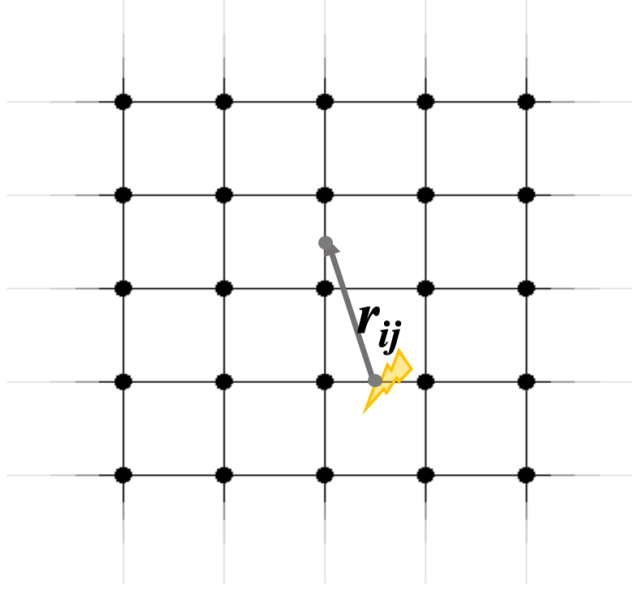


Figure 3.4: An illustration of how the stress of failing bundles is transferred in the bundle-network. When a bundle i fails, the entire stress load is transferred to other intact bundles. The fraction of the stress load bundle j receives is evaluated by the distance r_{ij} between the midpoints of the bundles and Eq. (3.5).

3.2.3 Remarks

It is important to note that the basic model variant considered in this present work assumes that the total stress is conserved. This assumption is usually valid for materials under controlled external load. However, in the case of a PEM explored here, stress on bundles is generated internally by water uptake and swelling, and it will usually not be conserved. In future studies using this model, a stress dissipation rule should be introduced to account for the change in total load during crack growth.

Therefore, the current model of the PEM in this work is within the same framework as the FBM due to its stress load conservation⁵. The physical phenomena revealed by the numerical results shown in Chapters 5 and 6 can be compared to the conclusions from other FBM fracture models [19, 82, 87].

In the past, substantial theoretical or numerical studies were based on the assumption of the power-law breakdown rule (or the Weibull strength distribution) [82, 87, 124, 136, 137]. As reviewed in Section 2.1.3, the exponential breakdown rule (based on the Gumbel strength distribution) better describes the natural failure processes of the fibrous systems or even of some random fuse networks (RFMs). Regardless, to the best of our knowledge, due to high

⁵Unlike an FBM with the fibers as the basic material elements, the basic elements in a this bundle-network of PEMs are bundles. But they have the same spirit, as the bond percolation problem in bundle-network of PEM can be transformed into a site percolation problem.

computational costs, few numerical works based on the exponential breakdown rule have been conducted. Our present model of the PEM as a deviation form of FBM can thus be compared with other FBMs based on the Weibull strength distribution. One difference to be noted is that the strength of correlations depends on both parameters γ and σ^0 (initial stress). In studies by Hidalgo *et al.* in Ref. [82], and by Shekhawat *et al.* in Ref. [124], breakages in the network were assumed to follow a power-law breakdown rule or a Weibull strength distribution, in which the failure processes or fracture regimes are independent of the uniformly distributed initial stress.⁶

⁶In our case, as the breakage rate of bundles follows an exponential law, the probability of a bundle failure at each kinetic MC step is proportional to its rate. In the power-law case, the ratio of breakage possibilities between a bundle with $n\sigma^0$ and another bundle with σ^0 does not change, i.e., $\frac{d}{d\sigma^0} \frac{n\sigma^{0\rho}}{\sigma^{0\rho}} = 0$. In our case, bundles with larger stress are more strongly correlated in systems with larger initial stress, and thus $\frac{d}{d\sigma^0} \frac{\exp(n\eta_k\sigma^0)}{\exp(\eta_k\sigma^0)} > 0$ for $n > 1$. Please refer to Chapter 4 for the simulated algorithms of the fracture process to achieve a deeper understanding.

Chapter 4

Computational Approach and Methods

The highly simplified bundle model of polymer electrolyte membranes (PEMs), discussed in Chapter 3, considers the fracture process of a PEM as a sequence of bundle failure events on a random network. In principle, this sequence is a Markov chain and it can be simulated using a well-established kinetic Monte Carlo (kMC) method [139, 140, 141, 142]. During the kMC simulation process, the onset of percolation needs to be determined so that the percolation thresholds p_c^L and the lifetime t_{PEM} can be obtained. This can be realized by employing an efficient tree-based algorithm.

Section 4.1 reviews the theoretical basis of the rejection-free kMC methods. Thereafter, this algorithm will be adapted to our PEM model.

Section 4.2 introduces a tree-based algorithm proposed by Newman *et al.* [102, 102] as an efficient way of keeping track of the formation and growth of clusters of broken bonds on the lattice of bundles.

Section 4.3 presents the detailed simulation procedure of the dynamic fracture process of PEMs that employs the kMC method as well as the percolation detection algorithm.

In Section 4.4, a comment on the limitations of this employed algorithm is detailed.

4.1 Kinetic Monte Carlo Algorithms

4.1.1 Markov Chain Monte Carlo

Monte Carlo (MC) methods are a broad class of computational algorithms that rely on the process of random sampling to carry out the repeated (computational) experiments/simulations to obtain numerical results. MC methods have been widely adopted to solve mathematical and physical problems. A simple example is the estimation of the number π , i.e., the ratio of the circumference to the diameter of a circle, by generating enough (uniformly distributed) random points within a square which itself is enclosed with a circle and counting the number of points inside this embedded circle relative to the total number of points. In

the process of MC simulations, random sampling requires a reliable way of generating a random number using a computer. This can be realized by a pseudorandom number generator [143].

In statistical physics, a dynamic process of a system can be described by a sequence of random states. If the probability of the next state is only dependent on its current state, regardless of its history, this process is a Markovian process [144, 145]. Accordingly, you will see in Section 4.1.3 the fracture dynamic process in our present model of PEM network is a Markov chain.

For a Markov process, the time evolution of a system can be depicted by an ensemble of all the possible sequences or trajectories of the states. This ensemble is described by a Markovian master equation,

$$\frac{\partial}{\partial t} \rho_v(t) = \sum_u (w_{vu} \rho_u(t) - w_{uv} \rho_v(t)), \quad (4.1)$$

where $\rho_v(t)$ is the probability for the system to be in state v at time t , and w_{vu} is the transition rate for the system to change from state u to state v .

We attempt to solve or calculate the master equation. However it is unlikely to acquire the complete probability transition matrix \mathbf{w} for the entire ensemble [142]. Therefore, we carry out MC methods to simulate one possible trajectory at a time. With infinite random samples, every possible trajectory should be generated (with the correct distribution).

Under the current state of the system, there are a number of candidate states that can be transited to. For a "standard" rejection Monte Carlo algorithm, whether the transition to this selected candidate state should be "accepted" or "rejected" follows a certain probability ¹. The Metropolis-Hastings algorithm [146, 147] is a rejection MC method that is widely adopted to simulate the Ising model or a static percolation model (see Section 2.2.2). Apparently, it is less efficient due to the repeated rejections of the occurrence of transitions before a real transition to one of the candidate states takes place.

4.1.2 Rejection-free Kinetic Monte Carlo

In the case of the rejection-free Monte Carlo method, it is more efficient as there must be the occurrence of one state transition (or one event in the language of statistics) at any given time step τ ². Thus, the probability that state v is selected to transit from the current

¹For a system or a microscopic material element that has multiple states, one of the states must first be randomly selected and then whether this state can be transited to follow a certain probability, whereas for binary states, it is just repeated rejection or acceptance of the other state (e.g., a spin in an Ising model).

²A real dynamic system should follow a continuous time scales, whereas the kinetic MC method is a discrete-time Markov chain. A reader can refer to Ref. [148] for a discussion of whether the kinetic rejection or rejection-free MC methods accurately describe the physical time scales.

state u is,

$$p_v = \frac{w_{vu}}{\sum_m w_{mu}}. \quad (4.2)$$

Based on Eq. (4.2), we replace p_u with a random number $\rho^{(1)}$, that is selected from a uniform distribution $[0,1]$ by a random number generator. Then state v is selected if the following conditions are met,

$$\begin{aligned} \sum_{m=1}^{v-1} p_m &\leq \rho^{(1)} < \sum_{m=1}^v p_m, & v > 1, \\ 0 &\leq \rho^{(1)} < p_1, & v = 1, \end{aligned} \quad (4.3)$$

During the selection process, the (efficient) recursive binary search algorithm [149] should be adopted.

The time interval τ in the kinetic rejection-free MC can be calculated by following the Poisson distribution, $P_{n_e} = \frac{(\lambda\Delta t)^{n_e}}{n_e!} e^{-\lambda\Delta t}$, where $\lambda = \sum_m w_{mu}$ and n_e represents the number of (transition) events that occur during the time duration Δt . n_e equates to 0, as no transition events should happen during the waiting time τ . The Poisson distribution then becomes

$$P_0(\Delta t = \tau) = e^{-\lambda\tau}. \quad (4.4)$$

We replace P_0 with $\rho^{(2)}$, another random number sampled from a uniform distribution $[0, 1)$. We get

$$\tau = -\frac{\ln(\rho^{(2)})}{\lambda}, \quad (4.5)$$

which can describe the possible waiting time τ before the next transition event.

In a kinetic rejection-free MC simulation, a complete MC realization or run, i.e., a copy in the statistical ensemble of a configuration, involves repeated MC steps of Eqs. (4.3) and (4.5) until a whole process is terminated ³. A specific MC run of a configuration reflects one of the possible trajectories of states or a copy of the statistical ensemble. To approach an ensemble of all trajectories of a real physical system, we need to have sufficient MC sampling size, i.e., conduct many independent MC runs.

4.1.3 Adopting the Rejection-free MC Method for the PEM Fracture Model

In our present model as presented in Chapter 3, the failure process of a PEM can be described as a sequence of bundle failure events. During the fracture propagation, the stress field redistributes over time. In this regard, we can express a state \mathbf{S} (at a specific time) of the

³A termination of a MC simulation is determined by the thresholds required for the problem at hand. For example, a MC run in our simulation can be assumed to be terminated when the percolation threshold is reached or when all bundles fail.

system as a configuration that includes the present network structure $\mathbf{s} = (s_1, \dots, s_i, \dots, s_N)$ where $s_i = -1$ or 1 (1 represents being intact), the updated stress field $\boldsymbol{\sigma}$ and the ongoing failing bundle index f_b , viz, $\mathbf{S}(\mathbf{s}, \boldsymbol{\sigma}, f_i)$. The present state u is,

$$u = \mathbf{S}(\mathbf{s} = \mathbf{s}^{(m)}, \boldsymbol{\sigma} = \boldsymbol{\sigma}^{(p)}, f_b = i). \quad (4.6)$$

The next candidate state v is,

$$v = \mathbf{S}(\mathbf{s} = \mathbf{s}^{(n)}, \boldsymbol{\sigma} = \boldsymbol{\sigma}^{(q)}, f_b = j). \quad (4.7)$$

where $\mathbf{s}^{(n)} = \mathbf{s}^{(m)} - (0, \dots, s_i = 1, \dots, 0)$ and $\boldsymbol{\sigma}^{(q)} = \boldsymbol{\sigma}^{(p)} + \boldsymbol{\sigma}_{add}$ which follows the rule of stress transfer from the ongoing failing bundle as depicted in Eq. (3.5) and Eq. (3.6).

According to the above expressions, we can see the probability of the next failure event of any surviving bundle solely depends on its current state. In other words, the dynamic process is Markovian. We thus apply the above Rejection-free MC method to this Markov process. The transition rate w_{vu} from the present state u to the candidate state v equates to the breakage rate κ_j of the candidate bundle j , thus Eq. (4.2) changes to

$$p_v = p_j = \frac{\kappa(\sigma_j)}{\sum_{k \in I} \kappa(\sigma_k)}, \quad (4.8)$$

where I denotes the set of intact bundles, σ_j represents the accumulated load on bundle j (or the j th component of $\boldsymbol{\sigma}^{(p)}$) and the decay rate $\kappa(\sigma)$ has an exponential form as described in Eq. (3.4).

Likewise, Eq. (4.5) changes to

$$\tau = -\frac{\ln(\rho^{(2)})}{\sum_{k \in I} \kappa(\sigma_k)}. \quad (4.9)$$

4.2 Percolation Algorithm

As described in Chapter 3, we map the fracture dynamics on the bundle-network of a PEM to a kinetic bond percolation model. This dynamic process can be simulated by a kinetic rejection-free MC method as described in Section 4.1.3. In an MC run, a bond on the lattice (which represents a bundle failure) appears one by one and connect together to form clusters, until one of the clusters percolate opposite boundaries of the lattice in any of the principal directions. Thus, we intend to adopt an algorithm to identify the clusters and observe the onset of percolation.

The conventional algorithms are less efficient due to the repeated cluster relabelling process of every bond (or site) belonging to the sub-cluster(s) when the merging of clusters

happens. In this regard, a depth-first or breadth-first search should be adopted [150] to trace back or scan the bonds belonging to the subclusters at each MC step.

Newman *et al.* in Refs. [102, 151] proposed an efficient tree-based algorithm for the purpose of determining the percolating cluster(s) (in the kinetic percolation model⁴). The main idea is to construct a tree structure to represent all bonds in the same cluster. In a "tree", a "pointer" is used to direct a "child" bond to its "parent" bond, and finally the successive pointers can lead to the "grand-parent" or the (only) root of the tree. As illustrated in Fig. 4.1, bond A_1 at first as an isolated bond is a cluster itself, so it points to itself. Later A_2 connects to it so that the pointer of A_2 directs towards A_1 ; A_3 as a new bond connects to A_2 so that sequentially leads to A_1 as the root of the cluster A . Likewise, going through the similar process, B_1 becomes the root of cluster B . Now consider that a new bond C_1 is added and connects both the cluster A and the cluster B . C_1 first connects to the adjacent bond B_2 , so it directly points to the root B_1 ; then as it also connects a (larger) cluster A though A_3 which directs toward A_1 , so B_1 as the root of sub-cluster B just updates its pointer to A_1 instead of pointing to itself. In this way, the other bonds in sub-cluster B do not require being relabeled, as all their pointers will finally lead to A_1 as the root of the new merging cluster. Finally, to detect whether a percolating cluster occurs at each MC step, we just have to check whether the occupied bonds on opposite boundary of the lattice share the same root.

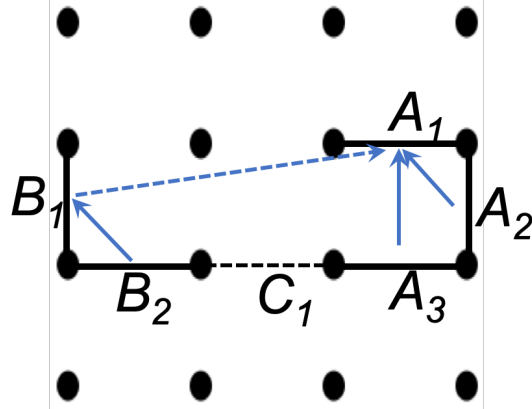


Figure 4.1: An illustration of two tree-structures which represents the clusters A and B and the merging process of the two clusters. The bonds A_1 and B_1 are the roots of the (sub-)clusters A and B respectively and the arrows represent pointers. Bond C_1 connects both the sub-clusters A and B , and by adding an updated pointer from the root B_1 of the cluster B to the other root A_1 , it completes the merging of the sub-tree (of B) into the bigger tree (of A).

⁴This algorithm can also apply to the "standard" static percolation as described in Section 2.2.1. Once the entire lattice structure is generated by the occupation probability p , a convenient random order of the "fake" kinetic occupation of the sites or bonds can be created accordingly.

4.3 Algorithm

By combining the kMC method (Section 4.1.3) and the percolation detection algorithm (Section 4.2), we can simulate the dynamic fracture process of our present model. The whole program is written in Python. Regarding to the matrix (or array) construction and calculation, the library NumPy is adopted to operate efficient array calculations. In this work, we construct finite $L \times L$ square lattices ($L = 50 - 400$). The number of bonds in the lattice is $N = 2L^2 - 2L$. In the program, we perform n MC runs (or realizations) for each configuration of L , $\eta_k\sigma^0$ (uniform initial stress), and γ (which defines the effective range of interaction in Eq. (3.5)). Each MC realization describe a possible dynamic directory in the statistical ensemble.

The percolation thresholds p_c^L obtained for these n runs (or realizations) exhibit a frequency distribution. Fig. 4.2 shows examples of the frequency distributions of p_c^L for $L = 50$ and 250 respectively in the uncorrelated percolation systems. For a finite lattice size, the width of this distribution is finite. In the limit of an infinite lattice size, a δ -function-like distribution is approached. From this frequency distribution, an expectation value of the percolation threshold can be determined. In most cases of lattices with $L = 100$, $n = 5000 - 10000$ runs were performed, whereas for $L > 150$, we only performed 50-200 runs in most of cases ($n \geq 2000$ runs only for a few cases). We employ the ranges of $\eta_k\sigma_0 = 0 - 3$ and $\gamma = 0 - 100$ to scan the dynamic range from weakly correlated random breakage to highly locally correlated crack growth.

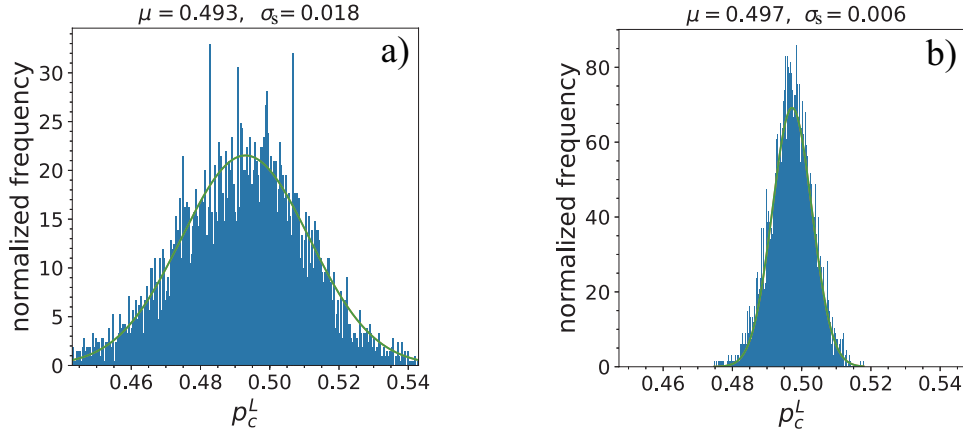


Figure 4.2: Frequency distributions of p_c^L in the uncorrelated case ($\eta_k\sigma^0 = 0.45$ and $\gamma = 0$), fitted with Gaussian functions (a) for $L = 50$ with the mean $\sigma_s = 0.493$, the standard derivation $\sigma_s = 0.018$ and $n = 5000$; and (b) for $L = 250$, $\sigma_s = 0.497$, $\sigma_s = 0.006$ and $n = 25000$.

A flowchart of this algorithm process is shown in Fig. 4.3.

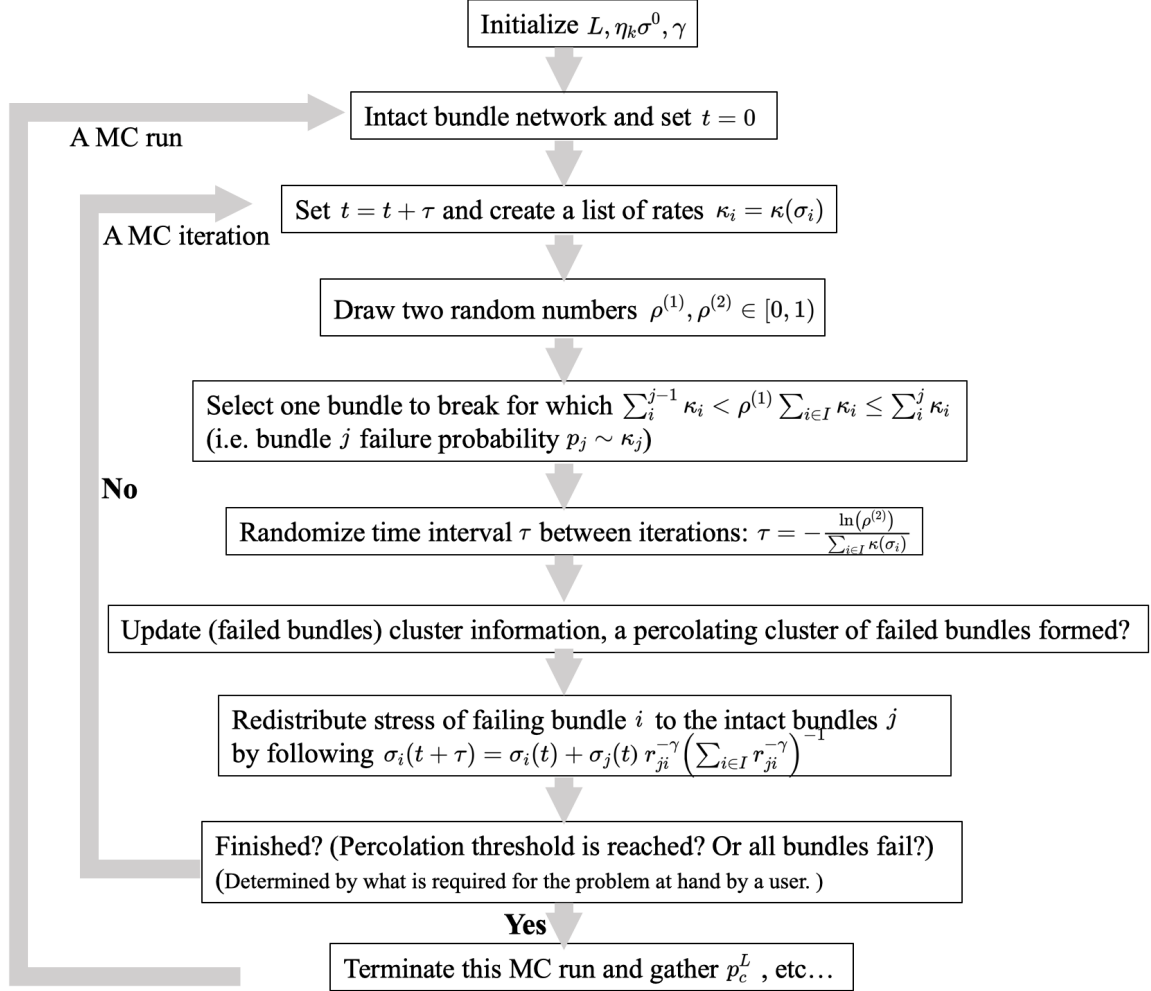


Figure 4.3: A flowchart of Monte Carlo simulations of a particular configuration of $L, \eta_k\sigma^0$ and γ . For each configuration, a distribution of p_c^L is acquired by performing n MC runs. For a single MC run, many MC iterations are repeated until a termination point is reached. A termination point is reached when a percolating cluster appears at first time or when all bundles fail, which is determined by the thresholds required for the problem at hand by a user.

The more detailed algorithm process is presented as follows:

Processes

(1) Initialization:

- (a) Square lattice initialization:
 - (i) Define L . Construct an N -element 1D-array (vector) where the i^{th} element represents the bond i in the $L \times L$ square lattice (see Fig. 4.4).
 - (ii) Construct an $N \times 6$ 2D-array (matrix) of the nearest neighbours (or the adjacent bonds)⁵ of any bond i in the square lattice.
 - (iii) Construct an $N \times N$ 2D-array of the distances r_{ij} between any two bonds i and j in the lattice.
- (b) Define $\eta_k \sigma^0$. Construct an N -element 1D-array of the stress field σ_i .
- (c) Define γ . Calculate an $N \times N$ 2D-array of F_{ij} which describes the fraction of stress transferred from bond i to bond j , according to r_{ij} and Eq. (3.5).

(2) Performing n MC runs:

Repeatedly perform the following processes for n MC runs (times):

- (a) Reset to the initial state of the lattice as described in (1) Initialization.
- (b) Repeat the following procedure for each subsequent MC step until an MC run is complete⁶ :
 - (i) Calculate a N -element 1D-array of failure rates of bundles, where i -th element represents the failure rate κ_i of bond i and it can be calculated according to σ_i and following Eq. (3.4).
 - (ii) Calculate the time interval τ according to Eq. 4.5 and update the present time t to $t + \tau$.
 - (iii) Select a bond to occupy⁷, i.e., a bundle failure event, according to κ_i . And the selection process follows Eq. (4.8) and Eq. (4.3).
 - (iv) Construct or update clusters of open bonds by Newman's tree-based algorithm [102, 151] as described in Section 4.2.

⁵Adjacent bonds of bond i means the bonds (or edges) that are connected or shared with bond i by the same site (or vertex). So in a square lattice, each bond has 6 adjacent bonds. In the vicinity of the finite-sized lattice boundaries though, the number of adjacent bonds of a bond can be less than 6.

⁶In this model, the PEM is assumed to reach a global failure when a percolation threshold is reached. However, for the purpose of studying the fracture regime after the onset of percolation, the simulation continues until all bundles fail *completely*. In this way, the growth dynamics of the largest crack can be analyzed in Chapter 5. See Fig. 5.9 , Fig. 5.10 and Fig. 6.5.

⁷On the other hand, open bonds represent intact bundles.

- (v) Transfer the stress load from failing bundle i to any surviving bundle j , according to $F_{ij} / \sum_{k \in I} F_{ij}$ and update the new stress field σ_i .
- (vi) Check whether the onset of percolation appears through Newman's algorithm. If yes, record the percolation threshold p_c^L and the lifetime t_{TEM} for this copy of the statistical ensemble.⁸

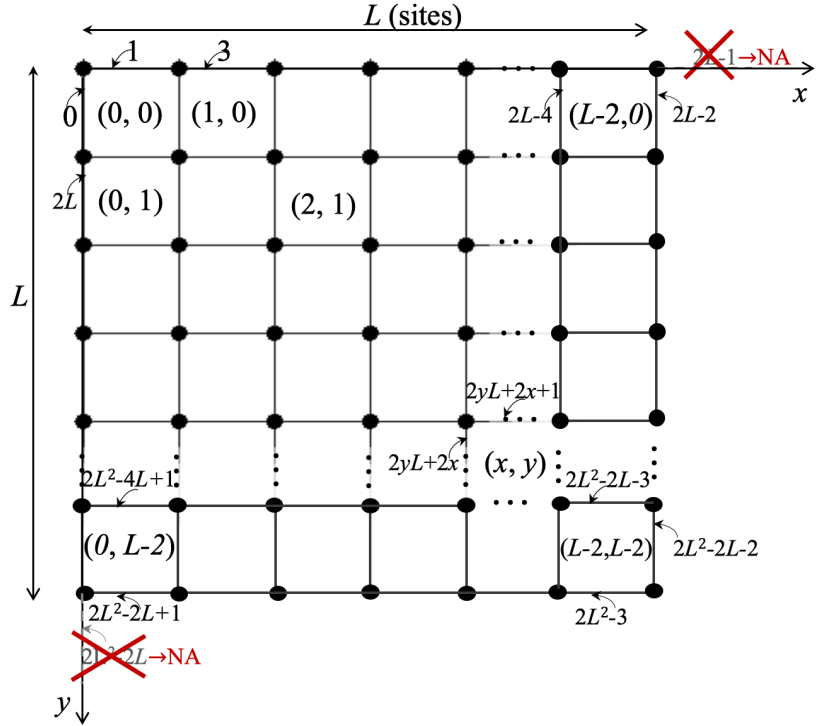


Figure 4.4: An illustration of an $L \times L$ square lattice. The coordinates of a cell are represented as (x, y) , and the indices of two bonds in a cell (x, y) are $2yL + 2x$ and $2yL + 2x + 1$, respectively. The distance between two bonds can be calculated accordingly. If a bond is outside of the boundaries of the lattice, its index is set as "NA". The total number of bonds is $N = 2L^2 - 2L$.

4.4 Remarks on the Algorithm

We here remark on a questionable aspect of this algorithm, that is related to the form of decay rate of $\kappa(\sigma)$ considered in this model. $\kappa(\sigma)$ is assumed as a *classical* and *continuous* form as described in Eq. 3.4 (or Eq. 3.2).

In the limit of small stress, as defined in E_a in Eq. 3.1, a thermally activated process involves an activation energy, so the energy barrier must be overcome to cause a bundle failure. The algorithm contradicts the logic above, as we get a failure probability $p_j > 0$ at

⁸We could also store the information of cluster sizes for cluster size studies.

each MC step with any finite σ borne by a bundle. Moreover, all bundles in the network will eventually fail over time in this regard, whereas in an algorithm of the static type (as reviewed in Section 2.1.3), below a critical stress load σ_c , the system will finally reach a stable state with remaining bundles remain intact [82].

In the limit of large stress, the fracture dynamics behaviour exhibited by the model can be nonphysical as well. With the assumption of stress conservation, the breakage process will accelerate even for the uncorrelated percolation regime. We can consider an extreme case that all stress loads accumulate on the last single bundle for a lattice of $L = 100$ for an initial load $\eta_k \sigma^0 = 0.5$, the breakage time τ in Eq. (4.5) can reach to unphysical timescale of 10^{-10^5} ! (Planck time is 5×10^{-44} .) Despite this, the breakage probability of each bundle at each MC step is still assumed to follow Eq. (4.8) in this algorithm ⁹.

The above questions are being raised is because they are relevant to whether the fracture dynamic behaviour being simulated (for example, the order of bundle breakages) is physical at the lower and the higher limits of the stress load.

⁹The storage of the high rate of large load, exceeds the storage of Float64 of NumPy array. When the load $\eta_k \sigma^0$ of any bundle exceeds the value of 4×10^2 , I assign the interval before the next MC step $\tau = 0$.

Chapter 5

Results: Fracture Regimes and Percolation Behaviour at a Fixed Lattice Size

5.1 Overview

has discussed a crossover between two limiting fracture regimes. In a fracture regime of infinite disorder, the bundles break completely at random [71] in the bundle-network, and this random breakage regime is usually referred to as the percolation-type regime. Another fracture regime shows more ordered breakage behaviours: with strong spatial correlation between breakage events, micro-cracks form alongside only one or a few crack tips or nuclei.

The correlations between breakage events are caused by the redistribution of the stress field over time, which results in a non-uniform stress field. We employ a power-law rule ($r^{-\gamma}$) for the stress transfer from the failing bundle to intact bundles to describe the field reconstruction after each failure event. In this stress transfer law, γ presents the effective range of stress transfer and it allows tuning between two limiting schemes of load sharing: the local load sharing scheme (LLS) for $\gamma \rightarrow \infty$ and the equal load sharing scheme (ELS) for $\gamma \rightarrow 0$ (or the global load sharing scheme (GLS) at low γ). ELS corresponds to a mean-field approximation (which Landau theory is based on) and LLS only considers the local interactions. With an assumption of exponential breakage rates of the bundles, the uniform initial stress field σ^0 is another quantity that characterizes the correlation strength between breakage events. Thereby, we wish to relate γ and σ^0 to the two fracture regimes.

The probability distribution¹ of the percolation thresholds p_{av}^L for uncorrelated percolation of finite lattices is Gaussian-like as reviewed in Section 2.2. The fracture regimes affect the geometric structure of the intact bundle-network over time. We ask two questions: (1) Do the distributions of percolation thresholds still resemble single-peaked Gaussian? (2)

¹or *frequency* distribution for numerical calculations

Does the strength of correlation *always* reduce the (overall) percolation threshold, as it is intuitively believed that correlation strength increases the connectedness of clusters?

This chapter presents a complete analysis of the impacts of σ^0 (normalized to η_k) and γ at a fixed lattice size $L = 100$. For each combination of values of σ^0 and γ , we have performed thousands of Monte Carlo (MC) realizations. Most of the results presented in the current chapter have been published in Ref. [152]. One should note that the global breakdown of PEMs in this model is defined as the point at which the system is percolated, since this is when the reactive air may permeate into the sample-spanning crack. All the physical quantities (except for the largest crack growth dynamics) are observed at a percolation threshold. The structure of the results in this chapter is presented as follows.

Section 5.2 contains the most important findings of this work. We investigate the crossover between two fracture regimes, viz., the random breakage (percolation-type) regime and the correlated crack growth (localization) regime. The frequency distributions of percolation thresholds are shown for these two regimes and their crossover. We then introduce a new order parameter based on the distribution of percolation thresholds. This order parameter is employed to assess the degree of disorder (or the degree of correlation) and to separate the two regimes as a relation of σ^0 and γ .

Section 5.3 presents the variations of the percolation thresholds, that include the mean values μ_1 , μ_2 of the two Gaussians fitted on the distribution and the average percolation threshold p_{av}^L .

Section 5.4 analyzes the growth of the largest crack evolving from the initial intact lattice to the complete breakdown of all bundles² on the lattice. The static cluster structures at a percolation threshold, including the moments of the cluster size distribution, are also analyzed.

In Section 5.5, we present the lifetime of PEMs as a practically important outcome.

In Chapter 6, an analysis of varying lattice sizes will be presented generalizing the above analysis at a fixed lattice size to varying sizes to assess to what extent the above observations are simply size effects.

5.2 Percolation Regimes and Order Parameter

5.2.1 Distribution of Percolation Thresholds for Different Regimes

As reviewed in Section 5.1, the system approaches the limit of uncorrelated percolation, when $\sigma^0 \rightarrow 0$ or $\gamma \rightarrow 0$. At this limit, the distribution of percolation thresholds p_c^L resembles a Gaussian. At high σ^0 and γ , the system reaches the limit of strong (local) correlation –

²Even though in this model the system failure of the PEM network is assumed to be reached at the onset of percolation, we continue the simulations of the bundles breakage events after this critical point. In this way, we can analyze a complete crack growth process from the beginning to the end.

a fracture regime that exhibits localized damage. Now it comes to the question of the distribution of p_c^L when the system sits between the limits of the two fracture regimes.

For parameter values appropriate to the weak correlation regime ($\eta_k\sigma^0 = 0.20$, $\gamma = 100$, and $n = 5650$) as illustrated in the damage snapshot of Fig. 5.1 (b), the percolation thresholds show a frequency distribution that exhibits a single peak and resembles a Gaussian distribution (Fig. 5.1 (a)). We verified in further simulations that the width of the distribution decreases with increasing L , approaching a δ function-like distribution in the limit of $L \rightarrow \infty$, as expected (see Fig. 4.2).

A strongly correlated system, as realized for high σ^0 or high γ exhibits correlated crack growth behaviour at early stage (Fig. 5.1 (d)). The frequency distribution of p_c^L for this case is illustrated in Fig. 5.1 (c), obtained with $\eta_k\sigma^0 = 2.0$, $\gamma = 100$, and $n = 6430$. The distribution exhibits a Gaussian-like shape as well, but with larger width.

Interestingly, we can identify an intermediate or crossover regime, in which the frequency distribution of percolation thresholds exhibits two peaks, as depicted in Fig. 5.2 (a) for the case $\eta_k\sigma^0 = 0.46$, $\gamma = 10$, and $n = 5000$.

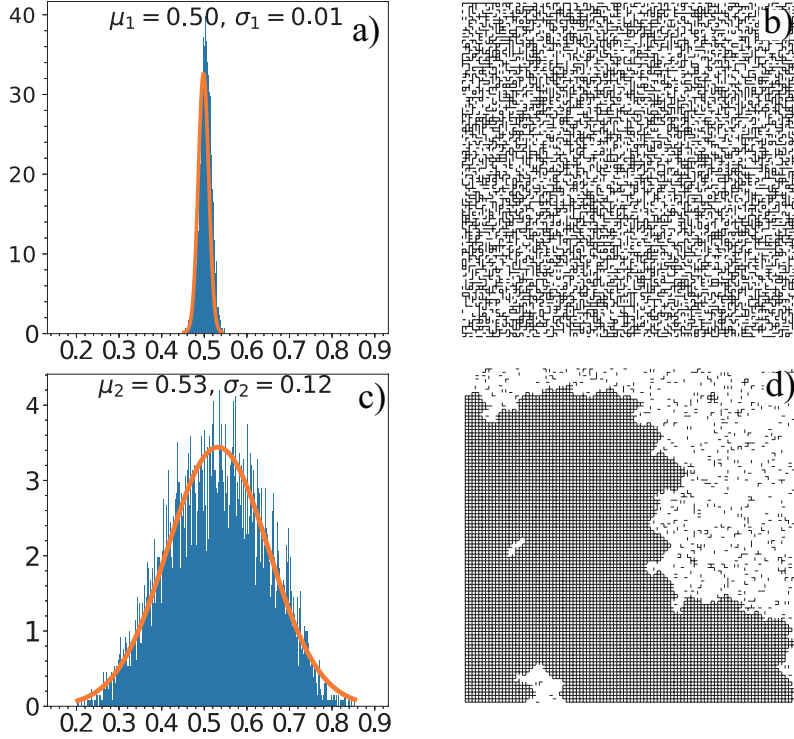


Figure 5.1: Normalized frequency distributions of percolation thresholds for a square lattice with $L = 100$, for (a) random breakage regime ($\eta_k\sigma^0 = 0.20$, $\gamma = 100$ and $n = 5650$, single Gaussian), (c) localization regime ($\eta_k\sigma^0 = 2.0$, $\gamma = 100$ and $n = 6340$, single Gaussian). The plots in (b) and (d) show snapshots of lattice configurations corresponding to (a) and (c). Orange curves represent the Gaussian functions fitted to these distributions.

In this case, both damage regimes, namely random breakage (left peak) and localization (right peak), occurring at different MC copies. The dominant mechanism of cluster growth for a specific MC realization depends on whether a correlated crack growth is triggered at a time point prior to reaching the percolation threshold by uncorrelated cluster growth. In Fig. 5.2 (b), (i) and (ii) show snapshots of two different MC realizations of the system, which correspond to random breakage regime and localization regime respectively.

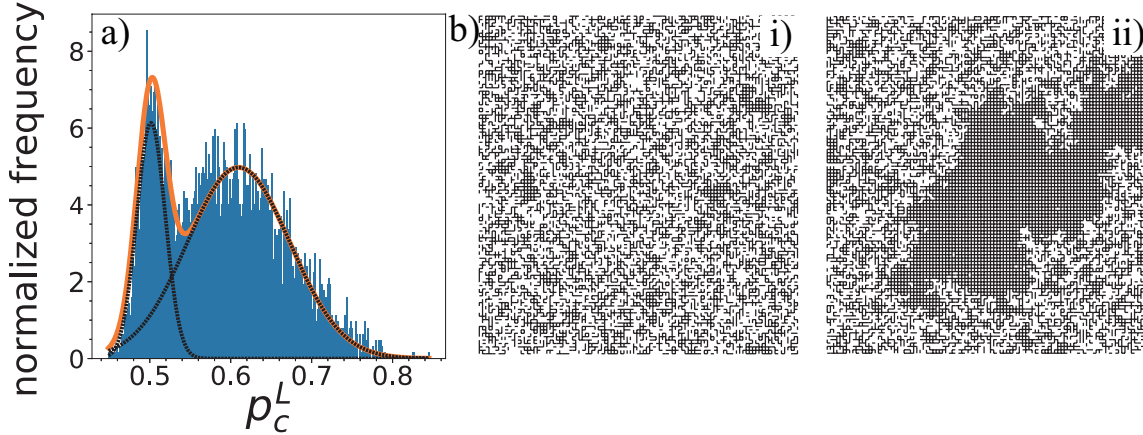


Figure 5.2: Normalized frequency distribution of percolation thresholds (a) and the damage snapshots (b) for the crossover region ($\eta_k \sigma^0 = 0.46$, $\gamma = 10$ and $n = 5000$). Two clearly distinguishable peaks for random breakage (the left peak) and localization (the right peak) are visible and both mechanisms coexist (statistically) on different MC copies as illustrated as shown (i) and (ii) in (b). The black curves represent the two Gaussian functions fitted onto each respective peak. The orange curve represents the sum of the two Gaussian functions.

5.2.2 Order Parameter

As reviewed in Section 5.1, whether the dominant damage regime is the random breakage or the localization regime, affects the geometric structure of the lattice, thus subsequently influencing the distribution of percolation thresholds. In this spirit, based on the percolation behaviours, we tentatively introduce a quantitative means to assess the importance of correlation effects for a given set of $\eta_k \sigma^0$ and γ .

With the two-peaked shape of the frequency distribution function as shown in Fig. 5.2 (a), we can determine two expectation values of the percolation threshold. We reproduce the frequency distributions of percolation thresholds with two Gaussian functions to determine their mean values μ_1 , μ_2 , standard deviations σ_1 , σ_2 , and areas A_1 , A_2 under the distinct peaks. We define an order parameter ξ

$$\xi = A_2/(A_1 + A_2). \quad (5.1)$$

to describe the crossover between the two disordered regimes, where $\xi \simeq 0$ in the limit of the random breakage regime and $\xi \simeq 1$ in the limit of the localization regime. Moreover, ξ can be employed as a quantitative measure of the strength of correlations.

5.2.3 Phase Diagram

With this introduced order parameter ξ as a measure to assess the crossover between the two fracture disordered regimes, we analyze how ξ depends on both $\eta_k\sigma^0$ and γ in Fig. 5.3.

Fig. 5.3³ (a) shows ξ as a function of $\eta_k\sigma^0$ for several different values of γ , whereas Fig. 5.3 (b) shows ξ as a function of γ for several different values of $\eta_k\sigma^0$. For $\eta_k\sigma^0 \leq 0.30$, only the first peak ($\xi \simeq 0$) occurs over the whole range of γ values explored. In this regime of weak stress, the correlated crack growth damage mechanism does not occur. The crossover region can be observed for stress $0.41 \leq \eta_k\sigma^0 \leq 0.46$ over high γ , in which two clearly distinguishable peaks are seen in the frequency distribution plots. Only for stress $\sigma^0 \geq 0.51$, the system can enter the localization regime. As can be seen, the crossover from random breakage to localization behaviour is relatively sharp.

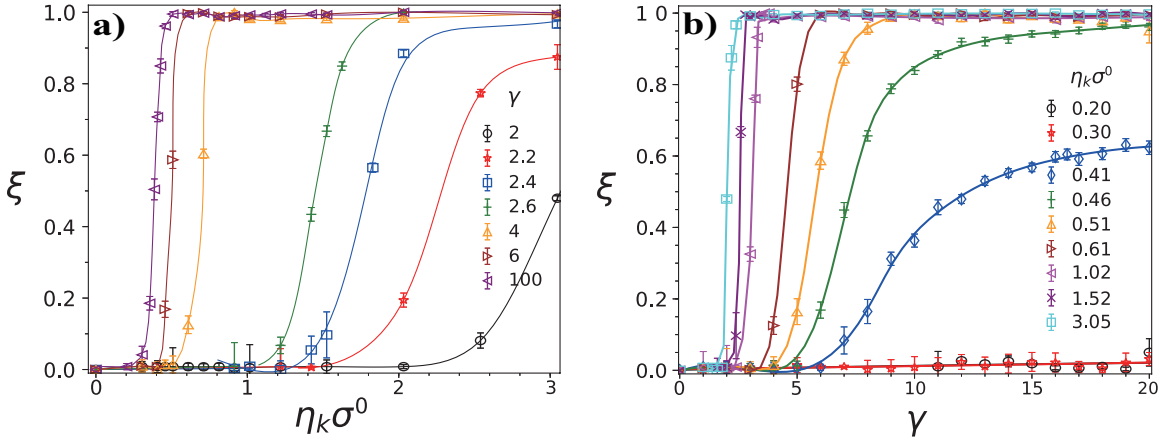


Figure 5.3: Plots of the order parameter $\xi = A_2/(A_1 + A_2)$ over (a) the initial stress of each bundle σ^0 (scaled by η_k) with γ as parameter, and (b) γ with σ^0 as parameter. Interpolated lines are shown to guide the eye. The method used to determine errors of ξ is described in footnote 3 on this page.

Using ξ as an order parameter to explore this transition, we have generated the phase diagram in the plane spanned by $\eta_k\sigma^0$ and γ in Fig. 5.4. The crossover region with statistical coexistence of both fracture disorder regimes is very narrow. As seen in Fig. 5.4, localization regime occurs for $\gamma > 2.5$ and $\eta_k\sigma^0 > 0.45$. In the later section, we reconfirm that ξ is a

³ ξ is determined by the fitted function of a sum of two Gaussians with six fitting parameters, including A_1 and A_2 . Most of errors for ξ are calculated based on the variances of A_1 and A_2 . A distribution in which the other peak is hardly observed by the eye is still fitted by the function of two Gaussians, but the predicted values of fitting parameters can be very sensitive to the parameter initialization. In this case, the errors equate to the differences in values of A_1 and A_2 from different reasonable parameter initializations.

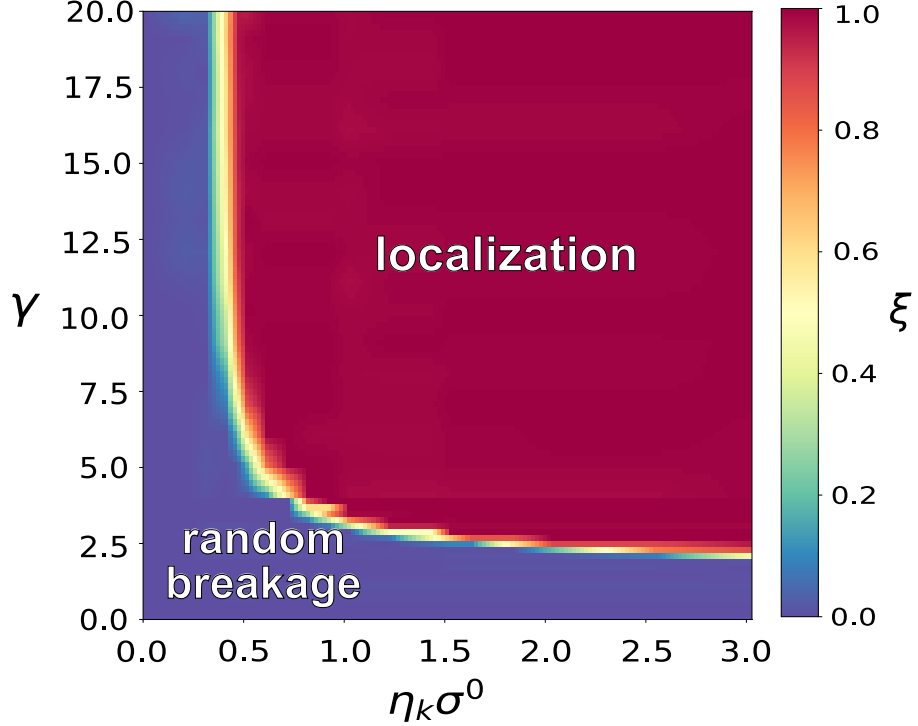


Figure 5.4: Phase diagram, illustrated as a color map, in the plane spanned by γ and $\eta_k\sigma^0$. The diagram was generated using Fig. 5.3 with ξ as order parameter. Regimes of random breakage and localization are clearly discernible, separated by a narrow crossover region.

suitable parameter to assess this transition between the two regimes analyzing the growth dynamics of the largest crack .

We also report that for $\eta_k\sigma^0 > 3.0$, at $\gamma = 1 - 2.5$, three peaks were observed. Fig. 5.5 shows the frequency distribution of percolation thresholds which exhibits three distinguishable peaks for the case of $\gamma = 1.2$ and $\eta_k\sigma^0 = 5.0$. We seek an explanation of this "fine structure" of the distribution. The third peak may come from the separation of the second peak. A possible explanation is that they correspond to two highly correlated regimes that both exhibit localized damage patterns at different points in time (see damage dynamics analysis in Fig. 5.8). One of the regimes exhibits the correlated crack growth mechanism very early on, right after a few isolated clusters are generated in the initial stage of random nucleation, whilst the other regime has a pattern of localized damage that occurs much later driven by cluster merging processes. We expect this fine structure of the distribution of p_c^L to show for $\eta_k\sigma^0 < 3.0$ also, but within a very narrow range of γ which is missing in our numerical analysis.

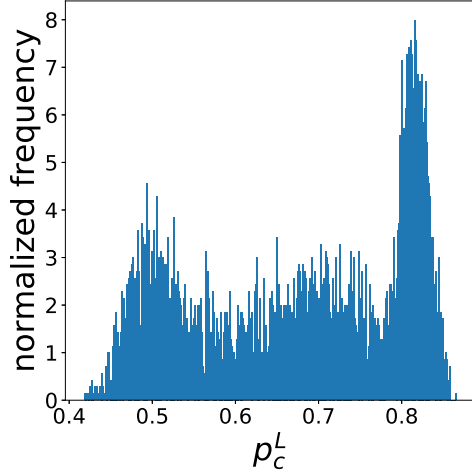


Figure 5.5: Normalized frequency distribution of percolation thresholds that exhibits three discernible peaks for the case with $\gamma = 1.2$, $\eta_k \sigma^0 = 5.0$.

5.3 Percolation Behaviour

We inquire whether the percolation thresholds decrease with increasing correlation strength as expected intuitively. In this section, we present both the two expectation values of the two separate peaks in the distribution of percolation thresholds and the average percolation threshold to illustrate the overall percolation behaviour.

5.3.1 Expectation Values of the Two Peaks

We examine the distribution of percolation thresholds by analyzing the expectation values μ_1 and μ_2 of the two Gaussian distributions fitted to the two respective peaks in the distribution. The mean value of the uncorrelated percolation case (when $\gamma \rightarrow 0$ or $\sigma^0 \rightarrow 0$) is $p_c^{\text{uncor}} = 0.4955 \pm 0.0002$ for $L = 100$ ⁴. Fig. 5.6 (a) and (b) show μ_1 and μ_2 as functions of γ for different stresses $\eta_k \sigma^0$. As can be seen in Fig. 5.6 (a), μ_1 , which represents random breakage events, closely approaches p_c^{uncor} . As a function of γ , μ_1 decreases at first. The minimum in μ_1 is found at around $\gamma = 1 - 2$. The variation of μ_1 is however, small.

More significant changes are seen in the plot of μ_2 as a function of γ . The values of μ_2 vary in the range $0.53 \leq \mu_2 \leq 0.64$. In the regime of weak initial stress, μ_2 increases from an initially low value at small γ to asymptotically approach a plateau value for $\gamma \geq 10$. At high initial stress, $\eta_k \sigma^0 > 0.5$, μ_2 goes through a sharp maximum at small γ and then relaxes to a small plateau upon increasing γ . The larger is $\eta_k \sigma^0$, the sharper is the maximum and the lower is the plateau value.

⁴For an infinite square lattice, the exact percolation threshold is $p_c = 0.5$ [99].

For $\eta_k\sigma^0 < 3.0$, the variances of both peaks in the distribution of percolation thresholds, viz., σ_1 and σ_2 , increase with ξ , but the peak due to random breakage is narrower, with σ_1 in the range 0.01-0.02, whereas σ_2 lies in the range 0.05 to 0.12. In the localization regime, fracture formation on the lattice is dominated very strongly by the sample-spanning cracks, which exhibits a large variability in shape among different simulation runs, resulting in larger σ_2 . In the random breakage regime, percolating clusters exhibit a high degree of similarity for different simulation runs performed at a given set of parameters, resulting in a narrow peak in the probability distribution of percolation thresholds. The general trends are that σ_1 and σ_2 increase with increasing $\eta_k\sigma^0$ and γ , with the more regular and pronounced trends seen in σ_2 . High sensitivities of σ_2 to these parameters are seen in the random breakage regime. In the localization regime, at $\gamma > 5$, σ_2 becomes independent of γ .

5.3.2 Average Percolation Threshold

The average percolation threshold p_{av}^L is defined in Eq. (2.15) in terms of the distribution of percolation thresholds p_c^L . Fig. 5.7 (a) illustrates p_{av}^L as a function of γ for different values of $\eta_k\sigma^0$. For all values of $\eta_k\sigma^0$, p_{av}^L drops below p_c^{uncor} at low γ . At higher value of γ , it exhibits a dramatic growth to a value much higher than p_c^{uncor} . We notice for $\eta_k\sigma^0 > 0.60$, after reaching a maximum, p_c^L then drops for large γ . Especially for very high stress $\eta_k\sigma^0 > 3$, it can decline to a plateau even lower than p_c^{uncor} . As can be seen, this overall behaviour of p_{av}^L is consistent with the variation of μ_1 and μ_2 illustrated in Fig. 5.6 (a) and (b). We will not elaborate to discuss it into details.

We here present p_{av}^L as a function of $\eta_k\sigma^0$ for different values of γ to examine whether there is a change in percolation behaviour with σ^0 . Fig. 5.7 (b) depicts that p_{av}^L rises at first and then drops as an overall trend for all γ . For GLS ($\gamma = 2$), we observe p_c^L decreases from p_c^{uncor} at first, consistent with the observation of the minimum values in p_c^L in Fig. 5.7 (a) at around $\gamma = 0 - 2$. As for $\gamma > 2$, we do not know whether p_{av}^L decrease at first at small stress $\eta_k\sigma^0$ also. We should examine the tiny range of stress at around $0 < \eta_k\sigma^0 < 0.2$, but we have not currently obtained adequate data to verify this.

To conclude, it defies our intuition that the overall percolation threshold p_{av}^L will *always* decrease with a higher correlation strength. The characteristics of the percolation behaviour are as follows: (1) At $\xi \sim 0$, which corresponds to a weakly correlated system, p_{av}^L reduces slightly with increasing ξ . A slight increase in the correlation strength accelerates the merging of clusters and thereby promotes formation of the percolating cluster. Similar behaviour was observed for prototypical long-range correlated percolation models explored in Refs. [117, 118, 121, 123, 124, 126, 153] (as reviewed in Section 2.2.2). (2) As ξ increases further (i.e, at the crossover region), we observe a subsequent growth of p_{av}^L . The system appears localized damage merely at one or a few dominated clusters, after the initial stage of random nucleation. This pattern of damage mechanism does not contribute to the merging of many random isolated clusters to form a percolating crack. Harter in his work [117] also

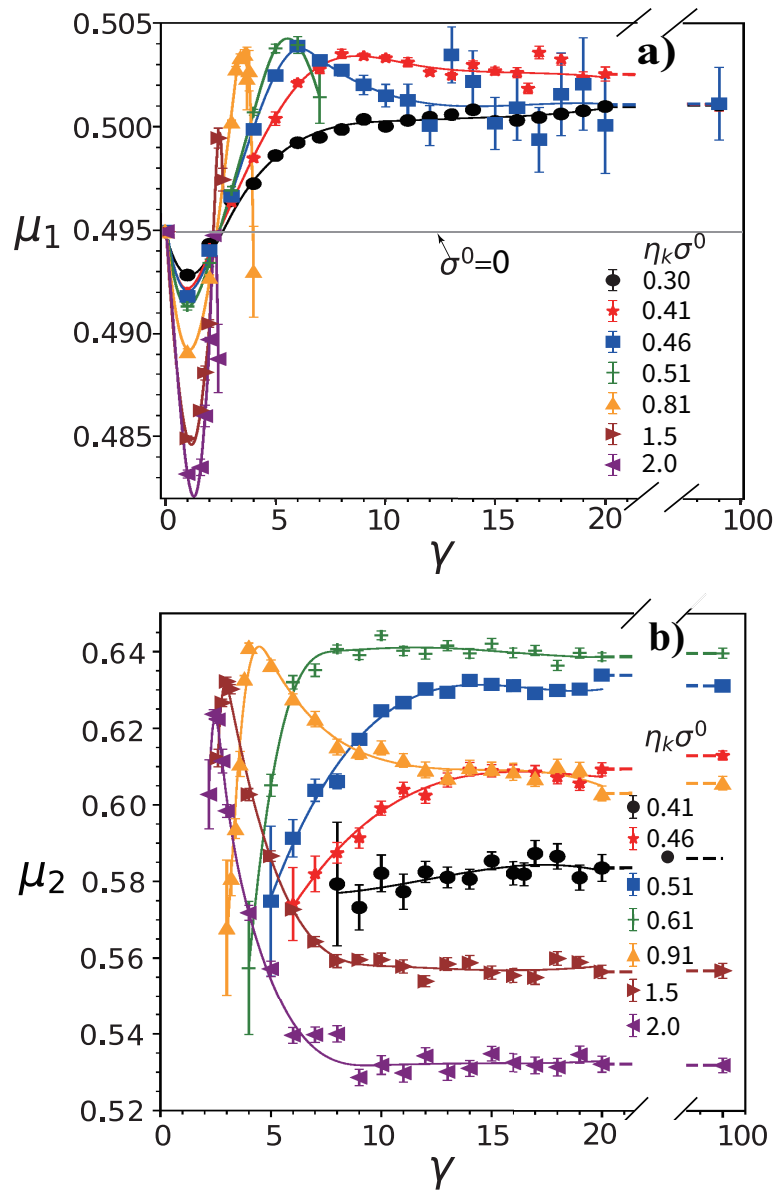


Figure 5.6: Plots of (a) μ_1 and (b) μ_2 as a function of γ with $\eta_k \sigma^0$ as parameter. The reader can refer to footnote 3 for details of the error estimates of μ_1 and μ_2 .

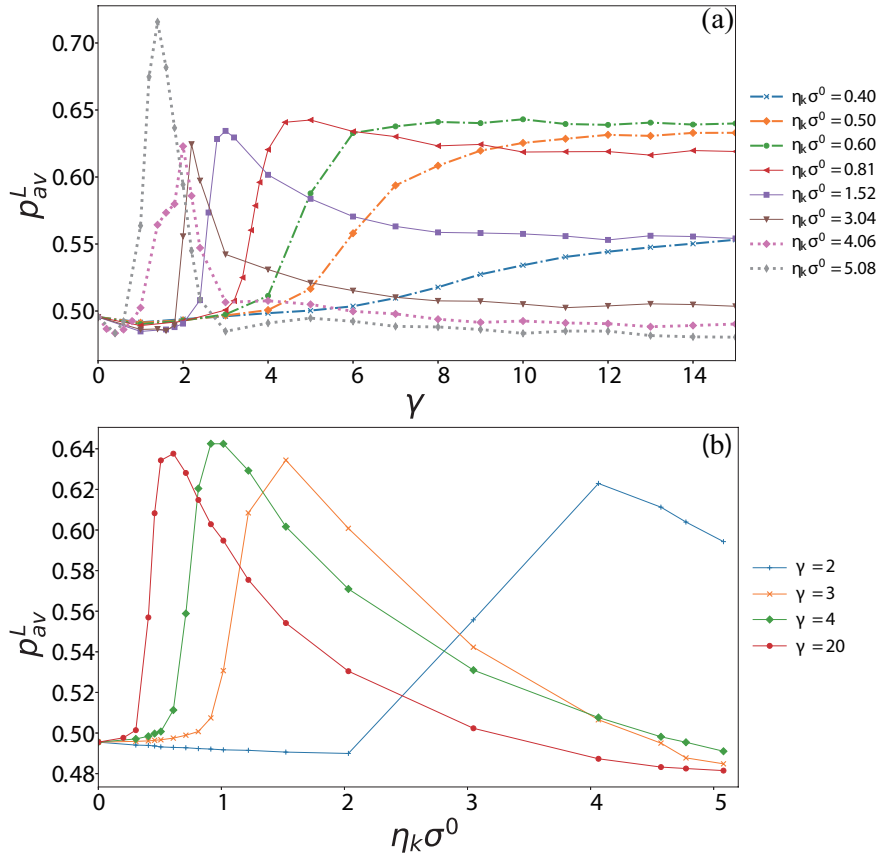


Figure 5.7: Plots of average percolation thresholds p_{av}^L over (a) γ with $\eta_k \sigma^0$ as parameter, and (b) $\eta \sigma^0$ with γ as parameter. Error bars indicate standard deviations of the means of the percolation thresholds p_{av}^L .

showed that the percolation thresholds reduce but will increase again for sufficient correlation length. (3) When approaching $\xi \sim 1$, the localized damage regime occurs at an early stage. p_{av}^L once again drops (even below p_c^{uncor}), and this was previously reported in the nucleation and growth study of Ref. [154]. In the next section, we will support the above explanations of the peculiar percolation behaviours by analyzing the cluster structures.

5.4 Cluster Structure Analysis

In this section, we characterize the cluster structures in both dynamic and static ways. We discuss the dynamics of the largest crack in Section 5.4.1. The characterization of growth of the largest crack reveals three different damage dynamical processes for the random breakage regime, the localization regime and their crossover region, thus it provides further support for the introduced order parameter ξ . Moreover, the dynamics of the largest crack reveals how a cluster grows into a percolating cluster, hence it gives insight further into the variation of the percolation thresholds as a function of $\eta_k \sigma^0$ and γ . In section 5.4.2, we analyze the cluster structures particularly at the onset of the percolation. We give a static analysis of the largest crack at a percolation threshold, that illustrates the variation of the percolating crack size as a dependence of $\eta_k \sigma^0$ and γ . We also analyze the moments of the clusters. In the next chapter, the 0th moment of cluster size distribution will be employed to separate the random breakage regime and the localization regime further for larger lattice sizes.

5.4.1 Dynamics of the Largest Crack

We analyze the size of the largest cluster of broken bonds S_L , normalized by the total number of bonds N , as a function of the fraction of failed bonds N_b/N . For damage propagation by the random breakage, formation of a sample spanning cluster of broken bonds proceeds in three stages, illustrated with the red solid line in Fig. 5.8: I. random nucleation of isolated cracks (slope ~ 0); II. merging of cracks into larger clusters (slope $\gg 1$); and III. growth of the largest crack (slope ~ 1). Regardless of the overall correlation strength ξ , stage I is always observed since the initial stress is uniformly distributed on the lattice. As $\eta_k \sigma^0$ or γ become larger, i.e., the system shifts towards the localization regime in Fig. 5.4, stage II, the merging stage, becomes less pronounced. In this regime, correlated growth of a single crack dominates. Eventually, for systems with $\xi \sim 1$ (dash dotted line), a direct transition from stage I to stage III occurs, bypassing the merging stage. Upon increasing the value of ξ , the accumulation of stress on the largest crack accelerates, which has a significant impact on the localization regime, affecting the percolation threshold, and time-to-fracture. This strong acceleration effect is due to the exponential breakage rule considered in our work. The effect is much weaker if a power-law breakage rule is considered, as in Ref. [87], in contrast to the unchanged fracture pattern in study of Ref [155] even for LLS scheme.

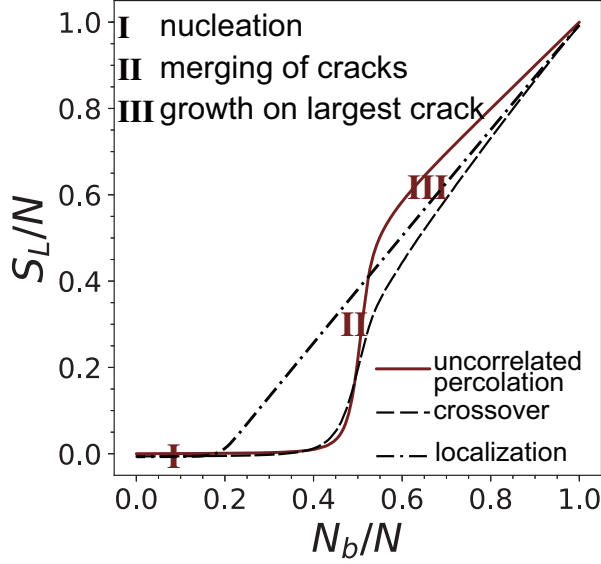


Figure 5.8: Normalized growth of the largest crack size S_L/N with the fraction of failed bonds N_b/N in the lattice. Three regimes are shown: uncorrelated percolation, where $\xi = 0$ (red solid line); crossover, where $0 < \xi < 1$ (dashed line); and localization, where $\xi \simeq 1$ (dash dotted line). Three growth stages are indicated: I. nucleation of cracks, II. merging of cracks and III. growth concentrated on the largest crack.

Fig. 5.9 illustrates the growth dynamics of the largest cluster in three stress ranges: (a) $\eta_k\sigma^0 = 0.30$, (b) $\eta_k\sigma^0 = 0.46$, and (c) $\eta_k\sigma^0 = 2.0$. S_L varies from the GLS to the LLS, corresponding to different fracture regimes. When $\eta_k\sigma^0 = 0.30$, the overlap of the S_L curves in Fig. 5.9 (a) indicates that only the random breakage mechanism occurs, consistent with $\xi \sim 0$ for $\eta_k\sigma^0 \leq 0.30$ in Fig. 5.3. As for Fig. 5.9 (b), representing the crossover region, as shown by the largest crack, localized damage was not observed even for the extreme case of LLS (i.e., for large γ). But the merging stage is shrinking, indicating the transition to localization. In Fig. 5.9 (c), all three pathways of formation and growth of clusters are present, corresponding to parameter ranges $0 \leq \gamma \leq 2$ (the random breakage regime), $2.2 \leq \gamma \leq 2.4$ (the crossover region), and $\gamma \geq 2.6$ (the localization regime).

Fig. 5.10 illustrates the growth for (a) $\gamma = 1$, (b) $\gamma = 3$, and (c) $\gamma = 100$. S_L varies from low to high stress ranges. We notice for $\gamma \geq 3$ as shown in Fig. 5.10 (b) and (c), all three pathways of formation and growth of clusters are present, corresponding to the random breakage regime ((b) $\eta_k\sigma^0 \leq 0.81$ and (c) $\eta_k\sigma^0 \leq 0.20$), the crossover region ((b) $0.91 \leq \eta_k\sigma^0 \leq 1.22$ and (c) $0.33 \leq \eta_k\sigma^0 \leq 0.46$) and the localization regime ((b) $\eta_k\sigma^0 \geq 1.52$ and (c) $\eta_k\sigma^0 \geq 0.81$). The higher γ is, the earlier the correlated crack growth occurs during the dynamics (for a same $\eta_k\sigma^0$). Similar damage behaviours are also shown in Fig. 5.9 (c) for high stress $\eta_k\sigma^0 = 2.0$, varying γ from GLS to LLS. Fig. 5.10 (a) shows the dynamics of S_L when $\gamma = 1$ (GLS): the higher stress promotes the merging of clusters and accelerates

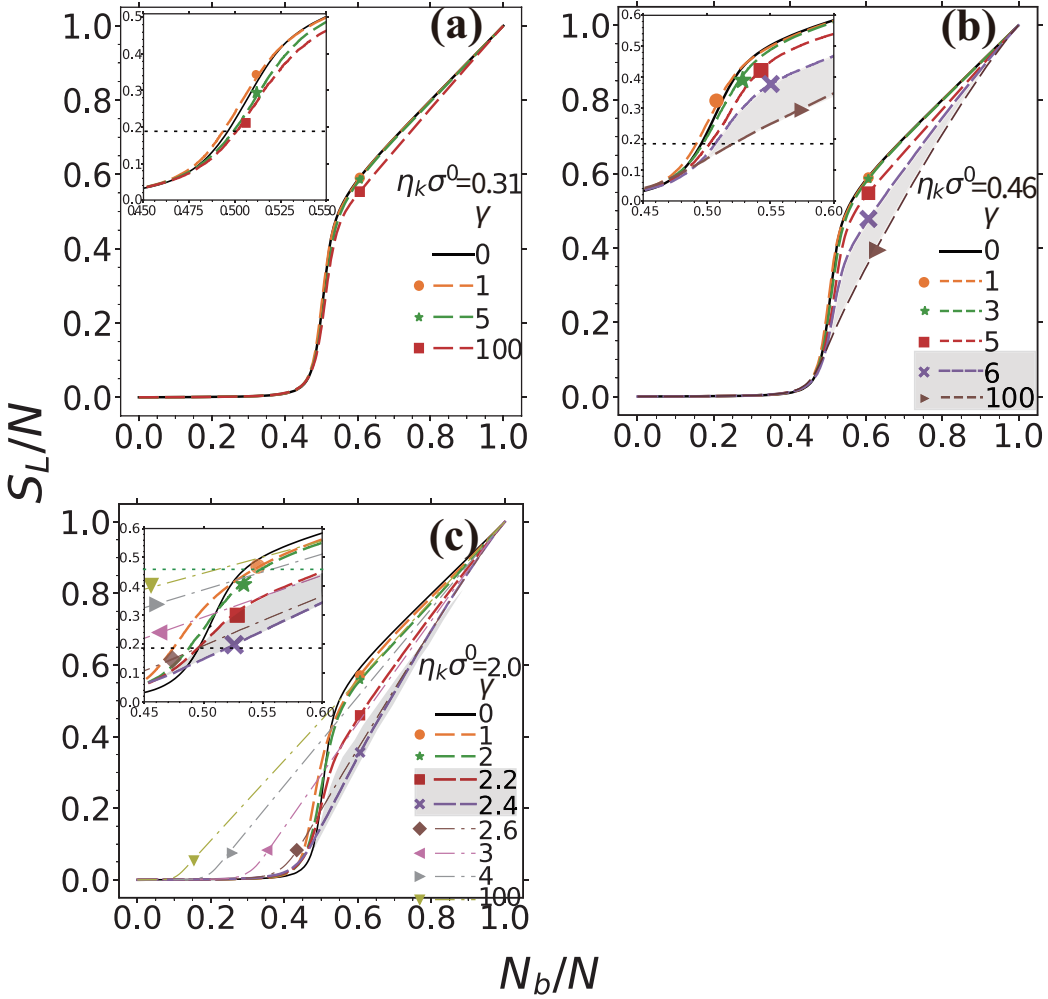


Figure 5.9: Normalized growth of the largest crack size S_L/N with the fraction of failed bonds N_b/N in the lattice for different stresses with γ as parameter. The black horizontal dashed lines and green horizontal dashed line indicate S_L/N at a percolation threshold in the uncorrelated percolation case (insets of (a)-(c)) and in the localization regime (inset of (c)) respectively. Cluster growth is shown for different ranges regimes in (a) with $\eta_k \sigma^0 = 0.30$, (b) with $\eta_k \sigma^0 = 0.46$, and (c) with $\eta_k \sigma^0 = 2.0$. The shaded area indicates the crossover region where $0 < \xi < 1$.

the damage to the stage of the correlated crack growth. This dynamic behaviour (Fig. 5.10 (a)) is different with the overlaps of the curves in Fig. 5.9 (a) (low stress $\eta_k\sigma^0 = 0.30$ for varying γ), even though both illustrations correspond to the random breakage regime.

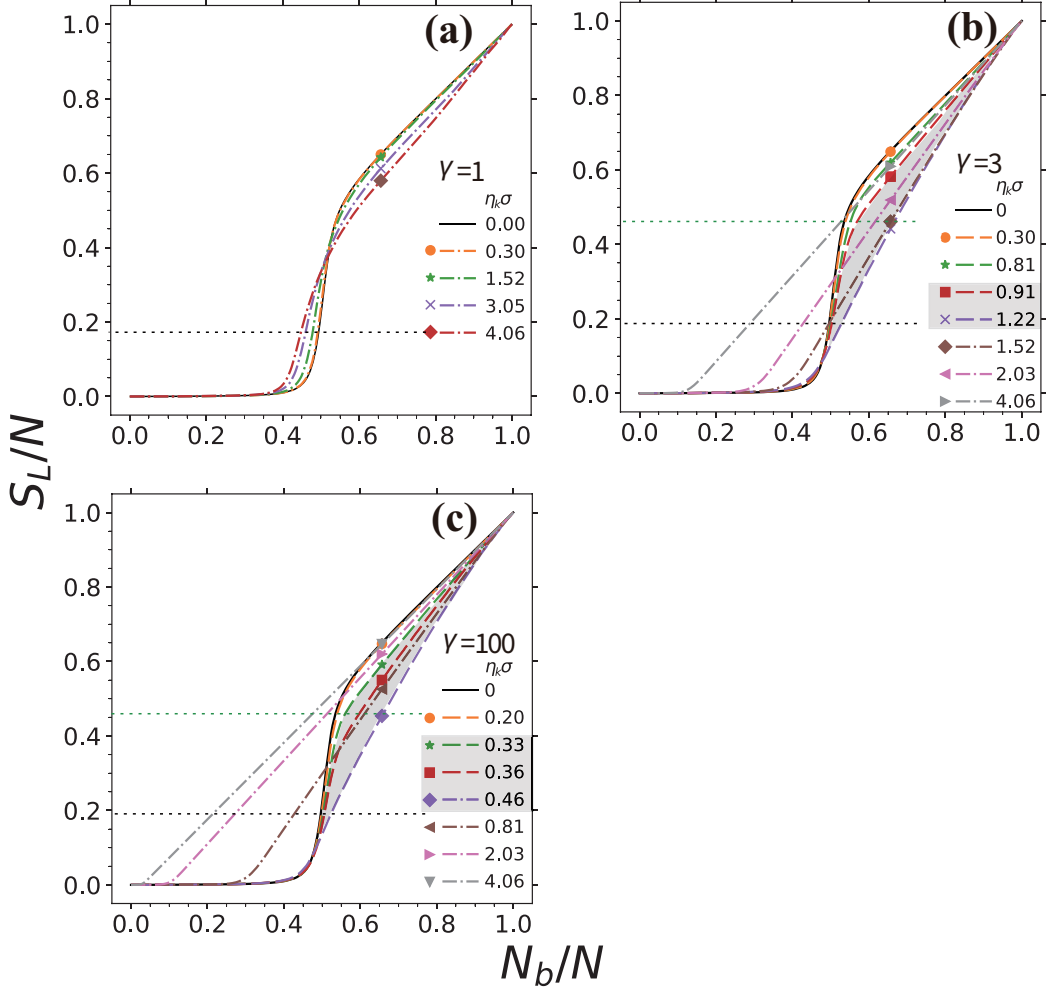


Figure 5.10: Normalized growth of the largest crack size S_L/N with the fraction of failed bonds in the lattice for different γ with $\eta_k\sigma^0$ as parameter. The black horizontal dashed lines and green horizontal dashed line indicate S_L/N at a percolation threshold in the uncorrelated percolation case ((a)-(c)) and in the localization regime ((c)) respectively. Cluster growth is shown for different ranges regimes in (a) with $\gamma = 1$, (b) with $\gamma = 3$, and (c) with $\gamma = 100$. The shaded area indicates the crossover region where $0 < \xi < 1$.

As can be seen in Figs. 5.9 and 5.10, the S_L dynamic curves of $\xi \sim 0$, $\xi \sim 1$ and $0 < \xi < 1$ all correspond to three distinctive paths. This provides further support for the validity of order parameter ξ . Localization regime corresponds that the direct transition from stage I to stage III, bypassing the merging stage. Interestingly, the onset of the localization regime ($\xi \sim 1$) corresponds that that cluster merging stage is skipped at the first time (see Fig. 5.9 (c) and Fig. 5.9 (b) and (c)).

We also attempt to seek a qualitative explanation of the peculiar variation of percolation thresholds by examining the crack growth dynamics. The horizontal dashed lines (black) in Fig. 5.9 (insets) and Fig. 5.10 indicate S_L/N (at p_c^L) of the uncorrelated percolation case and the horizontal dashed lines (green) indicate S_L/N (at p_c^L) when $\xi \sim 1$. The horizontal dashed lines help roughly compare how fast a system reaches a percolation point. A further discussions of the variation of percolation threshold will be shown in Fig. 5.11 (d). We confirm with Fig. 5.10 (a) that when $\xi \sim 0$, the early clusters merging contributes to the temporary drop of p_{av}^L at around $\gamma = 1 - 2$. The higher the stress, the lower the minimum of the percolation threshold (compare with Fig. 5.6 (a)). We notice that in the crossover region (the shaded areas), the system takes a larger damage fraction (N_b/N) to reach percolation (black dashed lines) upon a further increase of ξ , until the system reaches the onset of the localization regime ($\xi \sim 1$). After that onset, the stronger the localized regime is, the earlier the N_b/N reaches the percolation threshold (green dashed lines). The above damage dynamics analysis provides a further support for the overall peculiar percolation behaviour that p_{av}^L has slight drop at $\xi \sim 0$ but later grows and eventually drops when ξ increases from 0 to 1.

5.4.2 Cluster Structures (Static)

Now we analyze the static cluster structures. The k th moment of the cluster distribution is defined as

$$m_k = \sum_s s^k n_s, \quad (5.2)$$

where n_s represents the number of clusters of size s , averaged over n MC runs. m_0 is the total number of clusters and m_1 represents the total number of broken bundles in the lattice. The average cluster size S_{av} is equal to m_1/m_0 . As we analyze the cluster structure at the critical point, viz., the onset of percolation, we change the notations of m_0 , m_1 and S_{av} to $m_{0,c}$, $m_{1,c}$ and $S_{av,c}$ respectively. We also analyze the largest crack size at a percolation threshold $S_{L,c}$.

Fig. 5.11 illustrates (a) $m_{0,c}$, (b) $m_{1,c}$, (c) $S_{av,c}$ and (d) $S_{L,c}$ as a function of the parameter γ for different stress ranges. Fig. 5.11 (b) shows $m_{1,c}$, i.e, the number of failed bundles at a percolation threshold, thus we get,

$$m_{1,c}(\gamma, \sigma^0) = p_c^{av}(\gamma, \sigma^0)N. \quad (5.3)$$

As we already illustrated the overall change of $p_c^{av}(\gamma, \sigma^0)$ in Fig. 5.7 (a), here we will not repeat the discussions. We particularly look into $m_{0,c}$, $S_{av,c}$, and $S_{L,c}$.

Fig. 5.11 (b) illustrates $m_{0,c}$. For a system at $\xi \sim 0$, as the lattice is dominated by many isolated small size clusters, a slight increase of the correlation strength helps the merging of the clusters, reducing the total number of clusters. Upon a further increase of ξ , the correlated damage grows only on one or few cracks, but this localization pattern does

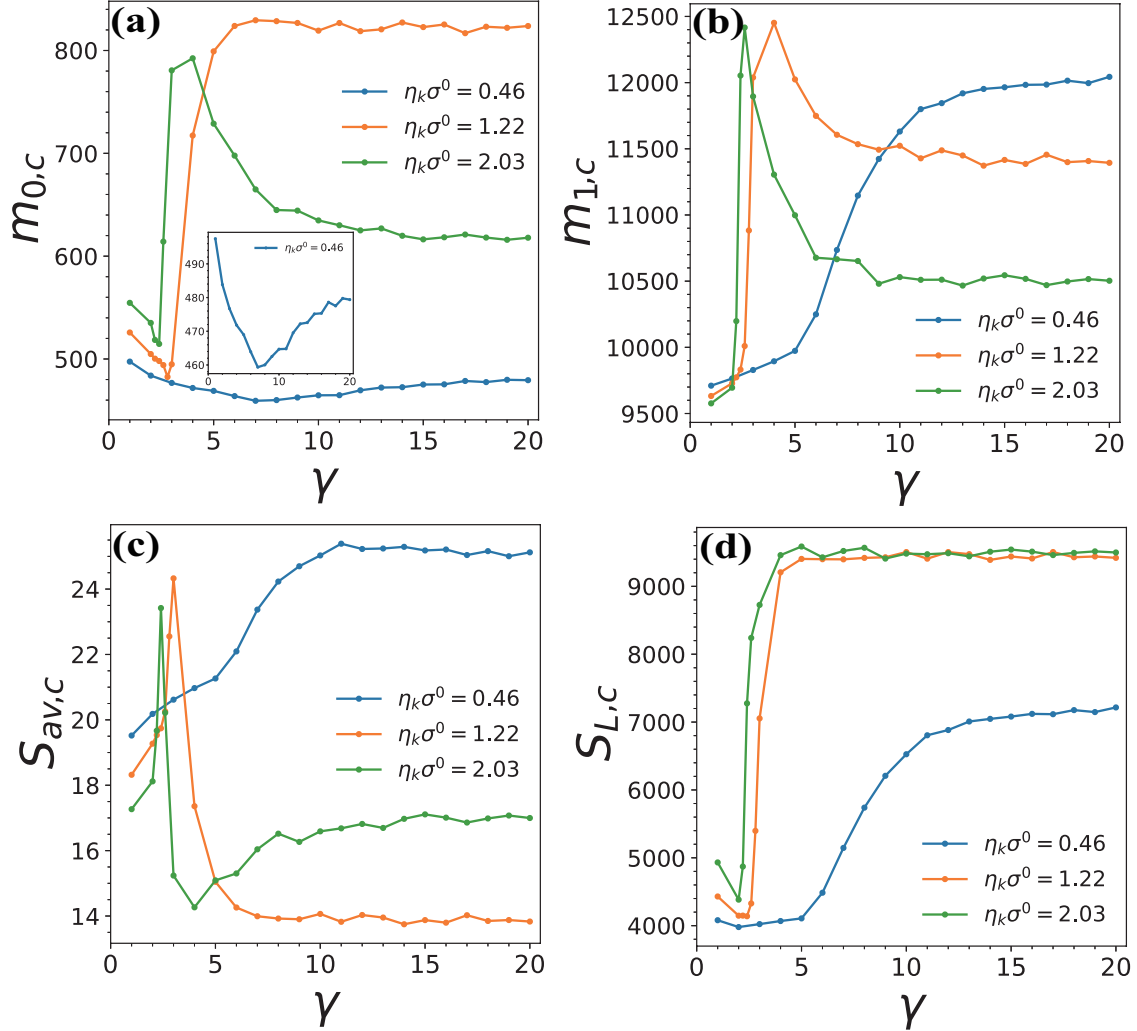


Figure 5.11: Cluster structures (a) $m_{0,c}$, (b) $m_{1,c}$, (c) $S_{av,c}$ and (d) $S_{L,c}$ at a percolation threshold as a function of γ for different stresses $\eta_k \sigma^0 = 0.46, 1.22, 2.03$. The inset in (a) shows $m_{0,c}$ for $\eta_k \sigma^0 = 0.46$.

not contribute to connections of the isolated clusters, resulting in a climb of $m_{0,c}$. This explains the trend for stress $\eta_k \sigma^0 \leq 1.22$. However, for a very high stress ($\eta_k \sigma^0 = 2.03$), corresponding to $\xi \sim 1$, the localized damage occurs at a very early stage (see dash dotted line in Fig. 5.8) just after the occurrence of a very few isolated clusters driven by the random nucleation. (These descriptions of the physical dynamics have been presented in Section 5.3.2.) Interestingly, we find the minimum of $m_{0,c}$ just happens at the crossover region. In the next chapter, a quantitative analysis of $m_{0,c}$ will be employed for the phases (or regimes) separation for $L > 150$.

Fig. 5.11 (c) shows $S_{av,c}$, that is equal to $m_{0,c}/m_{1,c}$. We observe the sharp maximums for $S_{av,c}$ at high initial stresses: roughly at the points $\gamma = 3$ for $\eta_k \sigma^0 = 1.22$ and 5 for $\eta_k \sigma^0 = 2.03$ respectively. These points falls into the crossover region. As for low stress ($\eta_k \sigma^0 = 0.46$), $S_{av,c}$ has a continuous increase as a function of γ .

Fig. 5.11 (d) shows $S_{L,c}$, the largest crack size, at a percolation threshold varying with $\eta_k \sigma^0$ and γ . We observe when $\xi \sim 0$, $S_{L,c}$ has a relatively moderate decrease attributed from the increase of the clusters merging. Upon a further increase of ξ , in other words, the system takes a crossover to the onset of localization, a rapid growth of $S_{L,c}$ is observed until $S_{L,c}$ reaches a higher plateau ($S_{L,c}/N_b = 0.46$ at $\xi \sim 1$). Because the damage remains concentrated in the same domain, it overall requires a larger $S_{L,c}$ to form a cluster percolating both sides of the lattice. In other words, the fractal dimension of the largest crack area for a system in the localization regime is much larger than that in the random breakage regime⁵.

5.5 Time-to-Fracture

Next, we analyze the time-to-fracture, or lifetime t_{PEM} of PEMs. In studies of fiber bundle models [82, 87, 137], fibrous materials can be considered to fracture when all material elements fail. In our present model, however, a PEM is assumed to fracture when a percolating crack appears for the first time as reactive gases can permeate across the sample-spanning crack. Fig. 5.12 displays t_{PEM} for the evaluated ranges of σ^0 and γ . The frequency distribution of t_{PEM} values, obtained in each case over n MC runs performed under identical conditions, is shown for three different systems, with details given in the caption. It exhibits a single peak for the random breakage regime, i.e., for $\xi \sim 0$, shown in Fig. 5.12 (a), as well as in the localization regime with $\xi \sim 1$, shown in Fig. 5.12 (c). A combination of two peaks can be discerned in the crossover regime, Fig. 5.12 (b). Using these distributions, we have calculated the expectation value of t_{PEM} , which is depicted as a function of $\eta_k \sigma^0$ for various

⁵The fractal dimension of our 2D lattice describes how the area increases with its linear size. For a system of $\xi \sim 1$, the fractal dimension of the largest damage area tends to be 2 as the bundles in that domain almost have a complete breakdown, whereas the fractal dimension of a system in the random breakage has a portion of bundles failed in the largest crack area, so it is between 1 to 2 [156].

γ in Fig. 5.13 (a), and, alternatively, as a function of γ for various $\eta_k\sigma^0$ in Fig. 5.13 (b). Due to the exponential bundle breakage law, introduced in Eq. 2, t_{PEM} follows essentially an exponential dependence on $\eta_k\sigma^0$. The slope of the semi-logarithmic plot in Fig. 5.13 (a) decreases upon transition from random breakage to localization regime.

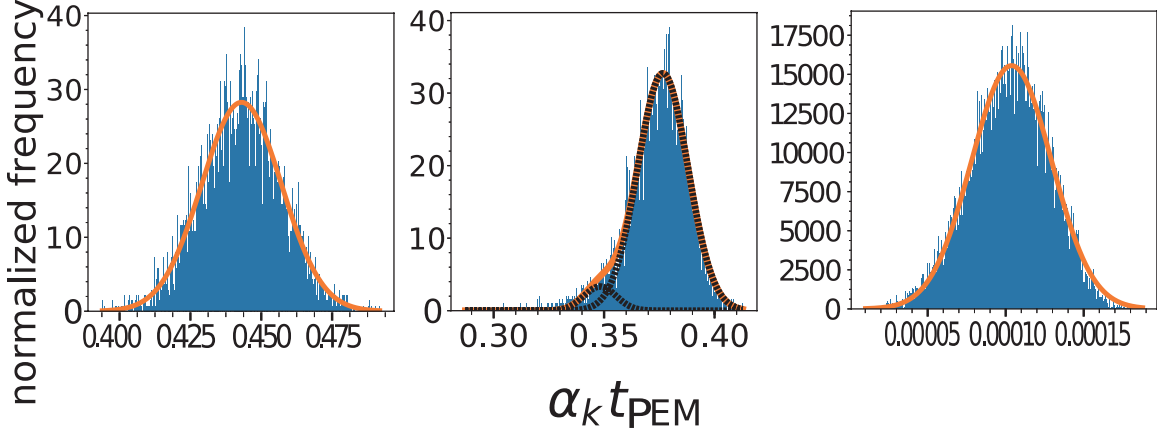


Figure 5.12: Frequency distributions of the time to fracture t_{PEM} (normalized to α_k) for systems in the regime of random breakage (left, $\eta_k\sigma^0 = 0.30$ and $\gamma = 4.0$), crossover region (middle, $\eta_k\sigma^0 = 0.41$, $\gamma = 10$) and localization regime (right, $\eta_k\sigma^0 = 5.0$, $\gamma = 100$). The distribution in the crossover region exhibits a superposition of two Gaussian peaks.

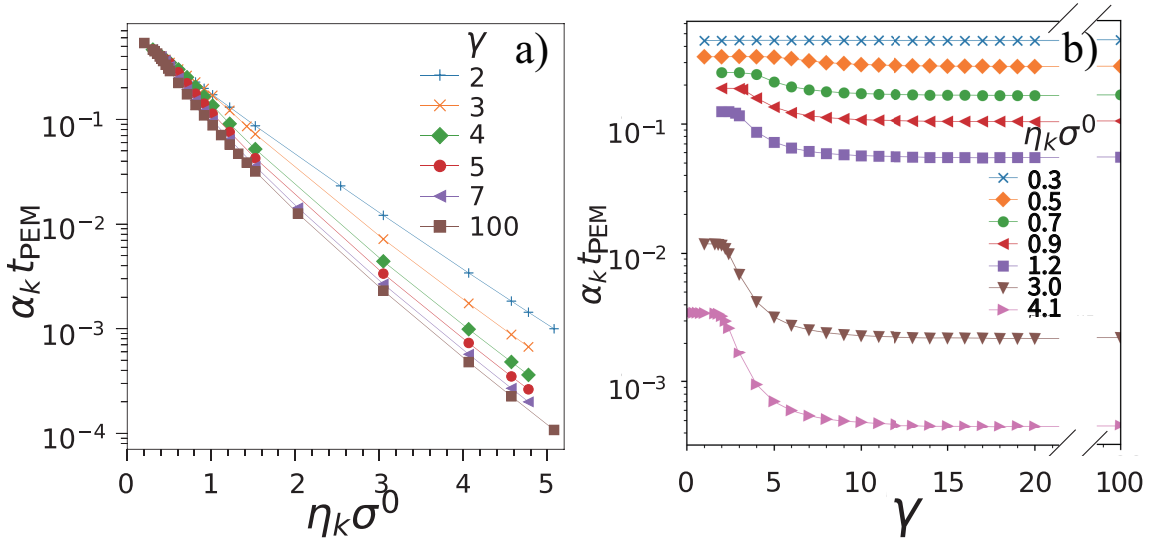


Figure 5.13: Time-to-fracture t_{PEM} (normalized to α_k) (a) on a log-scale as a function of $\eta_k\sigma^0$ with γ as parameter and (b) as a function of γ with $\eta_k\sigma^0$ as parameter.

Fig. 5.13 (b) displays the time-to-fracture of the lattice, t_{PEM} , as a function of γ . It exhibits a peculiar transition between two plateaus, from a higher value in the random breakage regime, attained for $\gamma < 2$ (ELS), to a lower value in the localization regime that

is approached asymptotically for $\gamma > 5$ (LLS). The magnitude of the transition shows a high sensitivity to $\eta_k \sigma^0$. At the highest stress value included in the plot, the two plateaus differ by a factor of 10, whereas at low stress values the transition becomes insignificant, illustrating the concerted impact of stress and effective range of stress transfer on the dynamics of the percolation transition.

Fig. 5.14 shows the color map of t_{PEM} as a function of both γ and $\eta_k \sigma^0$. For the particular case $k = 1$ and $T = 298\text{K}$, dimensional scales of $\sigma^0(\text{MPa})$ and t_{PEM} are shown on the upper abscissa (298K) and at the right side of the color bar (298K), respectively. To find t_{PEM} as a function of σ^0 and γ at other k , the parameters in Table 3.1 should be used. To study the impact of temperature, values of α_1 and η_1 are recalculated based on an assumption that activation energy E_a and activation volume ν remain the same, with ratios in Table 3.1 remaining unaffected by T . The upper abscissa (353K) and the right side of the color bar (353K) shows an example of the effect of T on t_{PEM} in three different stress regimes for $k = 1$. We notice that, compared to the phase diagram, the crossover curve the similar way, however the crossover ξ in phase diagram is quite narrow as shown in Fig. 5.14.

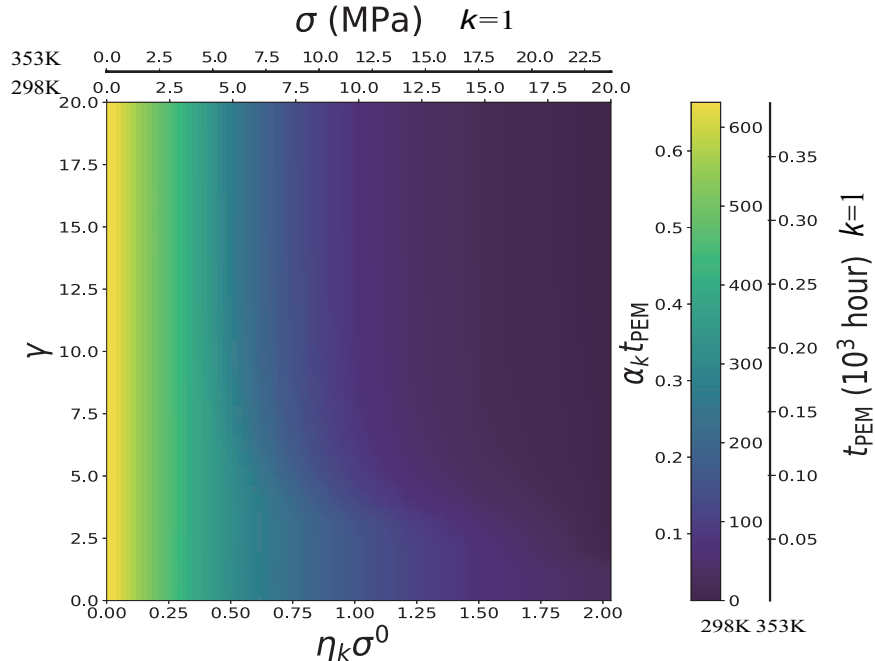


Figure 5.14: A color map of t_{PEM} in the γ and $\eta_k \sigma^0$ plane. Dimensional values of $\eta_k \sigma^0$ and t_{PEM} are shown at the abscissa (top) and the color map legend, respectively, for $T = 298\text{K}$ and $T = 353\text{K}$.

Table 5.1 shows the dimensional lifetime t_{PEM} (hours) obtained with our model for $\sigma^0 = 3\text{MPa}$, 5MPa and 30MPa , bundle sizes $k = 1, 3, 10$, and $T = 298\text{K}$ and 353K . We use $\tau_0 = 1.0 \times 10^{-11}\text{s}$, $E_a = 1.95 \times 10^{-22}\text{ kJ}$, $\nu = 0.418 \text{ nm}^3$ [13] as well as the parameters in Table 3.1 for the calculations of α_k and η_k . As can be seen, temperature has a marked impact on t_{PEM} , with the higher T destabilizing the bundle network. Moreover, t_{PEM} decreases

with increasing σ^0 , whereas a larger k has a stabilizing effect. While all these trends are reasonable, it will be important in future work to evaluate t_{PEM} for more realistic lattice configurations in 3D.

Table 5.1: Lifetime for $k = 1, 3, 10$ at $T = 298$ and 353K in the range of $\sigma^0 = 3 - 30\text{MPa}$. The two limits for the range of t_{PEM} values given in parentheses correspond to γ varying from 0 to 100 respectively.

k	$\sigma^0(\text{MPa})$	$T = 298\text{K}, t_{\text{PEM}} (\text{h})$	$T = 353\text{K}, t_{\text{PEM}} (\text{h})$
1	3	$4.2 \times 10^5 *$	$2.5 \times 10^2 *$
	5	$(3.1 - 2.6) \times 10^5$	$(2.0 - 1.6) \times 10^2$
	30	$(11 - 2.1) \times 10^3$	6.9-1.3
3	3	$5 \times 10^5 \dagger$	$3 \times 10^2 \dagger$
	5	$5 \times 10^5 \dagger$	$3 \times 10^2 \dagger$
	30	$(16 - 8) \times 10^4$	$(10 - 5.0) \times 10^1$
10	3	$6 \times 10^5 \dagger$	$4 \times 10^2 \dagger$
	5	$6 \times 10^5 \dagger$	$4 \times 10^2 \dagger$
	30	$3.2 \times 10^5 *$	$2.0 \times 10^2 *$

* The changes of these values of t_{PEM} are insignificant when varying γ .

\dagger These values corresponds to $\eta_k \sigma^0 < 0.2$, in which the data were not obtained. We approximated the values by extrapolating data in Fig. 5.13 (a).

5.6 Summary

An essential property in this chapter is the order parameter ξ introduced based on the distribution of percolation thresholds. The distribution exhibits two discernible peaks and can be employed to assess the crossover between the two disordered fracture regimes, the random breakage regime and the localization regime. In the crossover region, a coalescence of the two regimes can be observed for different statistical copies. We question which regime prevails when the lattice size approaches an infinite limit. The size effects will be analyzed and discussed in the next chapter.

Chapter 6

Results: Finite Size Effects

6.1 Overview

As reviewed in Section 2.1.3 (Fig. 2.16), Shekhawat *et al.* proposed a size-scaling theory which described a crossover between the two fracture regimes, i.e., the random breakage regime (percolation-type) and the localization regime (correlated crack growth). That theory predicts that the localization regime prevails when the lattice approaches the infinite size limit. Another scaling theory proposed by Kim *et al.* in Ref. [157] proposed that at any given finite load $\sigma^0 > 0$, the infinitely large system instantly breaks down. In this regard, we are interested in assessing the competition between the two fracture regimes within the framework of our present model when L increases.

Chapter 5 has presented a detailed analysis of the model considered in this thesis for a finite lattice at fixed size $L = 100$ over a parameter space of $\eta_k\sigma$ and γ . We introduced the order parameter ξ based on the distribution of percolation thresholds and ξ provides a reliable tool to assess the phase (or regime) separation (over $\eta_k\sigma$ and γ). The localization regime is characterized by $\xi \simeq 1$ while the random breakage regime corresponds to $\xi \simeq 0$. More intriguingly, we observe a narrow crossover region for $0 < \xi < 1$ in which the distribution of percolation thresholds exhibits two Gaussian-like peaks and both regimes coexist in a statistical sense. In this chapter, we attempt to generalize the analysis for varying lattices sizes to investigate the impacts of finite size effects.

The order parameter ξ , determined by the distribution of percolation thresholds requires thousands of MC realizations performed on a given set of L , $\eta_k\sigma$ and γ . However, due to the computational costs, we can obtain only 50-200 MC realizations at each set for $L > 150$ in most cases. Thus, we will tentatively employ another physical quantity to explore how the two fracture regimes shift with L in this chapter. Here we have considered L varying from 30 to 400. The structure of this chapter is as follows: Section 6.2 presents m_0 , the number of clusters, as another means to explore the crossover between random breakage regime and the localization regime. With an analysis of m_0 , we obtain a phase diagram that extends to varying sizes. In Section 6.3, we analyze ξ and the crack growth dynamics for several sets of

$\eta_k\sigma$ and γ in the (vicinity of) crossover region, to show competing manner of the two regimes for different L . Section 6.4 analyzes the variation of the average percolation threshold with L . This analysis is done to compare the peculiar change of percolation thresholds dependent on the correlation strength as shown in Section 5.3. Section 6.5 shows the lifetime of a PEM analysis for configurations of uncorrelated percolation, the crossover region and the localization regime. Lastly, in Section 6.6, preliminary studies of growth dynamics of small γ and σ^0 will be presented.

6.2 Phase Diagram

We have introduced the order parameter ξ in Chapter 5 to separate the regimes of random breakage and localization over $\eta_k\sigma^0$ and γ . Employing ξ , we have obtained the phase diagram of the two regimes for lattices of $L = 100$ in Fig. 5.4. However, ξ is determined by two Gaussian functions that are fitted to the distribution of percolation thresholds, and to get ξ within acceptable errors, we need to complete 2000 to 10000 Monte Carlo (MC) realizations for a single set of L , $\eta_k\sigma^0$ and γ . However, subject to the computational costs, for lattices of $L > 150$, we only carry out 50–200 MC realizations for each configuration.

Fig. 5.11 shows m_0 , the number of clusters, as a function of γ for low to high stress values. We observe the minimum values of m_0 fall into the narrow crossover region, viz., $0 < \xi < 1$. We now tentatively plot the minimum values of m_0 and compare them with the original phase diagram of $L = 100$ (Fig. 5.4) which was determined by ξ . In Fig. 6.1, these dots of the minimum values of m_0 are joined by a dashed line and this line overlaps with the narrow crossover region of the phase diagram. Thereby, we can adopt m_0 as an indicator for the phase separation for $L > 100$.

Employing m_0 to infer the "crossover lines" to separate the two fracture regimes, we generate new phase diagrams for $L = 100$, 250 and 400 in Fig. 6.2 accordingly. We also further verified that systems of $L = 250$ and 400 at "the crossover lines" have two discernible peaks in the distributions of the percolation thresholds, i.e., $0 < \xi < 1$, though we have not obtained a sufficient large number of MC realizations to fit the distribution with two Gaussian functions to deduce accurate values of ξ . Fig. 6.3 shows two examples of the distributions of the percolation thresholds obtained by performing (a) 325 MC realizations at a set of $L = 250$, $\eta_k\sigma^0 = 0.51$ and $\gamma = 5.5$, and (b) 80 MC realizations at a set of $L = 400$, $\eta_k\sigma^0 = 0.61$ and $\gamma = 4$.

We note that the crossover region shifts towards to smaller values of γ and $\eta_k\sigma^0$ upon increasing L . This suggests that, in the vicinity of the crossover region, the localization regime prevails for larger lattice sizes for $\eta_k\sigma^0$ and γ . To further support this, several physical quantities, including ξ and the largest crack growth, will be analyzed in the next section.

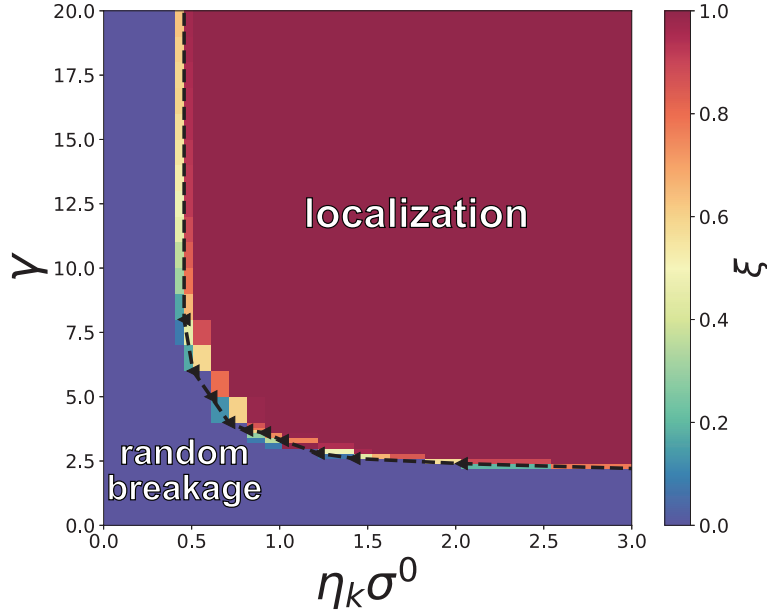


Figure 6.1: The minimum values of m_0 are shown by triangular dots linked by a dashed line. The color map represents the phase diagram (Fig. 5.4) in the plane spanned by γ and $\eta_k\sigma^0$ and was generated with the order parameter ξ . Regimes of random breakage and localization are separated by a narrow crossover region. The minimum values of m_0 clearly fall into the crossover region. Thus, minimum values of m_0 can be adopted to separate the two regimes for larger sizes L .

Clearly, the fracture regime is sensitive to the lattice sizes of systems in the vicinity of the crossover region¹. Now it comes to the question of the fracture regime for a parameter space of $\eta_k\sigma^0$ and γ that is far away from the crossover region when $L \rightarrow \infty$. We verified that only one (clear) Gaussian-like peak can be observed in the distributions of the percolation thresholds for systems of $\eta_k\sigma^0 = 0.2$, $\gamma = 100$ and sizes upto $L = 400$. At this point, because of the limited exploration of the size effect, we cannot verify that a system can eventually convert to the localization regime for $L \rightarrow \infty$ over the entire range of $\eta_k\sigma^0$ and γ . In Section 6.6, preliminary results relating to this question will be presented.

6.3 Transition of Fracture Regimes in the Crossover Region

In this section, we provide further support that in the vicinity of the crossover region, upon increasing L , the damage regime has a transition from the random breakage to the localization. We present an analysis of ξ and the largest crack dynamics to characterize the competing behaviours of the two regimes in this region.

¹Strictly speaking, the term "crossover region" in this section refers to a set of small values of $\eta_k\sigma^0$ and γ in which $0 < \xi < 1$ for $L = 100$.

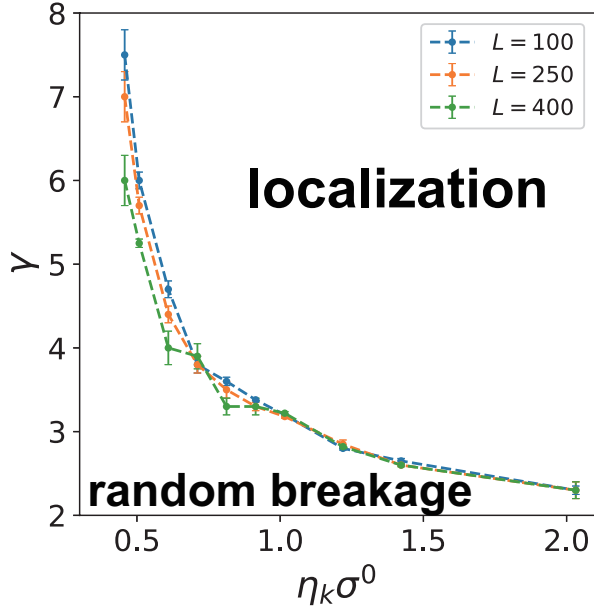


Figure 6.2: Phase diagrams in the plane spanned by γ and $\eta_k \sigma^0$ for different sizes $L = 100$, 250 and 400 . Regimes of the random breakage and the localization are separated by the "crossover line" determined by minimum values of m_0 . A minimum value is estimated by the minimum of the interpolated line applying to the discrete m_0 values, and the value's error bar is determined by its two closest m_0 values.

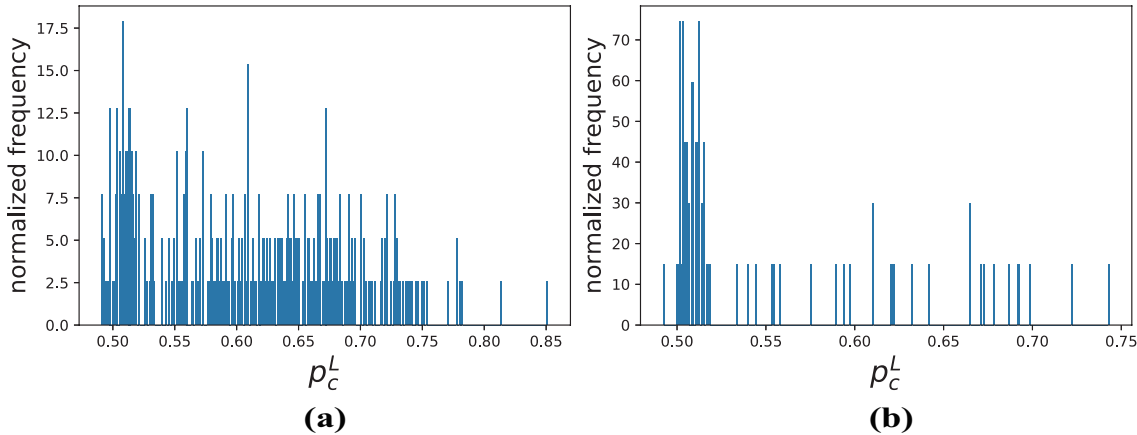


Figure 6.3: Frequency distributions of the percolation thresholds for (a) $L = 250$, $\eta_k \sigma^0 = 0.51$, $\gamma = 5.5$ performed by 325 MC runs and (b) $L = 400$, $\eta_k \sigma^0 = 0.61$, $\gamma = 4$ performed by 80 MC runs.

6.3.1 Order Parameter ξ

Even though we cannot obtain a complete analysis of ξ in a plane spanned by $\eta_k \sigma^0$ and γ due to the insufficient number of MC realizations, an effort can be made to examine several specific configurations in the crossover region. For example, we performed 3330 MC

realizations for the set of $L = 250$, $\eta_k\sigma^0 = 0.36$ and $\gamma = 100$, that reveals a frequency distribution of percolation thresholds that can be fitted with two Gaussian functions to acquire an acceptable value of ξ .

Fig. 6.4 shows ξ for $\eta_k\sigma^0 = 0.36$ and 0.41 in the LLS scheme ($\gamma = 100$) for several sizes L . Upon increasing L , ξ increases from 0 to 1. This supports that the system in the vicinity of the crossover region has a crossover from the random breakage regime to the localization regime as increasing L .

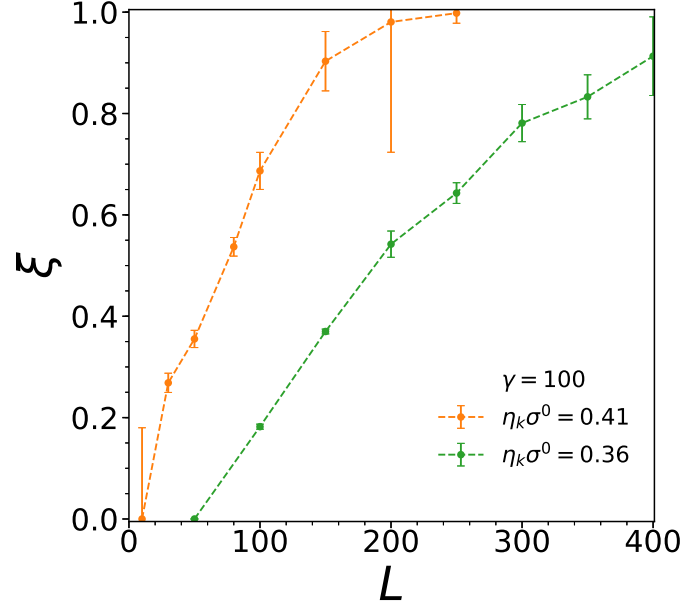


Figure 6.4: ξ obtained with $\eta_k\sigma^0 = 0.41$ and $\eta_k\sigma^0 = 0.36$ for $\gamma = 100$ (LLS) as a function of L in the crossover region. The method used to determine errors of ξ is described in footnote 3 on page 43.

6.3.2 Largest Crack Dynamics

The above characterization of ξ can be further verified by the analysis of largest crack growth. Fig. 6.5 shows S_L/N as a function of the damage fraction N_b/N for several sizes L obtained with $\eta_k\sigma^0 = 0.41$ in the LLS scheme (solid lines). We also illustrate the growth dynamics of uncorrelated percolation (dashed lines) for comparison. According to the three distinctive pathways that corresponds to the two fracture regimes and their crossover shown in Fig. 5.8, we verify that the systems of increasing L cross over to the onset of the localization regime at $L = 400$. We have not further verified whether a system of $L > 400$ has a regime of even stronger correlation, in which the localized damage mechanism occurs much earlier (see the dashed dotted line in Fig. 5.8).

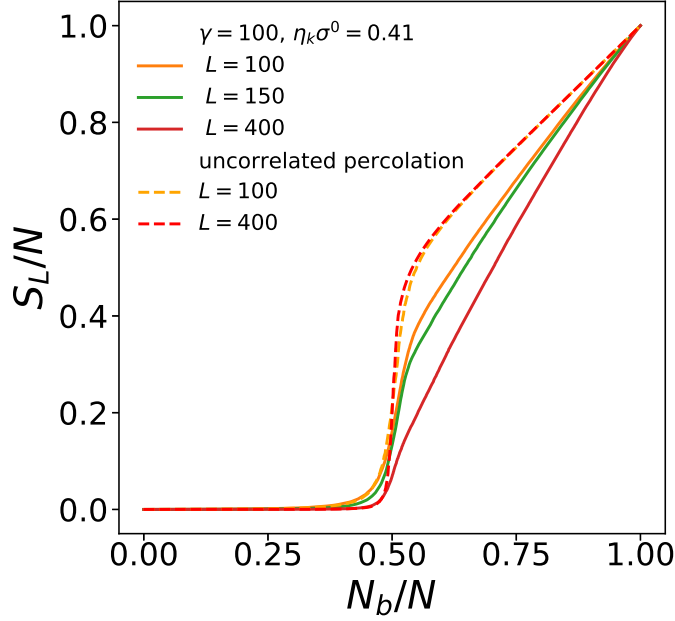


Figure 6.5: Largest crack growth S_L/N as a function of damage fraction N_b/N for $\eta_k\sigma_0 = 0.41$ and $\gamma = 100$ (solid lines) for several sizes L . S_L/N of the uncorrelated case (dashed lines) are presented as a comparison.

6.4 Variation of Percolation Thresholds

We have shown an unusual variation of the percolation threshold with the increase of the correlation strength at a fixed size of $L = 100$ in Section 5.3. We have learned that at $\xi \sim 0$, the average percolation threshold p_{av}^L exhibits a slight decay first. Upon the further increase of ξ , p_{av}^L increases subsequently. If approaching $\xi \sim 1$, p_{av}^L once again drops, even below p_c^{uncor} if the localized damage mechanism is strong enough. In this section, we attempt to exclude the possibility that the unusual behaviour of p_{av}^L is attributed to the size effects.

Fig. 6.6 (a) to (c) shows p_{av}^L as a function of γ for sizes $L = 100$ (blue) and $L = 250$ (orange) from low to high stresses. At low stress $\eta_k\sigma^0 = 0.51$, we observe that p_{av}^L in the case of $L = 250$ stabilizes for an even higher plateau value than that of $L = 100$. For a relatively high stress $\eta_k\sigma^0 = 1.0$, we note a sharp maximum at small γ for both sizes, but the lower plateau at high γ for $L = 250$ is even lower than that for $L = 100$. The higher the stress is, the lower the plateau value is. We observe plateau values lower than p_c^{uncor} for both sizes at $\eta_k\sigma^0 = 5.0$ as shown in Fig. 6.6 (c), and the maximum value for $L = 250$ is higher than that for $L = 100$.

Fig. 6.6 (d) shows p_{av}^L as a function of $\eta_k\sigma^0$ in the LLS scheme ($\gamma = 100$) for several sizes L . We observe that p_{av}^L reaches a maximum for all sizes and then rapidly drop with the increase of $\eta_k\sigma^0$. At high stress, $\eta_k\sigma^0 = 10.2$, p_{av}^L can reach a value less than p_c^{uncor} , because the system has a damage mechanism of correlated crack growth that occurs at an early

stage, prior to the merging stage. The larger L is, the higher and sharper the maximum is, and the lower p_{av}^L is for high stress.

To conclude, upon increasing ξ (the correlation strength) from 0 to 1, p_{av}^L undergoes a slight drop first, but grows and eventually drops again when the correlation is strong enough. This peculiar percolation behaviour of p_{av}^L is not caused by the finite-size effects.

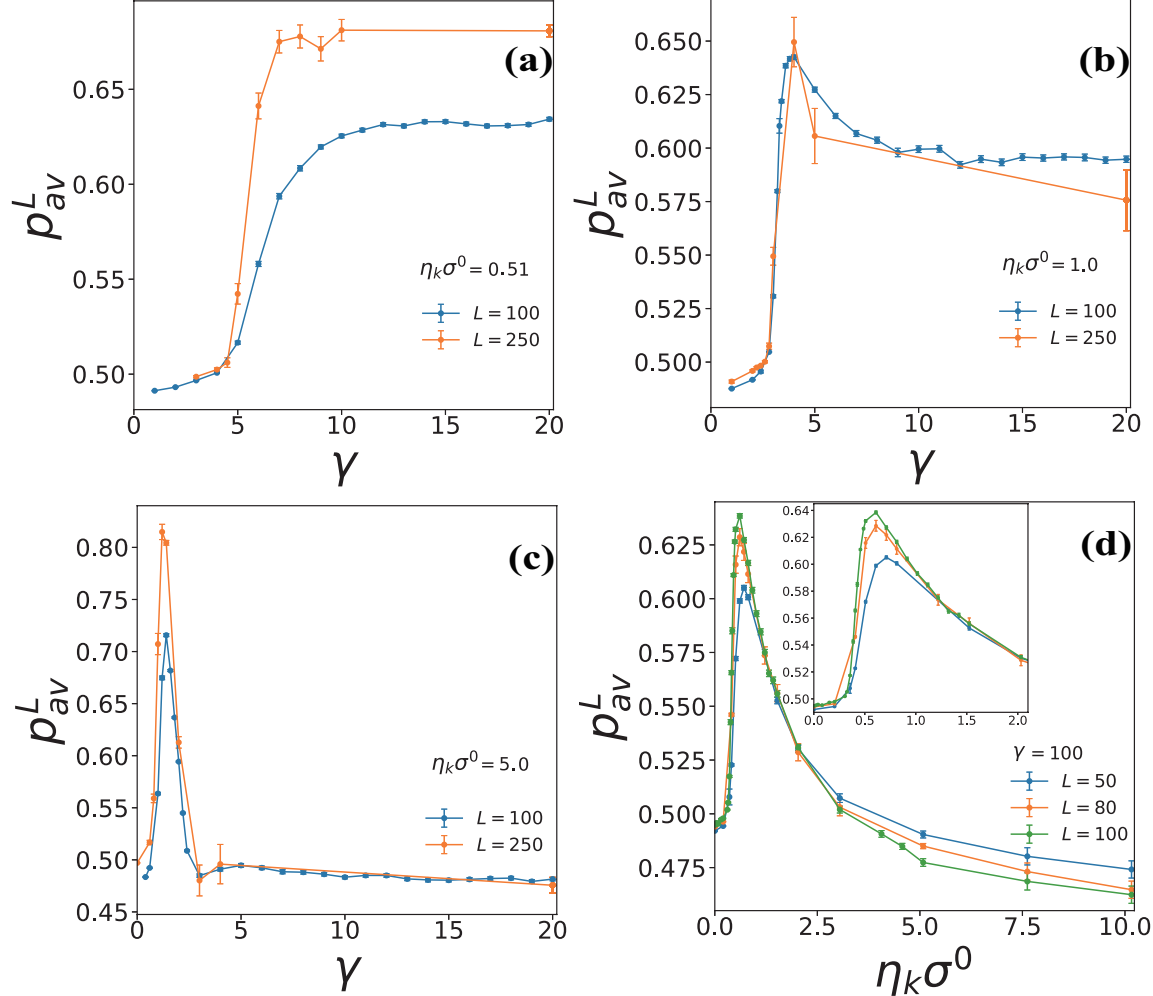


Figure 6.6: Plots of the average percolation thresholds p_{av}^L over γ for (a) $\eta_k \sigma^0 = 0.51$, (b) $\eta_k \sigma^0 = 1.0$ and (c) $\eta_k \sigma^0 = 5.0$, and p_{av}^L over $\eta_k \sigma^0$ for (d) $\gamma = 100$ for different L . Errors bars indicate standard deviations of the means of p_{av}^L .

6.5 Time-to-Fracture

In Section 5.5, we estimated the time-to-fracture, t_{PEM} , for square lattices of $L = 100$. However, the size L of a real polymer membrane network is estimated to have a scale of

$L = 10^2 - 10^3$, considering that the thickness of a film is about $10 - 150 \mu\text{m}$ [158] while the typical bundle length is about 40 nm [58, 128]. We now discuss size effects on t_{PEM} .

The middle rail of Fig. 6.7 shows t_{PEM} for systems of several sizes L in the random breakage regime, the localization regime and their crossover. The average percolation thresholds p_{av}^L are shown in the left rail of Fig. 6.7 to compare. The right rail of Fig. 6.7 shows t_{PEM} as a function of $1/L$ to get an estimate of t_{PEM} for $L \rightarrow \infty$. Time-to-fractures t_{PEM} of different fracture regimes exhibit distinctive dependence of L .

Fig. 6.7 (b) shows t_{PEM} for a system of uncorrelated percolation, as an extreme case of the random breakage regime, with $\eta_k \sigma^0 = 0.41$ and $\gamma = 0$. t_{PEM} remains almost the same within a variance of 2% and the slight change in t_{PEM} merely arises from the size effects of the uncorrelated percolation threshold p_c^{uncor} as illustrated in Fig. 6.7 (a). As $\lim_{L \rightarrow \infty} p_c^{\text{uncor}} = 0.5$ for a square lattice, we expect that t_{PEM} will eventually stabilize at around 0.388 for a large system as suggested in Fig. 6.7 (c).

In the crossover region with $\eta_k \sigma^0 = 0.41, \gamma = 100$ as seen in Fig. 6.7 (e), t_{PEM} reduces by 7% while L increases from 50 to 250. But p_{av}^L in Fig. 6.7 (d) exhibits a substantial increase with L , hence we realize that the decrease of t_{PEM} is not linked to the variation of p_{av}^L . We observe an even more pronounced drop of t_{PEM} for the regime of strong localized damage with $\eta_k \sigma^0 = 5.0, \gamma = 100$, in Fig. 6.7 (h) which corresponds to a change by 44 % as L increases from 50 to 250, but p_{av}^L reduces by only 3% (Fig. 6.7 (g)). Hence, we conclude that the stronger the correlation strength (or ξ) is, the more strongly the reduction of t_{PEM} varies with L . As indicated in Fig. 6.7 (i), $\alpha_k t_{\text{PEM}}$ converges to around 0.00006 when $L \rightarrow \infty$.

A Nafion membrane in a cell has a lifetime up to 20 000 hours [50] under ideal conditions at a temperature of 35 °C to 40 °C. As indicated by Table 5.1 (for $L = 100$), lifetime predictions of PEMs at a low stress are consistent with this value. But for a high stress regime, t_{PEM} reduces significantly (by 10 times) and reduce even further with larger lattice sizes L . However, we should note that t_{PEM} can be underestimated for high values of $\eta_k \sigma^0$ and γ , limited by the framework of our present model. The main impact factor is the assumption of stress conservation during stress redistribution.

6.6 Preliminary Studies

6.6.1 Fracture Regimes for Small σ^0 or γ

We have shown in Sections 6.4 and 6.5 that upon increasing L , the fracture regime exhibits a transition from the random breakage regime to the localization regime in the vicinity of the crossover region. We now explore the fracture regime of small $\eta_k \sigma^0$ or γ that is far away from the crossover region.

Fig. 6.8 shows the dynamic analysis of the largest crack growth S_L/N for $\eta_k \sigma^0 = 0.2$ and $\gamma = 100$ (solid lines) for several sizes L . The dynamics of S_L/N for systems of the uncorrelated case (dashed lines) are presented for comparison. As can be seen, S_L/N for the

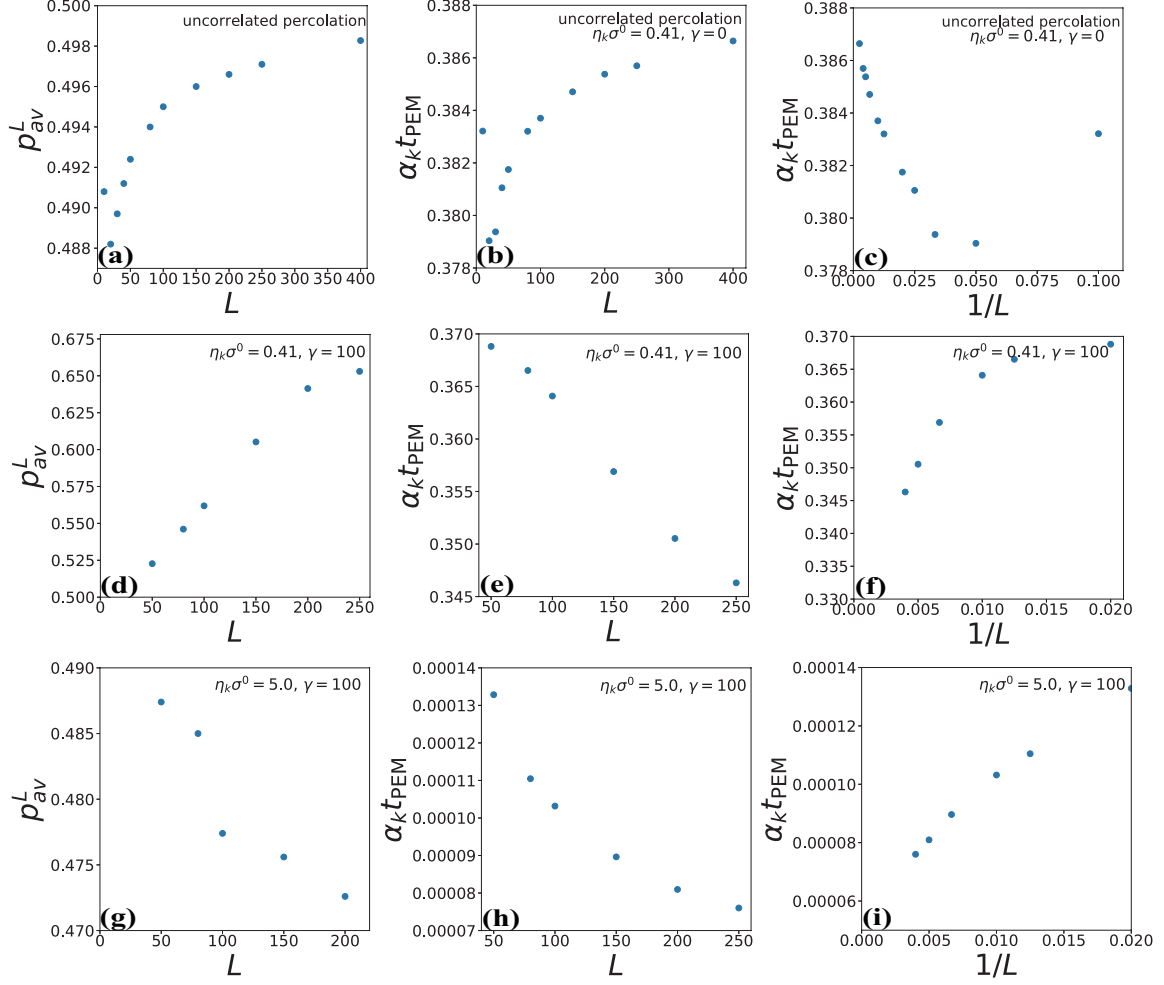


Figure 6.7: Time-to-fracture t_{PEM} (normalized to α_k) for (b) the uncorrelated system ($\eta_k \sigma^0 = 0.41$ and $\gamma = 0$), (e) the crossover region ($\eta_k \sigma^0 = 0.41$ and $\gamma = 100$), and (h) the localization regime ($\eta_k \sigma^0 = 5$ and $\gamma = 100$) as a function of L . Values of the corresponding average percolation threshold p_{av}^L are shown in (a), (d), and (g). t_{PEM} as a function of $1/L$ are shown in (c), (f), (i).

case $\eta_k\sigma^0 = 0.2$ and $\gamma = 100$, closely approaches the dynamic lines of the uncorrelated case of the same size L . Therefore, systems of sizes up to $L = 400$ remain in the random breakage regime and a crossover to the regime of localization is not found. A further verification of whether the damage regime approaches the localization regime when $L \rightarrow \infty$ for any finite $\eta_k\sigma^0$ and γ relies on a numerical exploration of lattices of much larger sizes.

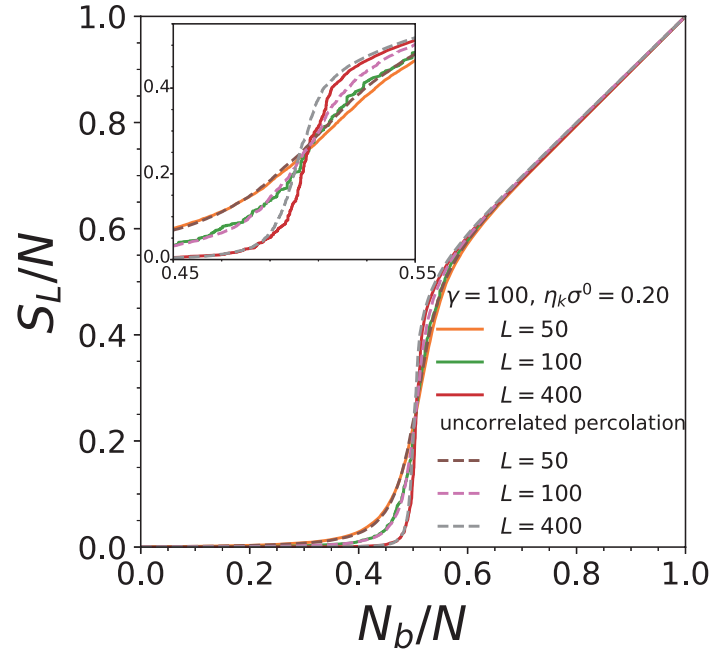


Figure 6.8: Largest crack growth S_L/N for $\eta_k\sigma^0 = 0.2$ and $\gamma = 100$ (solid lines) compared with the growth dynamics of uncorrelated percolation (dashed lines).

6.7 Summary

In this chapter, we focused on analyzing the competition between the two fracture regimes for different lattice sizes. We observed a transition from the random breakage regime to the localization regime in the vicinity of the crossover region of $\eta_k\sigma^0$ and γ upon increasing L . As for small values of $\eta_k\sigma^0$ and γ , the crossover to the localization regime is not yet observed owing to the limited lattice sizes.

We also analyzed the time-to-fractures of PEMs. It shows a rapid decrease of the lifetime in the regime of high stress for large sizes of lattices. A crucial assumption to be revisited in future work is the stress conservation considered in this model.

Chapter 7

Conclusions and Outlook

This chapter presents the main findings of the work in this thesis and potential extensions for further studies.

7.1 Conclusions

This thesis details how fracture dynamics on polymer electrolyte membranes (PEMs) are mapped onto a kinetic bond percolation model with a square lattice. This work provides both practical and physical insight into the fracture dynamics process. For practical purposes, we are motivated to predict the lifetime of polymer electrolyte membranes (PEMs). For a general view of statistical physics, we elaborate on understanding the fracture regimes in the disordered media in our current model framework.

Under the assumption of an exponential breakdown rule for bonds in the network and a power-law stress transfer rule ($\sigma_{\text{add}} \sim r^{-\gamma}$), the correlation between the breakage events is described by the physical quantities γ and σ^0 . The former factor controls the effective range of the stress transfer and the latter is the initial stress field magnitude, which is assumed to be uniformly applied to the system. By tuning the parameters γ and σ^0 , we have found a crossover between the two limits of fracture regimes: a percolation-type random breakage regime in the limit of weak correlation and a localization regime in the limit of strong correlation. The most important finding is probably the ability to describe the correlation strength or the degree of disorder of the system in terms of an order parameter ξ . We have explored lattices of both a fixed size and varying size L and the following main conclusions can be drawn.

The (frequency) distribution of percolation threshold shows two Gaussian-like peaks that exhibit a competing behaviour. In the two limiting fracture regimes, only one peak of the distribution (but with different widths) can be observed, while the distribution exhibits two Gaussian-like peaks in the crossover region. Hence, the order parameter ξ was introduced based on the area of the second peak to assess the crossover between the two fracture regimes. According to ξ , we generated the phase diagram of the two regimes and their

crossover in the plane spanned by σ^0 and γ based on ξ , at a fixed lattice size $L = 100$. For larger lattices, as indicated by the phase diagrams (via the cluster structures analysis), the crossover region has shifted towards smaller values of σ^0 and γ . In other words, the fracture regimes also compete for the increase of L in the vicinity of the crossover region. In this region, the localization regime is dominant for lattices of larger L .

Although the percolation thresholds may be intuitively expected to drop with the increase of the correlation strength, we observe this slight drop only when the correlation is very weak. Under stronger correlation, however, the percolation thresholds grow even higher than that of the uncorrelated case and eventually drop again when transiting to the localization regime. We confirmed that the peculiar percolation behaviour is not due to finite-size effects.

We analyzed the largest crack growth dynamics in the different regimes. Even though Refs. [159, 160] indicated that the percolating crack is formed or the final collapse of the system is caused by the coalescence of several cracks rather than the growth of a single one, this is not true in our model for strongly correlated damage regime, i.e., the localization. For a weakly correlated system, it is indeed that the parallel growth of microcracks and the merging of these cracks leads to the system's final failure. However, for a damage regime of localization, the growth of a single crack occurs very early on and that leads to the percolation of the system. The first time the stage of merging of cracks is skipped signals the onset of the localization regime.

The statistics of percolating cracks was used for a lifetime assessment of PEMs. The lifetime decreases exponentially with σ^0 . For larger initial stress σ^0 , the local load sharing (LLS) regime significantly reduces the lifetime of PEMs. As a function of γ , the PEM lifetime exhibits a transition from a higher plateau at $\gamma < 2$ to a lower plateau at $\gamma > 10$. Upon increasing L , the lifetime reduces, especially for strongly correlated systems.

We cannot conclude at this point that the above peculiar phenomena, i.e., the percolation behaviour, the damage growth regime, and the time-to-fractures of PEMs, have a more general meaning for statistical physics of fracture, or these behaviours are just limited to this present model. This model is within the same framework as the fiber bundle model (FBM), together with an assumption of an exponential breakage law of fractures. The most typical characteristic of the FBM is the assumption of stress conservation during the fracture process. This is clearly the cause of a counterintuitive observation of the rapid decrease of the time-to-fractures for large system sizes. Furthermore, Shekhawat *et al.* in Ref. [19] and Kim *et al.* in Ref. [157] have concluded that the random breakage regime is just a finite-size effect. This has been confirmed in the limited range of σ^0 and γ values in our work, in which lattice sizes are explored up to $L = 400$. For the whole range of σ^0 and γ , finite-size effects remain to be further investigated.

7.2 Outlook

This section discusses several possible extensions for further studies. To further understand finite-size effects, several explorations for larger lattices can be carried out within the current framework of the model. Further, this model should be modified to make more realistic predictions of the fracture dynamics in polymer electrolyte membrane networks. The outlook is detailed in the following paragraphs.

To explore whether the limit of $L \rightarrow \infty$ corresponds to a damage regime of localization, for a system of any finite values of σ^0 and γ , the numerical calculations need to be performed on lattices of particularly large sizes L . Approaching this limit, there comes to technical problems, viz., the considerable cost of computational time and RAM. In future studies, we can propose a modified algorithm that improves computational efficiency. A finite-size scaling analysis can then be studied given sufficient MC realizations over adequate parameter space σ^0 , γ and L . However, as indicated by Newman in Ref. [86], a system evaluated with an exponential breakdown rule (or the Gumbel strength distribution) is not expected to show any simple scaling, whereas a system evaluated with a power-law breakdown rule can [19]. (See discussions in Section 2.1.3.)

A major challenge of the modeling of the fracture dynamics on PEM networks is probably the introduction of a more realistic stress redistribution scheme during the fracture process. The stress field in a PEM is caused by an internal swelling pressure of water, but the current scalar stress field and the load transfer scheme of a power-law-type spatial decay is rather simple. The most nonphysical part is the assumption of stress (load) conservation; we expect a qualitatively different fracture propagation behaviour when a stress dissipation rule is introduced. Further, more theoretical or numerical explorations of stress field reconstructions of PEM supercells can be conducted to provide a more solid support in the future modeling of stochastic fracture processes.

Currently, to keep computational costs reasonable, the PEM network is mapped to two dimensional square lattices. Melchy and Eikerling in Ref. [58] has considered a more realistic three-dimensional cubic lattice, but at a quite small lattice size $L = 20$. Our preliminary simulations of cubic lattices suggest that the lifetime (of systems of the same number of bundles) will be reduced due to the lower percolation threshold of the cubic lattice. Furthermore, as the self-assembled network has a randomly disordered structure, a more ambitious goal is to study the fracture dynamics on a disordered structure. For examples of studies on disordered networks, the reader can refer to theoretical and experimental works by Reid *et al.* [161, 162]. Moreover, in the future, we can introduce nonuniformities in bundle sizes, stiffness, elastic modulus, and surface charge density in the polymer network.

Bibliography

- [1] L. Reti and E. M. Bührer. *The Unknown Leonardo*. Hutchinson London, 1974.
- [2] G. Galilei. *Discorsi e dimostrazioni matematiche intorno à due nuove scienze*. Leiden, 1638.
- [3] D. Gross. Some remarks on the history of fracture mechanics. In *The History of Theoretical, Material and Computational Mechanics*, page 195. Springer, 2014.
- [4] A. A. Griffith. The phenomena of rupture and flow in solids. *Phil. Trans. Roy. Soc. London*, A(221):163, 1920.
- [5] W. Weibull. A statistical theory of strength of materials. *Ing. Vet. Ak. Handl.*, 1939.
- [6] L. de Arcangelis, S. Redner, and H. Herrmann. A random fuse model for breaking processes. *Journal de Physique Lettres*, 46(13):585, 1985.
- [7] J. B. Rundle and W. Klein. Nonclassical Nucleation and Growth of Cohesive Tensile Cracks. *Phys. Rev. Lett.*, 63(2):171, 1989.
- [8] H. J. Herrmann and S. Roux. *Statistical models for the fracture of disordered media*. North-Holland, 1990.
- [9] R. L. Selinger, Z. G. Wang, W. M. Gelbart, and A. Ben-Shaul. Statistical-thermodynamic approach to fracture. *Phys. Rev. A*, 43(8):4396, 1991.
- [10] L. Mishnaevsky Jr. Methods of the theory of complex systems in modelling of fracture: A brief review. *Eng. Fract. Mech.*, 56(1):47, 1997.
- [11] S. N. Zhurkov and B. Narzullaev. Time dependence of the strength of solids. *Zh. Tekh. Fiz.*, 23(10):1677, 1953.
- [12] S. N. Zhurkov. Kinetic concept of the strength of solids. *Int. J. Fract. Mech.*, 1:311, 1965.
- [13] S. N. Zhurkov and V. E. Korsukov. Atomic mechanism of fracture of solid polymers. *J Polym Sci B Polym Phys*, 12(2):385, 1974.
- [14] S. N. Zhurkov and V. S. Kuksenko. The micromechanics of polymer fracture. *Int. J. Fract.*, 11(4):629, 1975.
- [15] F. W. Schwartz, L. Smith, and A. S. Crowe. A stochastic analysis of macroscopic dispersion in fractured media. *Water Resour. Res.*, 19(5):1253, 1983.

- [16] L. Smith and F. W. Schwartz. An analysis of the influence of fracture geometry on mass transport in fractured media. *Water Resour. Res.*, 20(9):1241, 1984.
- [17] Y. Bachmat and J. Bear. Macroscopic modelling of transport phenomena in porous media. 1: The continuum approach. *Transp. Porous Media*, 1(3):213, 1986.
- [18] S. Burylov and Y. L. Raikher. Macroscopic properties of ferronematics caused by orientational interactions on the particle surfaces. i. extended continuum model. *Mol. Cryst. Liq. Cryst.*, 258(1):107, 1995.
- [19] A. Shekhawat, S. Zapperi, and J. P. Sethna. From Damage Percolation to Crack Nucleation Through Finite Size Criticality. *Phys. Rev. Lett.*, 110(18):185505, 2013.
- [20] T. L. Chelidze. Percolation and fracture. *Phys. Earth Planet. Inter.*, 28(2):93, 1982.
- [21] M. Merzer and S. L. Klemperer. Modeling low-frequency magnetic-field precursors to the loma prieta earthquake with a precursory increase in fault-zone conductivity. *Pure Appl. Geophys.*, 150(2):217, 1997.
- [22] A. Hunt, R. Ewing, and B. Ghanbarian. *Percolation theory for flow in porous media*, volume 880. Springer, 2014.
- [23] D. J. Amit and D. J. Amit. *Modeling brain function: The world of attractor neural networks*. Cambridge University Press, 1992.
- [24] M. M. Lorist, E. Bezdan, M. ten Caat, M. M. Span, J. B. Roerdink, and N. M. Maurits. The influence of mental fatigue and motivation on neural network dynamics; an eeg coherence study. *Brain Res.*, 1270:95, 2009.
- [25] R. Albert and A.-L. Barabási. Statistical mechanics of complex networks. *Rev. Mod. Phys.*, 74(1):47, 2002.
- [26] P. Grassberger and Yi-Cheng Zhang. Self-organized formulation of standard percolation phenomena. *Physica A*, 224(1-2):169, 1996.
- [27] D. P. Kroese, T. Brereton, T. Taimre, and Z. Botev. Why the monte carlo method is so important today. *Wiley Interdiscip. Rev. Comput. Stat.*, 6:386, 2014.
- [28] M. M. Mench. *Fuel cell engines*. John Wiley & Sons, 2008.
- [29] A. Kraytsberg and Y. Ein-Eli. Review of advanced materials for proton exchange membrane fuel cells. *Energy Fuels*, 28(12):7303, 2014.
- [30] M. Derbeli, L. Sbita, M. Farhat, and O. Barambones. Pem fuel cell green energy generationsmc efficiency optimization. In *2017 International Conference on Green Energy Conversion Systems (GECS)*, page 1. IEEE, 2017.
- [31] R. M. Khorasany, A. Sadeghi Alavijeh, E. Kjeang, G. G. Wang, and R. K. Rajapakse. Mechanical degradation of fuel cell membranes under fatigue fracture tests. *J. Power Sources*, 274:1208, 2015.
- [32] X. Huang, R. Solasi, Y. Zou, M. Feshler, K. Reifsnider, D. Condit, S. Burlatsky, and T. Madden. Mechanical endurance of polymer electrolyte membrane and pem fuel cell durability. *J. Polym. Sci., Part B: Polym. Phys.*, 44(16):2346, 2006.

- [33] H. Wang, H. Li, and X.-Z. Yuan. *PEM Fuel Cell Failure Mode Analysis*, volume 1. CRC Press, Boca Raton, Florida, USA, 2011.
- [34] E. Kjeang, N. Djilali, and D. Sinton. Microfluidic fuel cells: A review. *J. Power Sources*, 186(2):353, 2009.
- [35] Y. Singh. *Characterization of Degradation, Fracture and Failure in Fuel Cell Membranes*. PhD thesis, Simon Fraser University, 2019.
- [36] T. Mima, T. Kinjo, S. Yamakawa, and R. Asahi. Study of the conformation of polyelectrolyte aggregates using coarse-grained molecular dynamics simulations. *Soft Matter*, 13(35):5991, 2017.
- [37] W. A. Curtin and H. Scher. Analytic model for scaling of breakdown. *Phys. Rev. Lett.*, 67(18):2457, 1991.
- [38] D. Y. Galperin and A. R. Khokhlov. Mesoscopic morphology of proton-conducting polyelectrolyte membranes of nafion® type: A self-consistent mean field simulation. *Macromol. Theory Simul.*, 15(2):137, 2006.
- [39] J. T. Wescott, Y. Qi, L. Subramanian, and T. Weston Capehart. Mesoscale simulation of morphology in hydrated perfluorosulfonic acid membranes. *J. Chem. Phys.*, 124(13):134702, 2006.
- [40] N. Grønbech-Jensen, R. J. Mashl, R. F. Bruinsma, and W. M. Gelbart. Counterion-induced attraction between rigid polyelectrolytes. *Phys. Rev. Lett.*, 78(12):2477, 1997.
- [41] J. Barrat and J. Joanny. Theory of polyelectrolyte solutions. *Adv. Chem. Phys.*, 94:1, 1996.
- [42] B.-Y. Ha and A. J. Liu. Counterion-mediated attraction between two like-charged rods. *Phys. Rev. Lett.*, 79(7):1289, 1997.
- [43] M. J. Stevens. Bundle binding in polyelectrolyte solutions. *Phys. Rev. Lett.*, 82(1):101, 1999.
- [44] L. Guldbrand, L. G. Nilsson, and L. Nordenskiöld. A monte carlo simulation study of electrostatic forces between hexagonally packed dna double helices. *J. Chem. Phys.*, 85(11):6686, 1986.
- [45] E. M. Schibli, A. G. Wright, S. Holdcroft, and B. J. Frisken. Morphology of anion-conducting ionenes investigated by x-ray scattering and simulation. *J. Phys. Chem. B*, 122(5):1730, 2018.
- [46] G. Gebel and O. Diat. Neutron and x-ray scattering: Suitable tools for studying ionomer membranes. *Fuel Cells*, 5(2):261, 2005.
- [47] A. S. Ioselevich, A. A. Kornyshev, and J. H. G. Steinke. Fine morphology of proton-conducting ionomers. *J. Phys. Chem. B*, 108(32):11953, 2004.
- [48] J. Wu, X. Z. Yuan, J. J. Martin, H. Wang, J. Zhang, J. Shen, S. Wu, and W. Merida. A review of pem fuel cell durability: Degradation mechanisms and mitigation strategies. *J. Power Sources*, 184(1):104, 2008.

- [49] S. F. Burlatsky, M. Gummalla, J. O'Neill, V. V. Atrazhev, A. N. Varyukhin, D. V. Dmitriev, and N. S. Erikhman. A mathematical model for predicting the life of polymer electrolyte fuel cell membranes subjected to hydration cycling. *J. Power Sources*, 215:135, 2012.
- [50] J. Yu, B. Yi, D. Xing, F. Liu, Z. Shao, Y. Fu, and H. Zhang. Degradation mechanism of polystyrene sulfonic acid membrane and application of its composite membranes in fuel cells. *Phys. Chem. Chem. Phys.*, 5(3):611, 2003.
- [51] S. Litster and G. McLean. PEM fuel cell electrodes. *J. Power Sources*, 130(1-2):61, 2004.
- [52] S. M. Haile. Fuel cell materials and components. *Acta Materialia*, 51(19):5981, 2003.
- [53] Y. Singh, R. T. White, M. Najm, T. Haddow, V. Pan, F. P. Orfino, M. Dutta, and E. Kjeang. Tracking the evolution of mechanical degradation in fuel cell membranes using 4D in situ visualization. *J. Power Sources*, 412:224, 2019.
- [54] N. S. Khattra, M. E. Hannach, K. H. Wong, M. Lauritzen, and E. Kjeang. Estimating the Durability of Polymer Electrolyte Fuel Cell Membranes Using a Fracture Percolation Model. *J. Electrochem. Soc*, 167(1):013528, 2020.
- [55] Y. Singh, F. P. Orfino, M. Dutta, and E. Kjeang. 3d visualization of membrane failures in fuel cells. *J. Power Sources*, 345:1, 2017.
- [56] Y. Singh, F. P. Orfino, M. Dutta, and E. Kjeang. 3d failure analysis of pure mechanical and pure chemical degradation in fuel cell membranes. *J. Electrochem. Soc.*, 164(13):F1331, 2017.
- [57] D. Ramani, Y. Singh, R. T. White, M. Wegener, F. P. Orfino, M. Dutta, and E. Kjeang. 4d in situ visualization of mechanical degradation evolution in reinforced fuel cell membranes. *Int. J. Hydrom. Energy*, 45(16):10089, 2020.
- [58] P.-É. A. Melchy and M. H. Eikerling. Theory of fracture formation in a heterogeneous fibrillar membrane. *J. Phys.: Condens. Matter*, 27(32):325103, 2015.
- [59] M. H. Eikerling and P. Berg. Poroelectroelastic theory of water sorption and swelling in polymer electrolyte membranes. *Soft Matter*, 7:5976, 2011.
- [60] P. Duxbury, P. Beale, and P. Leath. Size effects of electrical breakdown in quenched random media. *Phys. Rev. Lett.*, 57(8):1052, 1986.
- [61] L. de Arcangelis and H. Herrmann. Scaling and multiscaling laws in random fuse networks. *Phys. Rev. B*, 39(4):2678, 1989.
- [62] B. Kahng, G. Batrouni, S. Redner, L. de Arcangelis, and H. Herrmann. Electrical breakdown in a fuse network with random, continuously distributed breaking strengths. *Phys. Rev. B*, 37(13):7625, 1988.
- [63] F. Kun, S. Zapperi, and H. J. Herrmann. Damage in fiber bundle models. *Eur. Phys. J. B*, 17(2):269, 2000.

- [64] R. Hiesgen, E. Aleksandrova, G. Meichsner, I. Wehl, E. Roduner, and K. A. Friedrich. High-resolution imaging of ion conductivity of nafion® membranes with electrochemical atomic force microscopy. *Electrochim. Acta*, 55(2):423, 2009.
- [65] S. Zapperi, P. Ray, H. E. Stanley, and a. Vespignani. Avalanches in breakdown and fracture processes. *Phys. Rev. E.*, 59(5 Pt A):5049, 1999.
- [66] M. J. Alava, P. K. V. V. Nukala, and S. Zapperi. Statistical models of fracture. *Adv. Phys.*, 55(3-4):349, 2006.
- [67] D. W. Herrmann, W. Klein, and D. Stauffer. Spinodals in a long-range interaction system. *Phys. Rev. Lett.*, 49(17):1262, 1982.
- [68] S. Zapperi, P. K. V. V. Nukala, and S. Šimunović. Crack avalanches in the three-dimensional random fuse model. *Physica A*, 357(1):129, 2005.
- [69] S. Zapperi, P. Ray, H. E. Stanley, and A. Vespignani. First-Order Transition in the Breakdown of Disordered Media. *Phys. Rev. Lett.*, 78(8):1408, 1997.
- [70] R. C. Hidalgo, F. Kun, K. Kovács, and I. Pagonabarraga. Avalanche dynamics of fiber bundle models. *Phys. Rev. E*, 80(5):1, 2009.
- [71] S. Roux, A. Hansen, H. Herrmann, and E. Guyon. Rupture of heterogeneous media in the limit of infinite disorder. *J. Stat. Phys.*, 52(1-2):237, 1988.
- [72] A. Garcimartín, A. Guarino, L. Bellon, and S. Ciliberto. Statistical properties of fracture precursors. *Phys. Rev. Lett.*, 79(17):3202, 1997.
- [73] N. Yoshioka, F. Kun, and N. Ito. Kertész line of thermally activated breakdown phenomena. *Phys. Rev. E*, 82(5):2, 2010.
- [74] A. Stormo, K. S. Gjerden, and A. Hansen. Onset of localization in heterogeneous interfacial failure. *Phys. Rev. E*, 86(2):4, 2012.
- [75] M. Kloster, A. Hansen, and P. C. Hemmer. Burst avalanches in solvable models of fibrous materials. *Phys. Rev. E*, 56(3):2615, 1997.
- [76] D. Sornette. Mean-field solution of a block-spring model of earthquakes. *Journal de Physique I*, 2(11):2089, 1992.
- [77] P. C. Hemmer and A. Hansen. The distribution of simultaneous fiber failures in fiber bundles. *J. Appl. Mech.*, 59(4):909, 1992.
- [78] A. Hansen and P. C. Hemmer. Burst avalanches in bundles of fibers: Local versus global load-sharing. *Phys. Lett. A*, 184(6):394, 1994.
- [79] D. L. Turcotte. *Fractals and Chaos in Geology and Geophysics*. Cambridge University Press, 1997.
- [80] B. D. Coleman. Time dependence of mechanical breakdown in bundles of Fibers. V. Fibers of class A-2. *J. Appl. Phys.*, 30(5):720, 1957.
- [81] L. Moral, Y. Moreno, J. B. Gómez, and A. F. Pacheco. Time dependence of breakdown in a global fiber-bundle model with continuous damage. *Phys. Rev. E*, 63(6):2, 2001.

- [82] R. C. Hidalgo, Y. Moreno, F. Kun, and H. J. Herrmann. Fracture model with variable range of interaction. *Phys. Rev. E*, 65(4):046148, 2002.
- [83] L. Gansted, R. Brincker, and L. P. Hansen. Fracture mechanical Markov chain crack growth model. *Eng. Fract. Mech.*, 38(6):475, 1991.
- [84] M. Vázquez-Prada, J. Gómez, Y. Moreno, and A. Pacheco. Time to failure of hierarchical load-transfer models of fracture. *Phys. Rev. E*, 60(3):2581, 1999.
- [85] B. D. Coleman. Time dependence of mechanical breakdown phenomena. *J. Appl. Phys.*, 27(8):862, 1956.
- [86] W. I. Newman, A. M. Gabrielov, T. A. Durand, S. L. Phoenix, and D. L. Turcotte. An exact renormalization model for earthquakes and material failure statics and dynamics. *Physica D*, 77(1-3):200, 1994.
- [87] O. E. Yewande, Y. Moreno, F. Kun, R. C. Hidalgo, and H. J. Herrmann. Time evolution of damage under variable ranges of load transfer. *Phys. Rev. E*, 68(2):026116, 2003.
- [88] C. Manzato, A. Shekhawat, P. K. Nukala, M. J. Alava, J. P. Sethna, and S. Zapperi. Fracture strength of disordered media: Universality, interactions, and tail asymptotics. *Phys. Rev. Lett.*, 108(6):1, 2012.
- [89] A. Mattsson and T. Uesaka. Time-dependent statistical failure of fiber networks. *Phys. Rev. E*, 92(4):16, 2015.
- [90] P. M. Duxbury and P. L. Leath. Failure probability and average strength of disordered systems. *Phys. Rev. Lett.*, 72(17):2805, 1994.
- [91] M. Sahimi. Heterogeneous Media : From Long-Range Correlated Percolation To Fracture and Materials Breakdown. *Phys. Rep.*, 306:213, 1998.
- [92] I. C. Van Den Born, A. Santen, H. D. Hoekstra, and J. T. M. De Hosson. Mechanical strength of highly porous ceramics. *Phys. Rev. B*, 43(4):3794, 1991.
- [93] J. B. Gómez, Y. Moreno, and A. F. Pacheco. Probabilistic approach to time-dependent load-transfer models of fracture. *Phys. Rev. E*, 58(2):1528, 1998.
- [94] D. Stauffer. Scaling theory of percolation clusters. *Phys. Rep.*, 54(1):1, 1979.
- [95] E. V. Albano. Critical behaviour of a forest fire model with immune trees. *J. Phys. A*, 27(23):L881, 1994.
- [96] E. V. Albano. Spreading analysis and finite-size scaling study of the critical behavior of a forest fire model with immune trees. *Physica A*, 216(3):213, 1995.
- [97] A. A. Saberi and H. Dashti-Naserabadi. Three-dimensional Ising model, percolation theory and conformal invariance. *EPL*, 92(6):67005, 2011.
- [98] A. A. Saberi. Recent advances in percolation theory and its applications. *Phys. Rep.*, 578:1, 2015.

- [99] D. Stauffer. *Introduction to Percolation Theory*. Taylor & Francis, London, 1985.
- [100] C. R. Scullard. Exact site percolation thresholds using a site-to-bond transformation and the star-triangle transformation. *Phys. Rev. E*, 73(1):1, 2006.
- [101] H. Kesten. *Percolation theory for mathematicians*, volume 194. Springer, 1982.
- [102] M. E. J. Newman and R. M. Ziff. Efficient Monte Carlo algorithm and high-precision results for percolation. *Phys. Rev. Lett.*, 85(19):4104, 2000.
- [103] X. Feng, Y. Deng, and H. W. J. Blöte. Percolation transitions in two dimensions. *Phys. Rev. E*, 78(3):031136, 2008.
- [104] M. J. Lee. Pseudo-random-number generators and the square site percolation threshold. *Phys. Rev. E*, 78(3):031131, 2008.
- [105] P. N. Suding and R. M. Ziff. Site percolation thresholds for archimedean lattices. *Phys. Rev. E*, 60(1):275, 1999.
- [106] R. M. Ziff and H. Gu. Universal condition for critical percolation thresholds of kagomé-like lattices. *Phys. Rev. E*, 79(2):020102, 2009.
- [107] J. Škvor and I. Nezbeda. Percolation threshold parameters of fluids. *Phys. Rev. E*, 79(4):041141, 2009.
- [108] Z. Koza and J. Poła. From discrete to continuous percolation in dimensions 3 to 7. *J. Stat. Mech. Theory Exp.*, 2016(10):103206, 2016.
- [109] S. M. Dammer and H. Hinrichsen. Spreading with immunization in high dimensions. *J. Stat. Mech.: Theory Exp.*, 2004(07):P07011, 2004.
- [110] J. Wang, Z. Zhou, W. Zhang, T. M. Garoni, and Y. Deng. Bond and site percolation in three dimensions. *Phys. Rev. E*, 87(5):052107, 2013.
- [111] P. J. Flory. Molecular size distribution in three dimensional polymers. i. gelation1. *J. Am. Chem. Soc.*, 63(11):3083, 1941.
- [112] W. H. Stockmayer. Theory of molecular size distribution and gel formation in branched-chain polymers. *J. Chem. Phys.*, 11(2):45, 1943.
- [113] M. E. Fisher and J. W. Essam. Some cluster size and percolation problems. *J. Math. Phys.*, 2(4):609, 1961.
- [114] D. Stauffer. Gelation in concentrated critically branched polymer solutions. percolation scaling theory of intramolecular bond cycles. *J. Chem. Soc., Faraday Trans. 2*, 72:1354, 1976.
- [115] A. Coniglio, C. R. Nappi, F. Peruggi, and L. Russo. Percolation and phase transitions in the ising model. *Commun. Math. Phys.*, 51(3):315, 1976.
- [116] P. M. De Oliveira, R. A. Nóbrega, and D. Stauffer. Are the tails of percolation thresholds Gaussians? *J. Phys. A: Math. Gen.*, 37(12):3743, 2004.

- [117] T. Harter. Finite-size scaling analysis of percolation in three-dimensional correlated binary Markov chain random fields. *Phys. Rev. E*, 72(2):026120, 2005.
- [118] A. Weinrib. Long-range correlated percolation. *Phys. Rev. B*, 29(1):387, 1984.
- [119] M. B. I. Isichenko. Percolation, statistical topography, and transport in random media. *Rev. Mod. Phys.*, 64(4):961, 1992.
- [120] M. Sahimi. Flow phenomena in rocks: From continuum models to fractals, percolation, cellular automata, and simulated annealing. *Rev. Mod. Phys.*, 65(4):1393, 1993.
- [121] N. Araújo, P. Grassberger, B. Kahng, K. J. Schrenk, and R. M. Ziff. Recent advances and open challenges in percolation. *Eur. Phys. J. Spec. Top.*, 223(11):2307, 2014.
- [122] S. F. Carle and G. E. Fogg. Transition probability-based indicator geostatistics. *Math. Geol.*, 28(4):453, 1996.
- [123] P. Renault. The effect of spatially correlated blocking-up of some bonds or nodes of a network on the percolation threshold. *Transp. Porous Media*, 6(4):451, 1991.
- [124] K. J. Schrenk, N. Posé, J. J. Kranz, L. V. M. Van Kessenich, N. A. M. Araújo, and H. J. Herrmann. Percolation with long-range correlated disorder. *Phys. Rev. E*, 88(5):1, 2013.
- [125] A. Weinrib. Percolation threshold of a two-dimensional continuum system. *Phys. Rev. B*, 26(3):1352, 1982.
- [126] K. Mendelson. Percolation threshold of a class of correlated lattices. *Phys. Rev. E*, 56(6):6586, 1997.
- [127] J.-P. Eckmann, O. Feinerman, L. Gruendlinger, E. Moses, J. Soriano, and T. Tlusty. The physics of living neural networks. *Phys. Rep.*, 449(1-3):54, 2007.
- [128] G. Gebel. Structural evolution of water swollen perfluorosulfonated ionomers from dry membrane to solution. *Polymer*, 41(15):5829, 2000.
- [129] A. S. Ioselevich and A. A. Kornyshev. Approximate symmetry laws for percolation in complex systems: Percolation in polydisperse composites. *Phys. Rev. E*, 65(2):1, 2002.
- [130] L. Rubatat, A. L. Rollet, G. Gebel, and O. Diat. Evidence of elongated polymeric aggregates in Nafion. *Macromolecules*, 35(10):4050, 2002.
- [131] A. L. Rollet, O. Diat, and G. Gebel. A new insight into nation structure. *J. Phys. Chem. B*, 106(12):3033, 2002.
- [132] T. D. Gierke and W. Y. Hsu. *The ClusterNetwork Model of Ion Clustering in Perfluorosulfonated Membranes*, chapter 13, page 283. 1982.
- [133] P.-É. A. Melchy and M. H. Eikerling. Physical theory of ionomer aggregation in water. *Phys. Rev. E*, 89(3):34, 2014.

- [134] R. V. Mises. Mechanik der festen Körper im plastisch-deformablen Zustand. *Nachrichten von der Gesellschaft der Wissenschaften zu Göttingen, Abh. Math.-Phys. Kl.*, 1913:582, 1913.
- [135] F. Irgens. *Continuum mechanics*. Springer Science & Business Media, 2008.
- [136] Y. Moreno, J. Gomez, and A. Pacheco. Fracture and second-order phase transitions. *Phys. Rev. Lett.*, 85(14):2865, 2000.
- [137] S. Pradhan, A. Hansen, and B. K. Chakrabarti. Failure processes in elastic fiber bundles. *Rev. Mod. Phys.*, 82(1):499, 2010.
- [138] M. Ghelichi, K. Malek, and M. H. Eikerling. Ionomer self-assembly in dilute solution studied by coarse-grained molecular dynamics. *Macromolecules*, 49(4):1479, 2016.
- [139] L. Golubović and S. Feng. Rate of microcrack nucleation. *Phys. Rev. A*, 43(10):5223, 1991.
- [140] L. Golubovic and A. Peredera. Mechanism of time-delayed fractures. *Phys. Rev. E*, 51(4):2799, 1995.
- [141] K. Binder. Applications of Monte Carlo methods to statistical physics. *Reports Prog. Phys.*, 60(5):487, 1997.
- [142] M. J. Hoffmann, S. Matera, and K. Reuter. Kmox: A lattice kinetic Monte Carlo framework. *Comput. Phys. Commun.*, 185(7):2138, 2014.
- [143] L. Blum, M. Blum, and M. Shub. A simple unpredictable pseudo-random number generator. *SIAM J. Comput.*, 15(2):364, 1986.
- [144] A. A. Markov. Extension of the limit theorems of probability theory to a sum of variables connected in a chain. *Dynamic probabilistic systems*, 1:552, 1971.
- [145] J. G. Kemeny and J. L. Snell. *Markov chains*. Springer-Verlag, New York, 1976.
- [146] N. Metropolis, A. W. Rosenbluth, M. N. Rosenbluth, A. H. Teller, and E. Teller. Equation of state calculations by fast computing machines. *J. Chem. Phys.*, 21(6):1087, 1953.
- [147] W. K. Hastings. Monte Carlo sampling methods using Markov chains and their applications. *Biometrika*, 57(1):97, 1970.
- [148] S. A. Serebrinsky. Physical time scale in kinetic Monte Carlo simulations of continuous-time Markov chains. *Phys. Rev. E*, 83(3):2010, 2011.
- [149] T. H. Cormen, C. E. Leiserson, R. L. Rivest, and C. Stein. *Introduction to algorithms*. MIT Press, 2009.
- [150] J. Hoshen and R. Kopelman. Percolation and cluster distribution. I. Cluster multiple labeling technique and critical concentration algorithm. *Phys. Rev. B*, 14(8):3438, 1976.
- [151] M. E. J. Newman and R. M. Ziff. Fast Monte Carlo algorithm for site or bond percolation. *Phys. Rev. E*, 64(1):1, 2001.

- [152] Y. Wang and M. Eikerling. Fracture dynamics of correlated percolation on ionomer networks. *Phys. Rev. E*, 101(4):1, 2020.
- [153] S. Prakash, S. Havlin, M. Schwartz, and H. E. Stanley. Structural and dynamical properties of long-range correlated percolation. *Phys. Rev. A*, 46(4):R1724, 1992.
- [154] M. R. Riedel and S.-i. Karato. Microstructural development during nucleation and growth. *Geophys. J. Int.*, 125(2):397, 1996.
- [155] Z. Danku and F. Kun. Fracture process of a fiber bundle with strong disorder. *J. Stat. Mech.: Theory Exp.*, 2016(7):73211, 2016.
- [156] J. Zierenberg, N. Fricke, M. Marenz, F. Spitzner, V. Blavatska, and W. Janke. Percolation thresholds and fractal dimensions for square and cubic lattices with long-range correlated defects. *Phys. Rev. E*, 96(6):062125, 2017.
- [157] D.-H. H. Kim, B. J. Kim, and H. Jeong. Universality Class of the Fiber Bundle Model on Complex Networks. *Phys. Rev. Lett.*, 94(2):25501, 2005.
- [158] T. Muzaffar. *Physical modeling of local reaction conditions inside of cathode catalyst layer of polymer electrolyte fuel cells*. PhD thesis, Simon Fraser University, 2018.
- [159] L. Monette and W. Klein. Physical Modeling of Local Reaction Conditions Inside of Cathode Catalyst Layer of Polymer Electrolyte Fuel Cells. *Phys. Rev. Lett.*, 68(15):2336, 1992.
- [160] S. Nukala, P. K. V. V. Nukala, S. Šimunović, and F. Guess. Crack-cluster distributions in the random fuse model. *Phys. Rev. E*, 73(3):1, 2006.
- [161] D. R. Reid, N. Pashine, J. M. Wozniak, H. M. Jaeger, A. J. Liu, S. R. Nagel, and J. J. De Pablo. Auxetic metamaterials from disordered networks. *Proc. Natl. Acad. Sci. U. S. A.*, 115(7):E1384, 2018.
- [162] D. R. Reid, N. Pashine, A. S. Bowen, S. R. Nagel, and J. J. de Pablo. Ideal isotropic auxetic networks from random networks. *Soft Matter*, 15(40):8084, 2019.